

THESIS FOR THE DEGREE OF LICENTIATE OF ENGINEERING

**Improvement of the nuclear safety
code CATHARE based on
thermal-hydraulic experiments for
the Jules Horowitz Reactor**

ALBERTO GHIONE

Department of Applied Physics, Division of Nuclear Engineering
Chalmers University of Technology
Göteborg, Sweden, 2015

Improvement of the nuclear safety code CATHARE based on thermal-hydraulic experiments for the Jules Horowitz Reactor
Alberto Ghione

©Alberto Ghione, 2015

Licentiate thesis at Chalmers University of Technology
Technical report CTH-NT-306
ISSN 1653-4662

Department of Applied Physics
Division of Nuclear Engineering
Chalmers University of Technology
SE-412 96 Göteborg
Sweden

Improvement of the nuclear safety code CATHARE based on thermal-hydraulic experiments for the Jules Horowitz Reactor
Alberto Ghione
Department of Applied Physics, Division of Nuclear Engineering
Chalmers University of Technology

ABSTRACT

The Jules Horowitz Reactor (JHR) is a material testing research reactor under construction at CEA-Cadarache (France). One of the computer codes employed in the safety analysis of this reactor is the thermal-hydraulic system code CATHARE. The physical models implemented in CATHARE have been developed and optimized for commercial Light Water Reactors which significantly differ from JHR in terms of both core geometry and operational conditions. In view of this, it is crucial to carefully assess the capabilities of CATHARE with respect to the JHR characteristics.

The current thesis aims at improving the physical correlations used in CATHARE for JHR modeling. The work is based on the SULTAN-JHR experiments in narrow rectangular channels, that were carried out at CEA-Grenoble in order to investigate the thermal-hydraulics of the JHR core channels.

The first part of the study is related to the assessment of the correlations for single-phase friction coefficients and for single-phase forced convection heat transfer. A more comprehensive modeling of single-phase flow in CATHARE is proposed by including a laminar-turbulent transition region. In addition, it is found that the turbulent heat transfer coefficient may be significantly under-estimated by standard correlations (e.g. Dittus-Boelter correlation) at high Reynolds numbers. Thus, new ad-hoc correlations were developed from the SULTAN-JHR data by making use of a best-fitting procedure.

In the second part, the CATHARE two-phase heat transfer modeling is revised. Several correlations have been tested against the SULTAN-JHR experiments. The results show that the simplified Forster-Greif correlation may accurately predict the heat transfer in JHR-type channels under fully developed boiling conditions. Such a relationship is then added in CATHARE.

Keywords: JHR, nuclear research reactor, CATHARE, SULTAN-JHR, narrow rectangular channels, single-phase friction, laminar-turbulent transition, single-phase heat transfer, fully developed boiling

Appended papers

The following papers are included in this licentiate thesis:

PAPER I

A. Ghione, B. Noel, P. Vinai, C. Demazière, *On the prediction of single-phase forced convection heat transfer in narrow rectangular channels*, NUTHOS10-1116, The 10th International Topical Meeting on Nuclear Thermal Hydraulics, Operation and Safety (NUTHOS-10), Okinawa (Japan), Dec. 14-18 2014.

PAPER II

A. Ghione, B. Noel, P. Vinai, C. Demazière, *Wall superheat prediction in narrow rectangular channels under Fully Developed Boiling of water at low pressures*, Manuscript to be submitted to the 16th International Topical Meeting on Nuclear Reactor Thermal Hydraulics (NURETH-16), Chicago (USA), Aug. 30 - Sep. 4 2015.

Contents

Nomenclature	ix
1 Introduction	1
1.1 Jules Horowitz Reactor	1
1.2 Scope of the thesis and structure	3
2 The system code CATHARE	5
2.1 Conservation equations	6
2.1.1 Mass conservation equations	7
2.1.2 Momentum conservation equations	8
2.1.3 Energy conservation equations	9
2.1.4 Non-condensable gas balance equations	9
2.2 Closure laws	9
2.2.1 Flow pattern transition	10
2.2.2 Momentum transfer: Interfacial friction	11
2.2.3 Momentum transfer: Wall friction	12
2.2.4 Interfacial heat transfer	13
2.2.5 Wall Heat transfer	15
3 The SULTAN-JHR experiments	25
3.1 Experimental set-up	25
3.1.1 Experimental loop	25
3.1.2 Test section	27
3.1.3 Instrumentation	33
3.2 Description of the test procedure	39
3.2.1 Isothermal tests	40
3.2.2 Flow Redistribution tests	41
3.2.3 Critical Heat Flux tests	41
3.2.4 Dissolved gas tests	41
3.3 Experimental data reduction	42
3.3.1 Calculation of the wet wall temperature	42
3.3.2 Inconel conductivity	44
3.3.3 Heat losses	46
3.3.4 Analysis of the test stability	47
3.4 CATHARE model of the test section	48
3.5 Simplified model for single-phase flow	50

4	Single-phase modeling	53
4.1	Improvement of CATHARE code structure	53
4.2	Friction and laminar-turbulent transition modeling	55
4.2.1	The friction factor in laminar flow	55
4.2.2	The laminar-turbulent transition	58
4.2.3	The friction factor in transition flow	59
4.2.4	The friction factor in turbulent flow	60
4.3	Laminar and transition heat transfer modeling	61
4.3.1	Laminar heat transfer coefficient	62
4.3.2	Transition heat transfer coefficient	62
4.3.3	Entrance effects	63
4.3.4	Comparison with SULTAN-JHR data	64
4.4	Turbulent heat transfer modeling	67
4.4.1	Selected correlations from the literature	68
4.4.2	Development of a correlation based on the SULTAN-JHR data	74
4.4.3	Influence of the channel geometry	83
4.5	Summary and suggested correlations	84
5	Two-phase heat transfer modeling	87
5.1	Physics of flow boiling and modeling	87
5.1.1	Modeling of two-phase heat transfer	89
5.1.2	Modeling approach in CATHARE	91
5.2	Correlations for fully developed boiling heat transfer	93
5.2.1	Jens-Lottes and Thom correlations	94
5.2.2	Qiu correlation	95
5.2.3	Belhadj correlation	96
5.2.4	Gorenflo correlation	98
5.2.5	Forster-Greif correlation	100
5.3	Summary and suggested modifications	104
6	Conclusions and future work	107
6.1	Summary of the main results	107
6.2	Future work	108
	Acknowledgments	109
	Bibliography	110
	Appended papers	117

Nomenclature

Acronym	Description
<i>AECL – UO</i>	Atomic Energy of Canada Ltd. - University of Ottawa
<i>BE</i>	Best-Estimate
<i>BWR</i>	Boiling Water Reactor
<i>CATHARE</i>	Code for Analysis of THERmalhydraulics during an Accident of Re-actor and safety Evaluation
<i>CEA</i>	Commissariat à l'Énergie Atomique et aux énergies alternatives (France)
<i>CFL</i>	Courant-Friedrichs-Lewy condition
<i>CHF</i>	Critical Heat Flux
<i>DBA</i>	Design Basis Accident
<i>DNB</i>	Departure from Nucleate Boiling
<i>EdF</i>	Électricité de France
<i>FDB</i>	Fully Developed Boiling
<i>IRSN</i>	Institut de Radioprotection et de Sûreté Nucléaire (France)
<i>ITF</i>	Integral Test Facility
<i>JHR</i>	Jules Horowitz Reactor
<i>LNE</i>	Laboratoire National d'Essais (France)
<i>LOCA</i>	Loss Of Coolant Accident
<i>MTR</i>	Material Testing Reactor
<i>NPL</i>	National Physical Laboratory (UK)
<i>NPP</i>	Nuclear Power Plant
<i>NRC</i>	Nuclear Regulatory Commission (USA)
<i>NVG</i>	Net Vapor Generation
<i>ONB</i>	Onset of Nucleate Boiling
<i>PWR</i>	Pressurized Water Reactor
<i>SETF</i>	Separate Effect Test Facility

Symbol	Dimensions	Description
General Symbols		
<i>A</i>	m^2	Duct cross section (or flow) area
a_i	m^{-1}	Volumetric inter-facial area
C_D	-	Drag coefficient
c_p	$J/kg/K$	Specific heat capacity
D_h	m	Hydraulic diameter $D_h = \frac{4A}{P_w}$

Continued on next page

Continued from previous page		
Symbol	Dimensions	Description
E	-	Entrainment rate
f	-	Friction factor
g	m/s^2	Acceleration of gravity $g = 9.8066$
G	kg/m^2s	Mass flux $G = \dot{m}/A = \rho v$
h	$W/m^2/K$	Heat transfer coefficient
i	J/kg	Specific enthalpy
i_{lg}	$J/kg = m^2/s^2$	Latent heat
k	$W/m/K$	Thermal conductivity
L/D	-	Length to pipe diameter ratio
\dot{m}	kg/s	Mass flow-rate
Nu	-	Nusselt number $Nu = \frac{hD_h}{k}$
p	Pa	Pressure
Pe	-	Peclet number $Pe = RePr$
Pr	-	Prandtl number $Pr = \frac{c_p \mu}{k}$
P_f	m	Friction perimeter
P_h	m	Heating perimeter
P_w	m	Wet perimeter
q	W/m^2	Heat flux in CATHARE
q'''	W/m^3	Volumetric heat transfer rate in CATHARE
R	-	Stratification rate
Re	-	Reynolds number $Re = \frac{GD_h}{\mu}$
t	s	Time
T	K or $^{\circ}C$	Temperature
v	m/s	Velocity
W	W	Supplied electrical power
x	-	Steam quality
z	m	Axial distance

Symbol	Dimensions	Description
Greek Symbols		
α	-	Void fraction
Γ	$kg/m^3/s$	Inter-facial mass transfer per unit volume
μ	$Pa \cdot s = kg/m/s$	Dynamic viscosity
ν	m^2/s	Kinematic viscosity
ρ	kg/m^3	Density
σ	kg/s^2	Surface tension
τ	$N/m^2 = kg/m/s^2$	Shear stress
ϕ	W/m^2	Heat flux

Subscripts	
ch	associated to the channel
cor	associated to the corners
g	Gas (or vapor) phase
l	Liquid phase

<i>m</i>	Mixture
<i>max</i>	Maximum
<i>nb</i>	Nucleate Boiling
<i>pl</i>	associated to the plate
<i>sat</i>	Saturation
<i>w</i>	Wall

Chapter 1

Introduction

1.1 Jules Horowitz Reactor

The current European fleet of Material Testing Reactors (MTRs) has greatly contributed to the development and support of the nuclear power programs. The MTRs are needed for the qualification and optimization of the materials and the nuclear fuels to be used in commercial Nuclear Power Plants (NPPs), and also for the design and development of future reactors (e.g. GenIV reactors). The majority of these reactors started their operation more than 50 years ago, as shown in Table 1.1. Thus, they are close to the end of their lifetime (e.g. the French Osiris is planned to be shut down at the end of 2015).

Table 1.1: List of the main MTRs in Europe [1].

Country	Reactor name	First criticality	Power [MWth]
Czech Rep.	LVR15	1957	10
Norway	Halden	1960	19
Netherlands	HFR	1961	45
Belgium	BR2	1963	60
France	Osiris	1966	70

In this context, there is a strategic need for the construction of new MTRs in Europe. The Jules Horowitz Reactor (JHR) [1] is therefore under construction in France, at CEA-Cadarache. The JHR program is the result of a cooperation between several international industrial and institutional partners, which will benefit of the experimental capabilities of the facility. The first criticality is provisionally planned for the year 2020.

The main objectives of this reactor are:

- Study of the materials and fuel behavior under irradiation for addressing ageing issues in current Light Water Reactors (LWRs).
- Development and optimization of materials and fuels for near- and long-term future reactors, namely GenIII and GenIV reactors.
- Production of radioisotopes for medical use. For example, the reactor is planned to satisfy 50% of the European demand of Tc^{99} .

JHR is a 100 MWth pool-type reactor, which uses light water both for cooling and neutron moderation. It has been designed to provide high neutron fluxes, both thermal (up to $6 \cdot 10^{14} \frac{\text{neutrons}}{\text{cm}^2 \cdot \text{s}}$ in the reflector) and fast (up to $5 \cdot 10^{14} \frac{\text{neutrons}}{\text{cm}^2 \cdot \text{s}}$ with neutron energy above 1 MeV in the core) [2]. The achievable radiation damage for in-core experiments is approximately equal to 16 dpa/y, while the linear power in the reflector may reach 850 W/cm for the qualification of nuclear fuels [1].

The core is placed in a pressurized tank at the bottom of the reactor pool (approximately 9 m below the water level [3]) and it is cooled by forced convection of water at low pressure. It has a diameter of 710 mm and an active fuel height equal to 600 mm. It is surrounded by a beryllium reflector where it is possible to introduce experimental devices. The small volume of the core implies an high power density of 460 kW/l, which is around 10 times the energy density of a BWR.

Up to 37 cylindrical fuel elements of external diameter equal to 98.6 mm are placed in the core. These fuel elements consist of a set of curved plates that are assembled in eight concentric rings fixed with stiffeners, as shown in Figure 1.1.

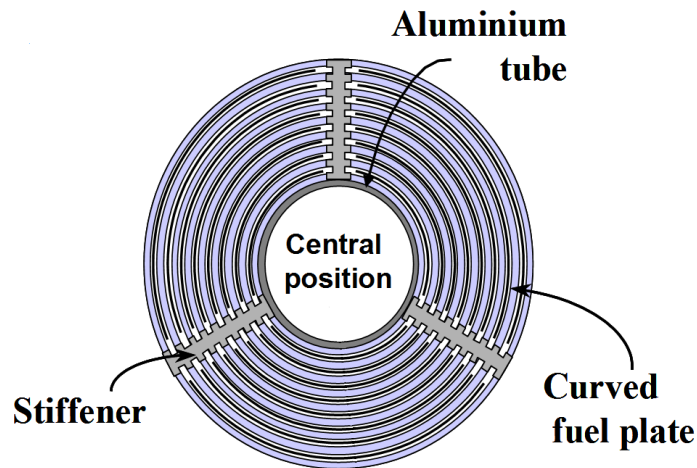


Figure 1.1: Schematic representation of the JHR fuel element. Courtesy by CEA.

In the central position of the fuel element, it is possible to insert either control rods or experimental devices. The coolant flows upward between the parallel fuel plates in narrow channels of average gap size equal to 1.95 mm. High velocities of the coolant (up to 15 m/s) are required since the high power density leads to high heat fluxes in the fuel plates (up to 5.5 MW/m^2).

A summary of the JHR nominal operating conditions is reported in Table 1.2.

Table 1.2: JHR nominal operating conditions [4]

Thermal power [MWth]	100	Power density [kW/l]	460
Core outlet pressure [MPa]	0.8	Core pressure drop [MPa]	0.7
Core mass flow rate [m³/h]	8500	Coolant velocity [m/s]	15
Coolant temperature [°C]	30 – 50	Maximum heat flux [MW/m²]	5.5

1.2 Scope of the thesis and structure

The thermal-hydraulic system code CATHARE is used for the safety analysis of JHR. The code is based on a transient 2-fluid 6-equation model, complemented with proper closure laws for single-phase and two-phase flow. These closure laws has been extensively validated for the modeling of conventional LWRs [5]. However, further work is required to assess the modeling capabilities of CATHARE in respect of JHR because, as described in the previous section, the core design and the operational conditions significantly differ from the case of commercial reactors.

The current work aims at evaluating the physical models implemented in CATHARE against the SULTAN-JHR experiments in narrow rectangular channels, that were carried out at CEA-Grenoble and that are representative of the thermal-hydraulics of the JHR core channels. In particular, this study focuses on correlations of single-phase friction and wall heat transfer both in single and two-phase flow.

The thesis is organized as follows. In Chapter 2, the system code CATHARE is presented in terms of its conservation equations and main closure laws. In Chapter 3, the SULTAN-JHR experiments are described. In Chapter 4, an analysis of the modeling capabilities of CATHARE for single-phase flow and related improvements are reported. In Chapter 5, correlations for two-phase heat transfer in fully developed boiling are assessed. In Chapter 6, conclusions and future work are summarized.

Chapter 2

The system code CATHARE

In this chapter, the set of conservation equations and the closure laws in the CATHARE system code are presented.

A system code has the capability of predicting the thermal-hydraulic behavior of a nuclear reactor in operational and accidental conditions. Different system codes are available, such as the US-NRC codes TRACE [6] and the French code CATHARE.

CATHARE has been developed since 1979 by the French Atomic Energy Commission CEA, the French utility EdF, the reactor vendor AREVA-NP and the French Nuclear Safety Institute IRSN. The name CATHARE is an acronym derived from: Code for Analysis of THERmal-HYdraulicS during an Accident of Reactor and safety Evaluation. The main focus of CATHARE was originally the simulation of safety-related transients in Light Water Reactors. In particular, it has been extensively applied to simulate Design Basis Accidents (DBAs) in PWR, like loss of coolant accidents (LOCAs) due to both large and small breaks. Recently, new modules for the treatment of other reactor types have been introduced [7]. Modules for the Gas-Cooled Reactor (GCR), the Sodium-cooled Fast-breeder Reactor (SFR) and the Supercritical Light Water-Cooled Reactor (SLWCR) were added, as well as modules for non-nuclear applications (e.g. cryogenic rocket engines).

CATHARE is based on a two-fluid model [8] where six conservation equations (3 for the liquid phase and 3 for the gas phase) together with proper closure laws (also called physical models or correlations) are solved. In addition, equations for non-condensable gases and the transport of radio-chemical components are also included. Therefore, the code is able to capture different two-phase flow and heat transfer regimes, mechanical non-equilibrium phenomena (e.g. phase separation as: stratification, annular flows and the Counter-Current Flow Limitation (CCFL)) and thermal non-equilibrium phenomena (e.g. metastable superheated water during flashing, superheated steam with saturated water during re-flooding and sub-cooled water with saturated steam during safety injections). A large variety of experimental data from Separate Effect Test Facilities (SETFs) have been employed to validate the physical models and the code has also been extensively assessed against Integral Test Facilities (ITFs) [5].

The conservation equations for mass, momentum and energy are spatially discretized using a first order upwind scheme. A *staggered mesh* nodalization is used, so that the numerical difficulties due to the pressure-velocity coupling (e.g. checkerboard instabilities) can be overcome [9]. Therefore the scalar quantities (e.g. pressure,

enthalpy, etc...) are stored at the cell centers (+), while the vector quantities (e.g. gas and liquid velocities) at the cell faces (●), as shown in Figure 2.1. The first order upwind scheme based on the donor cell principle is employed for convective terms.

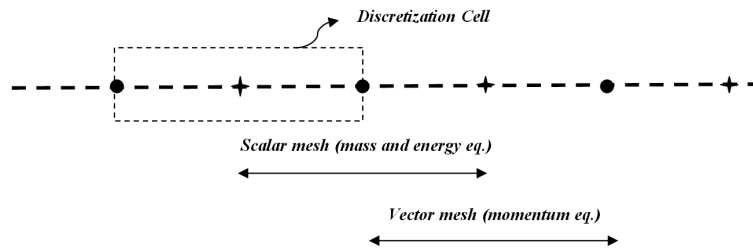


Figure 2.1: The staggered mesh approach in CATHARE [10].

The time discretization scheme is *fully implicit* when 1D and 0D modules are considered and *semi-implicit* with 3D modules. When the implicit scheme is used, no stability condition is required for the time-step, which is adjusted automatically in order to reach convergence in a predetermined number of iterations. In the 3D module, a CFL condition has to be satisfied for stability due to the semi-implicit scheme.

Finally, the discretized non-linear equations are solved with a Newton-Raphson iterative method [11].

CATHARE is written in Fortran 77 and it has a modular and object-oriented code structure, which enhance the flexibility of the code. In view of this, new models may be easily added without changing the main code structure.

The user can assemble different predefined modules to create a nodalization of the thermo-hydraulic circuit of interest. The main available modules are: a 1D (or axial) module used to represent pipes, a 0D (or volume) module for large-size plena (e.g. pressurizer, lower plenum in the reactor vessel) and a 3D module used for 3D-core modeling. To complete the nodalization of a circuit, these main modules may be connected to several sub-modules, such as: multi-layer wall, boundary conditions, CCFL, re-flooding and point kinetic neutronic modules.

The detailed description of the available modules and of the input deck definition is not reported here, but it can be found in [11].

In the following sections, the conservation equations and the main closure laws for the 1-D axial module are described. In the current work, the code version of CATHARE is v25_3 revision 2.1.

2.1 Conservation equations

The phasic mass, momentum and energy equations in CATHARE are obtained from the time- and space-average of the local instantaneous conservation equations. In the derivation, simplifications are introduced and the main ones [11] are:

- the axial heat conduction, the axial component of the viscous stress tensor and the axial mass diffusion are neglected;

- the work of the pressure distribution and the interfacial forces are neglected;
- the interface between the phases is assumed to have no thickness and no mass;
- the superficial tension gives no contribution to the momentum and to the energy equations;
- the velocity of the phases at the interface is assumed to be the same.

From the solution of the six conservation equations, the following variables are computed: the pressure p , the void fraction α , the liquid velocity \vec{v}_l , the gas velocity \vec{v}_g , the liquid enthalpy i_l and the gas enthalpy i_g .

The full system of equations is solved even if one of the two phases is not present [10]. To do so, the void fraction is only allowed to vary between 10^{-5} and $1 - 10^{-6}$ and the missing phase is assumed to be at the saturation temperature. This kind of approach is used to avoid numerical problems.

2.1.1 Mass conservation equations

The mass conservation equations for the gas and liquid phase read respectively:

$$\frac{\partial \alpha A \rho_g}{\partial t} + \frac{\partial \alpha \rho_g A v_g}{\partial z} = A \Gamma + S_g \quad (2.1)$$

$$\frac{\partial (1 - \alpha) A \rho_l}{\partial t} + \frac{\partial (1 - \alpha) \rho_l A v_l}{\partial z} = -A \Gamma + S_l \quad (2.2)$$

The interfacial mass transfer Γ takes into account the mass variation of vapor or liquid because of evaporation or condensation. The first term on the right-hand side of Eqn. 2.2 has a negative sign since the amount of liquid that evaporates must be subtracted from the liquid balance equation. The mass transfer due to evaporation or condensation is modeled as [11]:

$$\Gamma = \frac{\frac{P_h}{A} q_{wi} - q_{li}''' - q_{gi}'''}{i_g - i_l} + \Gamma_r \quad (2.3)$$

This equation includes the generation or condensation of steam due to the wall-to-interface heat flux q_{wi} , the liquid-to-interface volumetric heat transfer rate q_{li}''' and the gas-to-interface volumetric heat transfer rate q_{gi}''' .

In order to deal with the residual phase in the case of single-phase flow, the term Γ_r is introduced [10] and is equal to:

$$\Gamma_r = \begin{cases} -\rho_g \frac{\alpha - \alpha_{min}}{\Theta_g} & \text{if } \alpha < \alpha_{min} \text{ (i.e. vaporization)} \\ 0 & \text{if } \alpha_{min} < \alpha < \alpha_{max} \\ -\rho_l \frac{\alpha - \alpha_{max}}{\Theta_l} & \text{if } \alpha_{max} < \alpha \text{ (i.e. condensation)} \end{cases} \quad (2.4)$$

where $\Theta_g = \Theta_l = 10^{-5}$. In the case of a liquid single-phase flow, the residual mass transfer allows to avoid the condensation of the residual steam and α becomes equal to α_{min} . On the other hand, if a vapor single-phase flow is simulated, the evaporation of the residual liquid does not occur and α tends to α_{max} .

2.1.2 Momentum conservation equations

The momentum conservation equations for the gas (2.5) and liquid phase (2.6) are written in secondary form:

$$\begin{aligned} \alpha\rho_g A \left[\frac{\partial v_g}{\partial t} + v_g \frac{\partial v_g}{\partial z} \right] + A\alpha \frac{\partial p}{\partial z} + Ap_i \frac{\partial \alpha}{z} + A\beta\alpha(1-\alpha)\rho_m \left[\frac{dv_g}{dt} - \frac{dv_l}{dt} \right] \\ = A\alpha\rho_g g + A\Gamma(v_i - v_g) - A\tau_i - P_f C_g \rho_g \frac{v_g |v_g|}{2} - K_{loc} \alpha \rho_g \frac{v_g |v_g|}{2} \\ + R \frac{(1-\alpha)}{4} p_i \frac{\partial A}{\partial z} + SM_g \end{aligned} \quad (2.5)$$

$$\begin{aligned} (1-\alpha)\rho_l A \left[\frac{\partial v_l}{\partial t} + v_l \frac{\partial v_l}{\partial z} \right] + A(1-\alpha) \frac{\partial p}{\partial z} + Ap_i \frac{\partial(1-\alpha)}{z} \\ - A\beta\alpha(1-\alpha)\rho_m \left[\frac{dv_g}{dt} - \frac{dv_l}{dt} \right] = A(1-\alpha)\rho_l g - A\Gamma(v_i - v_l) \\ + A\tau_i - P_f C_l \rho_l \frac{v_l |v_l|}{2} - K(1-\alpha)\rho_l \frac{v_l |v_l|}{2} + R \frac{\alpha}{4} p_i \frac{\partial A}{\partial z} + SM_l \end{aligned} \quad (2.6)$$

The material derivative, defined as $\frac{d}{dt} = \frac{\partial}{\partial t} + v \frac{\partial}{\partial z}$, is used in the added mass term (i.e. the last term in the left-hand side of the equations), which models the effect of the inertial forces. In the right-hand side of the equations, the following terms are modeled, respectively: the gravity, the interfacial momentum transfer, the interfacial friction, the wall friction, the friction due to singularities, the momentum transfer due to flow stratification and a further possible source term.

Under the assumption that there is no relative motion between the interface and the gas bubbles at low void fraction and between the interface and the liquid droplets at high void fraction, the interfacial velocity v_i can be expressed as:

$$v_i = \alpha v_l + (1-\alpha)v_g \quad (2.7)$$

The mixture density is defined as:

$$\rho_m = \alpha\rho_G + (1-\alpha)\rho_L \quad (2.8)$$

The coefficient β contained in the added mass terms can be modeled as:

$$\beta = 0.5(1-R)A_1 \quad (2.9)$$

The coefficient A_1 depends on the entrainment rate E and on the void fraction α [11]. The coefficient R is related to the degree of stratification of the flow. In the case of a stratified flow R is equal to 1 and β is zero, so no contribution from the added mass term goes in to the momentum equations. Besides, β is also zero when the flow or the geometry of the system are annular. The singular pressure drop coefficient K_{loc} , which describes the pressure effects due to changes in duct geometry, is computed with empirical correlations or imposed by the user. The other unknown quantities are modeled by specific closure laws, which are discussed in Section 2.2.

2.1.3 Energy conservation equations

The energy conservation equations for the gas (2.10) and liquid (2.11) phase are written in primary form:

$$\begin{aligned} \frac{\partial \alpha \rho_g A (i_g + \frac{1}{2} v_g^2)}{\partial t} + \frac{\partial \alpha \rho_g A v_g (i_g + \frac{1}{2} v_g^2)}{\partial z} - A \alpha \frac{\partial p}{\partial t} \\ = A [Q_{gi} + \alpha \rho_g v_g g] + P_h q_{wg} + S E_g \end{aligned} \quad (2.10)$$

$$\begin{aligned} \frac{\partial (1 - \alpha) \rho_l A (i_l + \frac{1}{2} v_l^2)}{\partial t} + \frac{\partial \alpha \rho_l A v_l (i_l + \frac{1}{2} v_l^2)}{\partial z} - A (1 - \alpha) \frac{\partial p}{\partial t} \\ = A [Q_{li} + (1 - \alpha) \rho_l v_l g] + P_h q_{wl} + S E_l \end{aligned} \quad (2.11)$$

where:

$$Q_{gi} = q_{gi}''' + \Gamma \left(i_g + \frac{1}{2} v_i^2 \right) \quad (2.12)$$

$$Q_{li} = q_{li}''' - \Gamma \left(i_l + \frac{1}{2} v_i^2 \right) \quad (2.13)$$

The interfacial volumetric heat transfer rates (i.e. q_{li}''' and q_{gi}''') and the wall to fluid heat fluxes (i.e. q_{wl} and q_{wg}) will be discussed in the following sections.

2.1.4 Non-condensable gas balance equations

Up to 4 non-condensable gases can be modeled according to the transport equation [11]:

$$\frac{\partial \alpha \rho_g A X_i}{\partial t} + \frac{\partial \alpha \rho_g A v_g X_i}{\partial z} = S_i \quad (2.14)$$

where X_i and S_i are the mass fraction and the source term for the species i , respectively.

The non-condensable gases are treated as *ideal gases*, with an uniform distribution with respect of the flow area and constant specific heat capacity $c_{p,i}$. All the gases are considered to have the same axial mean velocity v_g and temperature $T_g = T_v$ (i.e. the temperature of the gases is the same of the vapor/steam).

2.2 Closure laws

Several closure laws are required in order to solve the set of conservation equations. These closure models can be based on physical considerations and/or empirical data from appropriate experiments. Moreover, they are usually valid and applicable for a limited range of system conditions and for specific geometries.

In this section, the main closure laws implemented in the standard version of CATHARE are discussed.

2.2.1 Flow pattern transition

A typical representation of the flow pattern map used in CATHARE is shown in Figure 2.2.

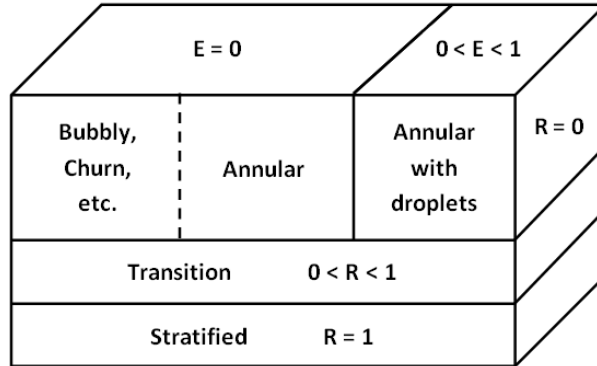


Figure 2.2: Flow pattern map in CATHARE.

The selection of the flow regimes is based on the entrainment rate E and the degree of stratification R . The transition between stratified and non-stratified flow and the transition between annular and droplet flow are explicitly modeled (full lines between these flow regimes in the map). The transition between the bubbly, churn and the annular flow (dashed line in the figure) is otherwise based on void fraction criteria and it is taken into account only for the interfacial friction and heat transfer. This has the advantage of a more robust and simpler code structure.

Stratification modeling

The stratification may be relevant in horizontal and inclined pipes and in pools. This phenomenon leads to a separation between the liquid and gas phase with a significant impact on the interfacial area, the interfacial momentum transfer and the interfacial energy transfer.

It is modeled through the use of two coefficients, namely the degree of stratification R and the interfacial pressure p_i .

R ranges between 0 for non-stratified flows and 1 for stratified flows .

The interfacial pressure is expressed as:

$$p_i = p_{i,h}(\beta) + R(p_{i,st} + p_{i,h0}) \quad (2.15)$$

where $p_{i,h}$ and $p_{i,h0}$ are numerical corrections which guarantees the hyperbolicity of the momentum equation in an unconditional way [12]. The stratified interfacial pressure is defined as the difference between the pressure at the interface and the average pressure and it reads:

$$p_{i,st} = \begin{cases} \alpha(1 - \alpha)(\rho_L - \rho_G)g_{\perp}D_h & \text{if } g_{\perp} > \frac{9.81}{2} \text{ or } 30^{\circ} < \theta < 150^{\circ} \\ 0 & \text{if } g_{\perp} < \frac{9.81}{2} \text{ or } \theta < 30^{\circ} \end{cases} \quad (2.16)$$

As seen from Eqn. 2.16, the stratification is not allowed for $\theta < 30^{\circ}$ and for $\theta > 150^{\circ}$. This choice is mainly due to numerical reasons. The angle Θ along with the gravity vector is indicated in Figure 2.3.

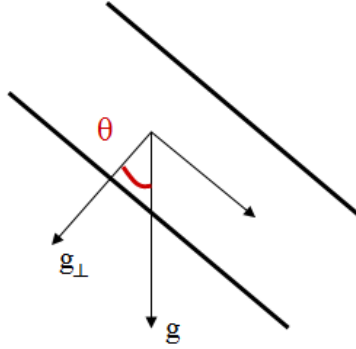


Figure 2.3: Gravity vector and notation.

A detailed description of the stratification modeling [11] is not reported here, since only non-stratified flows will be analyzed in this study.

Entrainment modeling

The phenomenon of entrainment consists of the entrapment of liquid droplets into the gas flow and it occurs at high void fractions. In CATHARE, the rate of entrainment E is modeled with the Sten-Wallis correlation and it can vary between 0 (no entrainment) and 1 (as in the case of dry-out conditions in a heated channel) [11] [12].

In the experiments used in this study, the entrainment rate is always zero.

2.2.2 Momentum transfer: Interfacial friction

The interfacial friction is an important parameter for the determination of the void fraction distribution. The interfacial friction term is modeled in a general form as:

$$\tau_i = \frac{1}{2} a_i f_i \rho \Delta v_2 k(\alpha) \quad (2.17)$$

where f_i is the interfacial friction coefficient, a_i is the volumetric interfacial area and $k(\alpha)$ is a numerical smoothing function, which avoids numerical problems when one phase tends to disappear [11]. The squared velocity difference Δv_2 is approximated as:

$$\Delta v_2 \simeq (\Delta v)^2 = (v_g - C_k v_l)^2 \quad (2.18)$$

where C_k is derived from the Wallis Drift Flux model and is equal to:

$$C_k = 1 + 1.6\alpha^{1.5}(1 - \alpha)^{1.5} \quad (2.19)$$

Numerical corrections are implemented in the code; details may be found in [11].

Interfacial friction for non-stratified flows

In order to obtain the interfacial friction term for non-stratified flows, two different models are combined:

$$\tau_{i,nst} = (\tau_{i,1} + \tau_{i,2})k(\alpha) \quad (2.20)$$

The term $\tau_{i,1}$ is related to bubbly-slug-churn flow patterns and its correlation is based on a drift-flux approach. It is implemented in three different forms, namely for tube, rod bundle and annulus geometry.

The second term $\tau_{i,2}$ was developed for annular flow patterns with possible entrainment. Therefore, it depends on the rate of entrainment E , the drag coefficient C_D and the droplet diameter δ [11].

Interfacial friction for stratified and transition flows

For the case of stratified flows, the general formulation of Eqn. (2.17) is still valid. As mentioned above, stratified flows are not of interest in this study. Thus, details on the modeling are not provided, but they may be found in [11].

The interfacial friction for transition flows is computed as an arbitrary blending between the formulation for a stratified $\tau_{i,st}$ and non-stratified flow $\tau_{i,nst}$.

$$\begin{aligned}\tau_i &= f(R)|\tau_{i,st}| + [1 - f(R)]|\tau_{i,nst}| \\ f(R) &= R^2(3 - 2R)\end{aligned}\tag{2.21}$$

2.2.3 Momentum transfer: Wall friction

In Eqn. (2.5) and (2.6), the wall friction terms contain the quantities C_g and C_l which also need closure laws.

The non-dimensional friction factors for the gas and liquid phases are respectively:

$$C_g = c_g f_g\tag{2.22}$$

$$C_l = c_l f_l\tag{2.23}$$

The single-phase Fanning friction coefficient f_g is expressed in terms of the Reynolds number Re_g :

$$f_g = \max\left(\frac{16}{Re_g}, \frac{0.079}{Re_g^{0.25}}, 0.003\right)\tag{2.24}$$

where the first quantity is valid for laminar flows and the second one is the Blasius correlation which is valid for turbulent flows in smooth pipes. Similarly, the coefficient f_l for the liquid depends on Re_l and it is equal to:

$$f_l = \max\left(\frac{16}{Re_l}, \frac{0.079}{Re_l^{0.25}}, 0.003\right)\tag{2.25}$$

A more detailed description of the single-phase coefficients is presented in Chapter 4.

The two-phase multipliers c_g and c_l depend on the stratification and entrainment rate, so:

$$c_g = R c_{g,st} + (1 - R) c_{g,nst}\tag{2.26}$$

$$c_l = [R c_{l,st} + (1 - R) c_{l,nst}] g(\alpha)\tag{2.27}$$

where $g(\alpha)$ is a numerical correction which eliminates the liquid contribution to the wall friction when the void fraction is very close to 1. The two-phase multipliers for stratified flows read:

$$\begin{aligned} c_{l,st} &= \frac{1}{\pi} \arccos(2\alpha - 1) \\ c_{g,st} &= 1 - c_{l,st} \end{aligned} \quad (2.28)$$

while the following expression is used for non-stratified flows:

$$\begin{aligned} c_{l,nst} &= c_{l,nst1}^{(1-e)} \cdot c_{l,nst2}^e \\ c_{g,nst} &= \alpha^{1.25} \end{aligned} \quad (2.29)$$

The parameter $c_{l,nst2}$ is the two-phase multiplier for the case of annular flows with entrainment. Its expression is consistent with the modified Lockhart-Martinelli model for high pressure [11]. The parameter $c_{l,nst1}$ is for bubbly, slug, churn and annular flows and is equal to:

$$c_{l,nst1} = \frac{(1 - \alpha)\rho_l}{\alpha\rho_g + (1 - \alpha)\rho_l} \quad (2.30)$$

The parameter e is a function of the entrainment rate E . It is zero for $E = 0$ and it goes to 1 for large values of E .

2.2.4 Interfacial heat transfer

The interfacial heat transfer models regulates the formation of void fraction during evaporation and condensation. The possible liquid superheat is used for the formation of steam through the liquid-to-interface volumetric heat rate q_{li}''' , so that the liquid returns to saturation conditions in a short time (i.e. to a condition of thermal equilibrium). Nevertheless, thermal non-equilibrium may occur in conditions such that the time-scales of the thermal-hydraulic phenomenon are shorter or equal to the time-scales for vaporization. An example is the rapid depressurization due to a pipe break in the primary system of a PWR with the consequent flashing of the coolant.

On the other hand, the production of steam in a sub-cooled liquid is condensed and it reduces the thermal non-equilibrium between the two phases.

These kinds of phenomena are very important in the transient analysis of nuclear reactors, thus an accurate modeling of the interfacial heat transfer is needed.

In CATHARE, the models for evaporation and condensation with or without non-condensable gases are different. For the purpose of the thesis, only the case without non-condensable gases is briefly described.

It should be noticed that all the models implemented in CATHARE were validated against appropriate experiments, as discussed in [12] and [5].

Liquid-to-interface heat transfer

If no condensable gases are present, two possible situations may occur:

- $T_l < T_{sat}(p) \implies \text{Condensation}$
- $T_l > T_{sat}(p) \implies \text{Flashing}$

The flashing is modeled with a semi-empirical correlation obtained from critical flashing experiments in long nozzles at CEA [12].

Condensation is important in situations where steam is discharged in sub-cooled water as well as in sub-cooled boiling where the generated bubbles are condensed in the sub-cooled liquid bulk. The condensation model in CATHARE is given as:

$$q_{li,cond}''' = Rq_{li,st}''' + (1 - R) \left[C_S q_{li,Chen}''' + (1 - C_S) q_{li,Shah}''' + E q_{li,E}''' \right] \quad (2.31)$$

In this equation, different contributions are taken into account.

The term $q_{li,st}'''$ is obtained with a correlation based on COSI tests for stratified flows [12].

The term $q_{li,E}'''$ is estimated with a correlation valid for annular flows with entrainment and it is developed from a conduction model for an entrained droplet.

The term $q_{li,Chen}'''$ is calculated with a modified Chen correlation and it is valid for annular flows without entrainment.

The term $q_{li,Shah}'''$ comes from a modified-Shah correlation. In the original publication [13], the correlation was developed for the condensation of steam due to wall cooling. It was then adapted for the modeling of the interfacial condensation and it has been validated for steam quality lower than 0.85 [11]. It is interesting to notice that the volumetric condensation rate is linearly dependent on the liquid sub-cooling ($T_{sat} - T_l$).

Finally, C_S is a balance coefficient that allows a smooth transition between the Shah and Chen correlations. It is therefore used to model the transition from bubbly-slug-churn to annular flow. The smooth function is a function of the duct hydraulic diameter D_h . In Figure 2.4, the case with $D_h < 20$ mm is represented. It shows that the condensation is modeled with Shah correlation for $\alpha < 0.85$ (since $C_S = 0$) and with Chen correlation for $\alpha > 0.9$ (since $C_S = 1$)

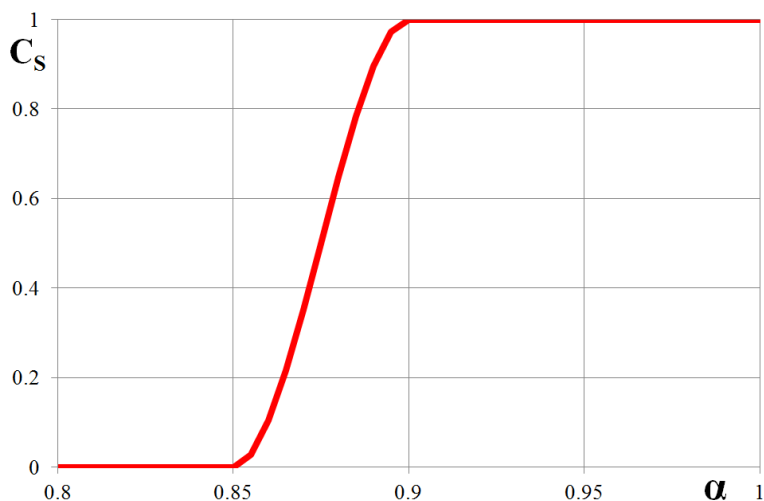


Figure 2.4: Balance coefficient between Shah and Chen correlation for $D_h < 20$ mm.

Interface-to-gas heat transfer

Similarly to the liquid-to-interface heat transfer, two possible situations may occur:

- $T_g > T_{sat}(p) \implies$ *Vaporization*
- $T_g < T_{sat}(p) \implies$ *Condensation*

When the steam is superheated, energy is transferred from the gas, through the interface, to the liquid with vaporization of the latter. This is, for instance, one of the heat transfer mechanisms involved in the reflooding phase of a LOCA. The vaporization in CATHARE is modeled as:

$$q_{gi,vap}''' = Rq_{gi,st}''' + (1 - R) [1 - R_{an}(1 - E)] q_{gi,bsc}''' + R_{an}(1 - E)q_{gi,an}''' \quad (2.32)$$

where $q_{gi,st}'''$ counts the contribution of stratified flows, $q_{gi,an}'''$ is valid for annular flows without entrainment, $q_{gi,bsc}'''$ is for bubbly, slug and churn flows and R_{an} is the rate of annular flow.

The terms $q_{gi,st}'''$, $q_{gi,bsc}'''$ and $q_{gi,an}'''$ are linearly dependent on $(T_{sat} - T_g)$, which indicates that $q_{gi,vap}''' < 0$.

The rate of annular flow ranges between 0 (for non-annular flows) and 1 (for annular flows). As the balance coefficient C_S , it allows a smooth transition between the bubbly-slug-churn to the annular flow region. The smooth transition occurs for void fractions between 0.8 and 0.9.

In case of condensation, the following formulation is used:

$$q_{gi,cond}''' = \left[q_{gi,vap}''' + 10^8 R(T_g - T_{sat}(p))^2 \right] F(x_g) \quad (2.33)$$

The second term in the equation represents the enhancement of the heat transfer coefficient due to the formation of several small liquid droplets in the condensing steam. The function $F(x_g)$ is a function of the steam quality x_g . It is equal to 1 for $x_g > 0.5$ and it goes smoothly to 0 in the range $0 < x_g < 0.5$, so that the condensation is inhibited for low mass quality flows. In this case, $q_{gi,cond}''' > 0$.

2.2.5 Wall Heat transfer

The temperature of the cladding (or more in general, of the wall surfaces) is one of the key safety parameters in the analysis of nuclear reactor transients. The prediction requires several empirical models which are used as closure laws in the energy conservation equations (2.10) and (2.11). These models are briefly presented in this section.

The structure of the CATHARE code is based on the typical Nukiyama boiling curve [14], whose sketch is displayed in Figure 2.5.

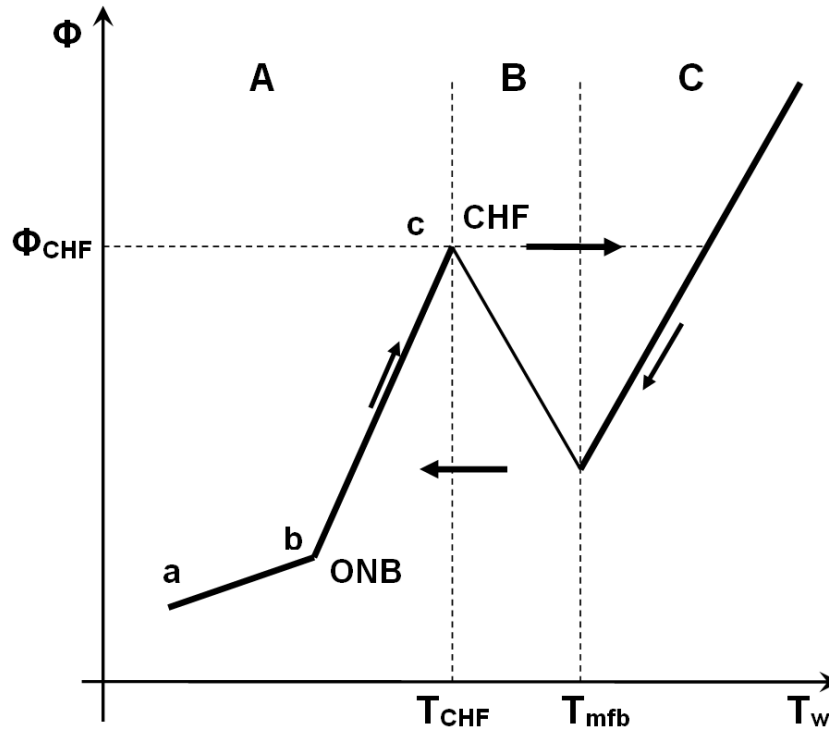


Figure 2.5: Boiling curve schematic.

Accordingly to the figure, three main heat transfer regions can be identified:

- the Pre-CHF region **A** where the liquid is in contact with the heated wall;
- the transition zone **B** where an unstable vapor layer is formed on the heated surface;
- the Post-CHF region **C** where the heated wall is insulated by a continuous layer of vapor;

Region **A** is further divided in: the single-phase heat transfer (segment **a-b** in Figure 2.5) and the sub-cooled and nucleate boiling region (segment **b-c**), that starts with the Onset of Nucleate Boiling. At point **c**, the nucleate boiling region ends. If the heat flux exceeds the so-called Critical Heat Flux ϕ_{CHF} , a boiling crisis occurs and the wall temperature drastically increases because of the loss of direct contact between the liquid phase and the heated surface. In region **C**, film boiling is established and several complex heat transfer mechanisms come into play (e.g. single-phase heat transfer to the gas phase and radiation heat transfer to the liquid and gas phase). If the heat flux is reduced in region **C**, an hysteresis phenomenon is observed which causes a delayed re-wetting of the wall surfaces due to the high temperatures and the presence of a vapor layer attached to the walls. The film boiling regime is therefore maintained until the temperature falls below the minimum film boiling temperature (i.e. T_{mfb} in the figure).

In the next subsections, the modeling of the pre-CHF heat transfer in CATHARE is presented. First, the implementation of the convective and nucleate boiling terms is explained. The computational scheme in CATHARE, which combines the convection

and nucleate boiling term, is then discussed in Section 2.2.5.4. Finally, the model for the critical heat flux is briefly presented.

2.2.5.1 Convection heat transfer

The standard definition of the convective heat transfer is:

$$q_{conv} = h_{conv} \Delta T \quad (2.34)$$

where h is the heat transfer coefficient and ΔT is a temperature difference.

To have a more practical and robust algorithm, the convective heat transfer term is included in the modeling of the whole pre-CHF region. Therefore, it is used for the single-phase convection, the sub-cooled boiling and the saturated boiling. In single-phase convection, the term obviously describes the proper heat transfer mechanism. In sub-cooled boiling, the term still gives a contribution, together with the nucleate boiling term, to the total heat transfer. However, the temperature difference is chosen in an artificial manner, so that a continuous transition from sub-cooled and saturated boiling is ensured. As regards the saturated boiling, the convective term has no impact, but it is held in the model with the temperature difference arbitrarily set to zero. According to this implementation strategy, the temperature difference is modeled as:

$$\Delta T = \begin{cases} T_w - T_l & \text{if } T_w < T_{sat} \text{ (Single-phase)} \\ T_{sat} - T_l & \text{if } T_l < T_{sat} < T_w \text{ (Sub-cooled boiling)} \\ 0 & \text{if } T_{sat} < T_l < T_w \text{ (Saturated boiling)} \end{cases} \quad (2.35)$$

The heat transfer coefficient h for single-phase liquid convection is strongly influenced by the flow regime (laminar or turbulent), so that different correlations have to be employed. In CATHARE, this coefficient is determined as the maximum of four different values:

$$h_{conv} = \max(h_{lam,NC}; h_{turb,NC}; h_{lam,FC}; h_{turb,FC}) \quad (2.36)$$

where $h_{lam,NC}$ indicates the heat transfer coefficient for the laminar natural convection, $h_{turb,NC}$ the turbulent natural convection, $h_{lam,FC}$ the laminar forced convection and $h_{turb,FC}$ the turbulent forced convection. The estimation of these coefficients is based on the properties of the liquid phase.

The different heat transfer coefficients are obtained from empirical correlations, which compute the Nusselt number, defined as:

$$Nu = \frac{h_{conv} D_{h,l}}{k_l} \quad (2.37)$$

The diameter $D_{h,l}$ is a modification of the standard hydraulic diameter $D_h = \frac{4A}{P_w}$ and it reads:

$$D_{h,l} = D_h(1 - \sqrt{\alpha} F_{num}) \quad (2.38)$$

This modification implies that $D_{h,l} = D_h$ in single-phase flows, while the effective hydraulic diameter for the liquid phase is reduced with increasing void fraction. This is

particularly important for annular flows where $D_{h,l}$ indicates the liquid film thickness. F_{num} is a numerical correction, which limits the minimum liquid film thickness to the value $10^{-3}D_h$.

Natural convection

The natural convection arises when the flow is driven by the only variation of the fluid density along the circuit and no external pump is used.

In CATHARE, the heat transfer correlation for natural convection is:

- for laminar flow

$$Nu_{lam,NC} = 0.55(Ra)^{1/4} \quad (2.39)$$

- for turbulent flow

$$Nu_{turb,NC} = 0.13(Ra)^{1/3} \quad (2.40)$$

The Rayleigh number is defined as:

$$Ra = GrPr \quad (2.41)$$

where Gr is the Grashof number and Pr is the Prandtl number. The Grashof number describes the buoyancy effects and its expression in CATHARE is:

$$Gr = \frac{g\beta_l\rho_l^2 D_{h,l}^3}{\mu_l^2} \cdot |T_w - T_l| \quad (2.42)$$

where β_l is the volumetric expansion coefficient:

$$\beta_l = -\frac{1}{\rho_l} \left(\frac{\partial \rho_l}{\partial T_l} \right)_p \quad (2.43)$$

and represents the variation of density of the fluid with the temperature, at constant pressure.

The Prandtl number reads:

$$Pr = \frac{c_{p,l}\mu_l}{k_l} \quad (2.44)$$

These formulas are consistent with the literature [15].

Forced convection

The heat transfer coefficient in laminar flows is constant and does not depend on the Reynolds and Prandtl number. In CATHARE, the laminar forced-convection Nusselt number is:

$$Nu_{lam,FC} = 3.66 \quad (2.45)$$

Kakaç [16] refers to Eqn. (2.45) as the correlation valid for circular ducts with constant wall temperature boundary conditions. For imposed heat flux, another relationship is provided, i.e. [16]:

$$Nu = 4.36 \quad (2.46)$$

Eqn. (2.45) is therefore conservative when applied to pipes with imposed heat flux boundary conditions.

The turbulent forced-convection heat transfer coefficient is modeled with the Dittus-Boelter equation [17]:

$$Nu_{turb,FC,DB} = 0.023Re^{0.8}Pr^{0.4} \quad (2.47)$$

where the Reynolds is defined as:

$$Re = \frac{\rho_l v_l D_{h,l}}{\mu_l} \quad (2.48)$$

To extend the use of Eqn. 4.18 to the case of two-phase flows, a correction at high void fraction is introduced in CATHARE. Thus, the final expression of the heat transfer coefficient under conditions of turbulent forced convection is:

$$h_{turb,FC} = (1 - C_S)h_{turb,FC,DB} + 2C_S h_{li,Chen} \quad (2.49)$$

where $h_{li,Chen}$ is the Chen heat transfer coefficient and C_S is the coefficient discussed in Section 2.2.4. The correction is active only for $\alpha > 0.85$, as shown in Figure 2.4.

2.2.5.2 Nucleate boiling

The nucleate boiling heat transfer is derived from Thom correlation [18]:

$$\Delta T_{sat} = 22.65 \left(\frac{\phi}{10^6} \right)^{0.5} e^{\left(-\frac{1}{87} \frac{p}{10^5} \right)} \quad (2.50)$$

where the wall superheat $\Delta T_{sat} = T_w - T_{sat}$ and ϕ is the imposed heat flux at the wall surface. The correlation was developed for a 12.7 mm vertical tube with upward water velocities between 1.5 and 6.1 m/s , pressures between 5.17 and 13.78 MPa and heat fluxes between 0.284 and 1.58 MW/m^2 .

In CATHARE, the nucleate boiling heat flux is therefore computed as:

$$q_{nb} = 1.97 \cdot 10^3 e^{(2.3 \cdot 10^{-7} p)} (T_w - T_{sat})^2 \quad (2.51)$$

2.2.5.3 Net Vapor Generation

The heating of sub-cooled water may be considered. The Net Vapor Generation (NVG) (or Onset of Significant Void (OSV)) corresponds to the point at which the amount of bubbles (so void) becomes significant. This is associated to the fact that bubbles starts to detach from the heated walls. In this condition, the heat is transferred from the wall to the fluid by sub-cooled boiling since the bulk of the fluid is still below the saturation temperature.

In CATHARE, the NVG criterion indicates the point at which vaporization at the heated walls starts, so that the void fraction becomes larger than zero (see also Section 2.2.5.4). The liquid sub-cooling at the NVG point is then calculated as:

$$\delta i_c = \text{Max}(\delta i_c^*; \delta i) \quad (2.52)$$

$$\delta i_c^* = \begin{cases} 5 \frac{\phi}{k_l} \frac{c_{p,l}}{Pe_0} \frac{D_{hl}}{65 \cdot 10^{-4}} & \text{if } Pe < 0.52 Pe_0 \\ 2 \frac{\phi}{k_l} \frac{c_{p,l}}{Pe_0} \frac{D_{hl}}{65 \cdot 10^{-4}} \left(\frac{Pe}{Pe_0} \right)^{1.4} & \text{if } Pe \geq 0.52 Pe_0 \end{cases} \quad (2.53)$$

where $Pe_0 = 7 \cdot 10^4$ and the term $\delta i = 10^4$ has been introduced for numerical reasons. The Peclet number is defined as:

$$Pe = RePr \quad (2.54)$$

The liquid sub-cooling is expressed in terms of enthalpy, so that the criterion for the net vapor formation becomes $\Delta i_{sub} = i_{l,sat} - i_l \leq \delta i_c$.

This NVG criterion is a modified version of the Saha-Zuber correlation [19]. It was developed and validated at CEA-Grenoble using KIT experiments, which were performed at the Moscow Power Engineering Institute in 1974 [20]. The range of the qualification was: $340 < G < 2100 \frac{kg}{m^2 s}$, $4.4 < p < 11$ MPa and $0.43 < \phi < 1.72 \frac{MW}{m^2}$.

2.2.5.4 Global CATHARE scheme for the pre-CHF region

For the purpose of modeling the heat transfer in the pre-CHF region, the total heat flux ϕ imposed on the wall can be divided in two parts: one heats up the liquid phase (q_{wl}) and the other one vaporizes the liquid (q_{wi}). In view of this, the following relationship can be written:

$$\phi = q_{wl} + q_{wi} \quad (2.55)$$

Thus, the modeling of the wall heat transfer in CATHARE can be summarized as:

- Single-phase:

$$T_w < T_{sat} \quad \Longrightarrow \quad \begin{cases} q_{wl} = q_{conv} \\ q_{wi} = 0 \end{cases} \quad (2.56)$$

- Sub-cooled boiling:

$$T_l < T_{sat} < T_w \quad \Longrightarrow \quad \begin{cases} q_{wl} = q_{conv} + (1 - \epsilon)q_{nb} \\ q_{wi} = \epsilon q_{nb} \end{cases} \quad (2.57)$$

- Saturated boiling:

$$T_l > T_{sat} \quad \Longrightarrow \quad \begin{cases} q_{wl} = 0 \\ q_{wi} = q_{nb} \end{cases} \quad (2.58)$$

In the single-phase region, only the convection heat transfer mechanism is present and the wet wall temperature is found from Eqn. (2.34) and (2.36):

$$T_w = T_l + \frac{\phi}{h_{conv}} \quad (2.59)$$

In the saturated boiling region, the nucleate boiling heat transfer mechanism is the predominant one, so that the wall superheat is simply determined with Thom correlation (see Eqn. (2.50)).

The modeling of the sub-cooled boiling region is more complex and both heat transfer mechanisms co-exist, as shown in Eqn. (2.57). The wall-to-liquid heat flux is a combination of the convective heat flux calculated with Eqn. (2.35) (where $\Delta T = T_{sat} - T_l$) and the nucleate boiling heat flux calculated with Eqn. (2.51).

The distribution parameter ϵ determines the rate of vaporization in sub-cooled boiling q_{wi} . It is based on the NVG correlation and it is computed as:

$$\epsilon = \begin{cases} 1 & \text{if } i_l - i_{l,sat} > \delta i \\ 1 - (\delta i_{aux} - 1)^6 \cdot (1 + 6 \cdot \delta i_{aux}) & \text{if } -\delta i_c < i_l - i_{l,sat} < \delta i \\ 0 & \text{if } i_l - i_{l,sat} < -\delta i_c \end{cases} \quad (2.60)$$

$$\delta i_{aux} = Max \left(0; \frac{\delta i_c + (i_l - i_{l,sat})}{\delta i_c + \delta i} \right) \quad (2.61)$$

The form of the function ϵ has no physical meaning, but it was observed to provide correct results in the simulation of the KIT experiments [20]. Furthermore the continuity of the heat fluxes and wall temperatures is ensured by this computation scheme. The typical form of the ϵ parameter function is shown in Figure 2.6.

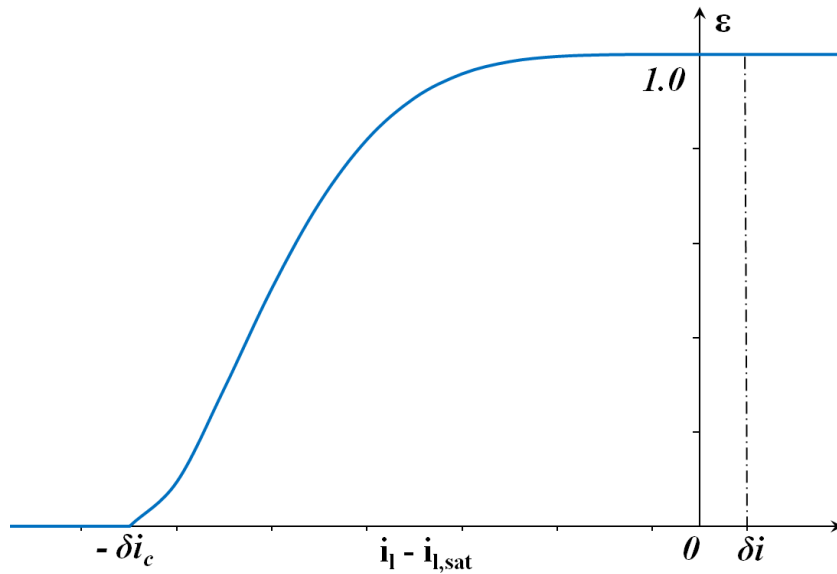


Figure 2.6: Typical form of the ϵ parameter function.

In the case of a vertical pipe with imposed uniform heat flux and forced flow, a typical CATHARE prediction of the wall and liquid temperatures together with the void fraction profile is depicted in Figure 2.7.

It is possible to distinguish four different regions:

- the region **A-B** with single-phase (liquid) heat transfer. The wall temperature is estimated with Eqn. (2.59) and the void fraction α is equal to zero.
- the region **B-D** of sub-cooled boiling where $T_w > T_{sat}$ and $\Delta T = T_{sat} - T_l$. Although some bubbles are in reality generated, they do not detach from the wall. The NVG point has not been reached yet, so $\epsilon = 0$ and no vaporization occurs (i.e. $\alpha = 0$)

- the region **D-G** of sub-cooled where the NVG point is reached. Then the liquid starts to vaporize and the void fraction becomes non-zero. In these conditions, the rate of vaporization and condensation (due to the sub-cooled bulk) compete between each other, determining the net void fraction generation.
- the region **G-H** with saturated boiling. The wall temperature is predicted with the correlation of Thom, as given in Eqn. (5.5).

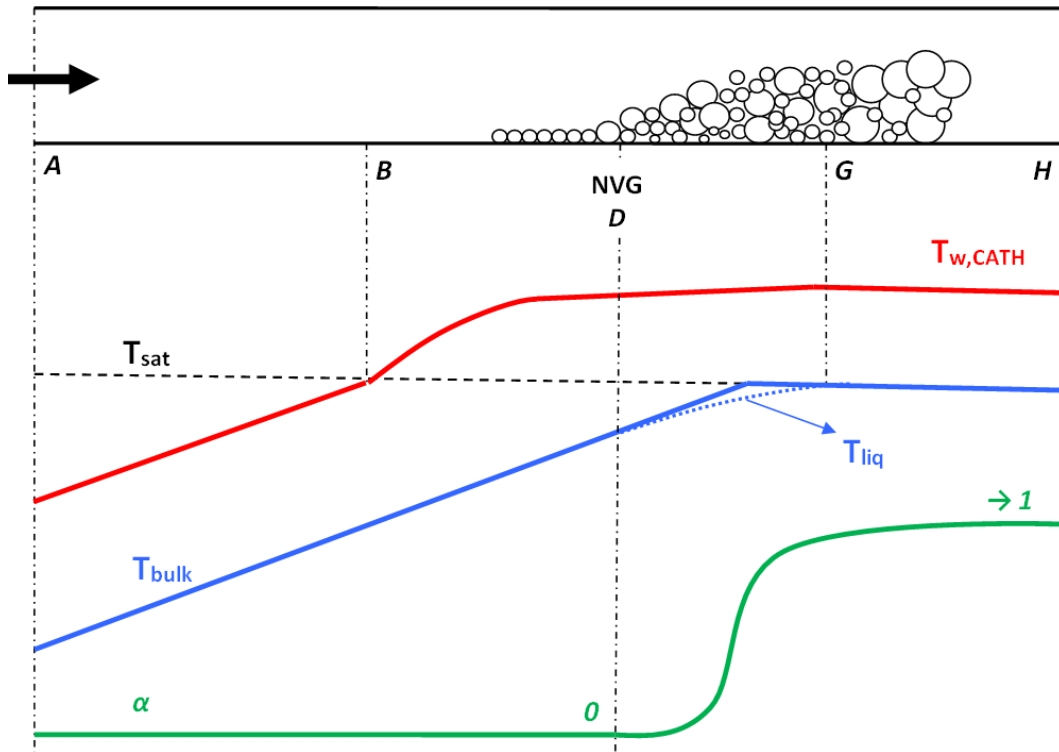


Figure 2.7: Flow boiling schematic in CATHARE.

The unphysical temperature jump, which can be observed at the beginning of the sub-cooled boiling region (i.e. in region B-D), is caused by the arbitrary definition of the temperature difference for the convection term.

2.2.5.5 Critical Heat Flux

The walls remains wet until the CHF conditions are reached. At this point, the heat transfer coefficient suddenly drops and the wall temperature significantly rises causing eventually the damage of the heated wall. It is therefore very important to accurately predict CHF.

For the determination of the critical heat flux, CATHARE uses the 1986 AECL-UO CHF lookup tables built up by Groeneveld [21] for circular pipes with diameter equal to 8 mm. The lookup tables are interpolated using cubic splines, given the local values of mass flux, pressure, and steam quality. The mass flux G is defined as the void fraction weighted average of the liquid and gas mass fluxes:

$$G = |G_g| + |G_l| = |\alpha\rho_g v_g| + |(1 - \alpha)\rho_l v_l| \quad (2.62)$$

The steam quality \bar{x} is computed as:

$$\begin{aligned}\bar{x} &= \frac{\alpha\rho_g + (1 - \alpha)\rho_l x}{\alpha\rho_g + (1 - \alpha)\rho_l} \\ x &= \frac{i_l - i_{l,sat}}{i_{lg}}\end{aligned}\tag{2.63}$$

The interpolated value $q_{CHF,interp}(G, p, \bar{x})$ is then corrected as:

$$\begin{aligned}q_{CHF} &= F_1 F_2 F_3 q_{CHF,interp}(G, p, \bar{x}) \\ F_1 &= Max \left(\frac{8.0 \cdot 10^{-3}}{D_h} ; 0.79 \right)^{\frac{1}{3}} \\ F_2 &= \begin{cases} 1 & \text{standard value} \\ 0.6 & \text{rod bundle} \end{cases} \\ F_3 &= \begin{cases} 1 & \text{if } \bar{x} < 0.9 \\ 10 (1 - \bar{x}) & \text{if } \bar{x} \geq 0.9 \end{cases}\end{aligned}\tag{2.64}$$

where F_1 is a geometric correction for hydraulic diameters different than 8 mm, F_2 corrects the values for rod bundles and F_3 represents a numerical linear correction which imposes $q_{CHF} = 0$ for $\bar{x} = 1$ and avoids negative values of the CHF.

The applicability range of the table in CATHARE is: $0.2 < p < 20$ MPa, $0 < G < 7500 \frac{kg}{m^2s}$ and $-0.15 < \bar{x} < 1$. The negative qualities refer to sub-cooled conditions.

Chapter 3

The SULTAN-JHR experiments

The SULTAN-RJH experimental program was performed at CEA Grenoble (France) during the years 2001-2008.

The main objective was to provide a reliable set of data for the validation of the thermal-hydraulic system code CATHARE in respect of the JHR core. Therefore, the geometry of the test sections was designed to have gap sizes and hydraulic diameters representatives of the JHR core channels. A rectangular geometry was chosen to avoid the technical difficulties in building a test section with curved plates (such as in JHR). The curvature of the plates in JHR is however relatively small, so that it is believed to influence only marginally the flow and the heat transfer.

The experimental ranges of the system parameters are reported in Table 3.1. It was selected according to the possible nominal and accidental flow conditions in the reactor.

Table 3.1: System conditions in the SULTAN-JHR experiments.

Outlet pressure [MPa]	0.2 – 0.9
Inlet water temperature [°C]	25 – 160
Mass flow rate [kg/s]	0.05 – 2.0
Flow velocity [m/s]	0.5 – 18
Uniform heat flux [MW/m²]	0.5 – 7.5

In the current chapter, the description of the experimental set-up and of the experiments is given. In addition, data reduction and modeling of experiments are discussed.

3.1 Experimental set-up

3.1.1 Experimental loop

The primary circuit of the SULTAN-JHR experimental facility is shown in Figure 3.1. It consists of a loop operating with demineralized and degassed water at relatively low pressure.

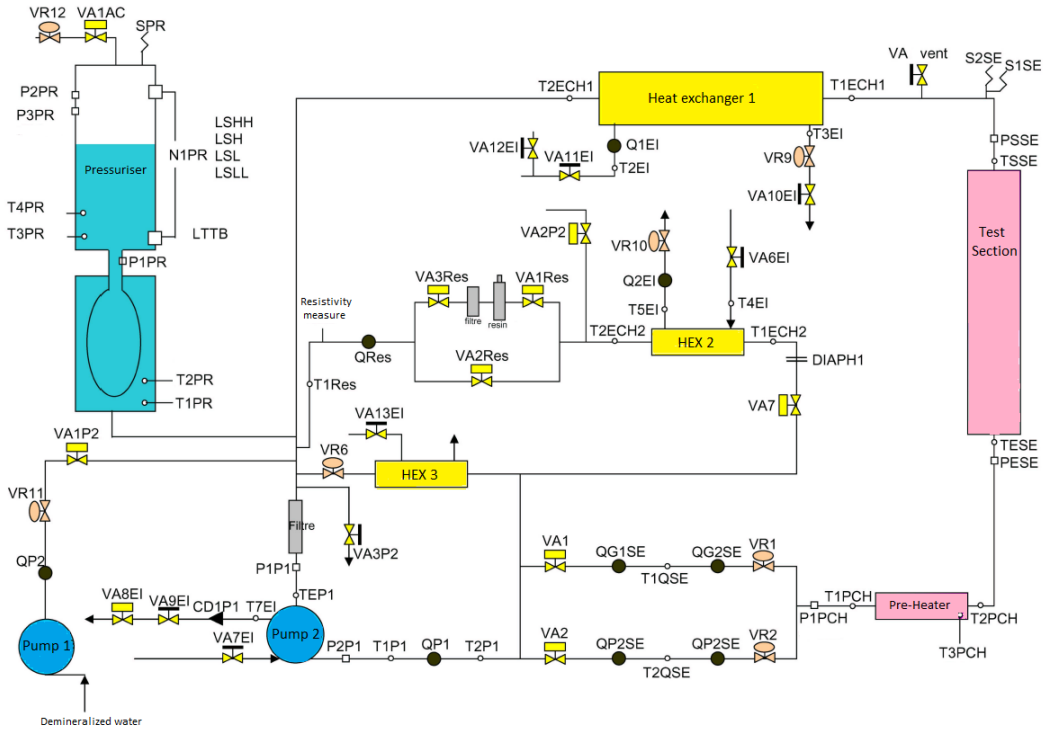


Figure 3.1: SULTAN-JHR experimental primary loop.

The primary loop consists of:

- a test section (described in Section 3.1.2).
- a 150 kW pre-heater, which allows the regulation of the water temperature before the water flow enters the test section.
- a heat exchanger - condenser (Heat exchanger 1), which extracts the power dissipated in the test section and guarantees the cooling of the loop.
- a 18.5 kW centrifugal pump (Pump 2), which guarantees the flow of water through the test section. The pump rotates at constant velocity, so that an almost constant flow rate (2 kg/s) is circulated. The regulation of the flow rate through the test section is done through a pump by-pass circuit and electric-pneumatic valves (VR1 and VR2).
- a pressurizer, which allows the regulation of the system pressure and compensates the possible dilatation and vaporisation of the fluid. A membrane is used to keep the water in the loop separated from the compressed air at the top of the pressurizer, in order to avoid the diffusion of incondensable gases in the degassed water.
- an in-line demineralization circuit, which treats continuously a small portion of the flow rate with filters and resins. The heat exchangers (HEX2 and HEX3) are used to regulate the temperature at the entrance of the resins, in order to optimize their efficiency. The main purpose is to keep the water electrical resistivity high ($> 200 \text{ k}\Omega$), removing all the impurities in the fluid. At the exit

of the demineralization circuit, the electrical resistivity of the water is measured. The electrical resistivity of the water is important because the test section is heated with a direct electrical current by Joule effect.

- two flow rate measurement lines in parallel. Each line has two venturis, which guarantee redundant and reliable measures. The measurement ranges are 0.05 - 0.4 and 0.2 - 2.0 kg/s for the small and large flow rate line, respectively. Depending on the flow rate, the correct line is operated (only one line at the time is used).

3.1.2 Test section

The test section consists of a vertical rectangular channel with water flowing upward. Three different test sections were used:

- Section 3 (SE3) with channel gap equal to 1.509 mm and uniform heat flux;
- Section 4 (SE4) with channel gap equal to 2.161 mm and uniform heat flux;
- Section 5 (SE5) with channel gap equal to 1.540 mm and non-uniform heat flux

3.1.2.1 Test sections with uniform heat flux (SE3 and SE4)

In this paragraph, the test sections with uniform heat flux (i.e. SE3 and SE4) are described. The cross-section in Figure 3.2 shows that the rectangular channel, whose

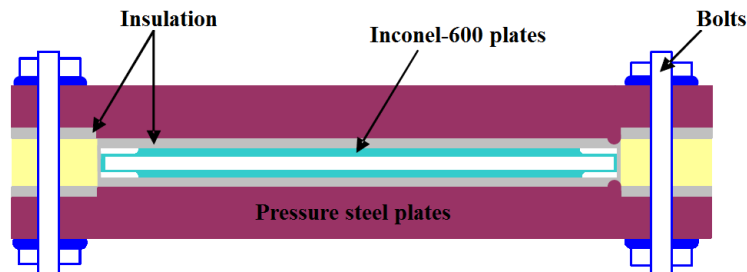


Figure 3.2: Transverse view of the SULTAN-JHR test section.

walls are made of Inconel-600, is encapsulated in an electrical insulation. The power in the test section is generated via direct electrical current heating (i.e. Joule effect) of the Inconel-600 plates. The maximum possible electrical power is equal to 600 kW. The insulation layer is obtained with mica-based *Cogetherm*[®] plates. The pressure plates consists of two 25 mm thick steel plates (steel Z38CDV5), which are kept together by bolts. The main purpose of the pressure plates is to maintain the channel gap size and geometry reasonably constant along the channel. The exterior of the test section is thermally insulated with 200 mm of rock wool to reduce heat losses. The design pressure of the test section is equal to 4 MPa. The front and side views in Figure 3.3 show the axial geometry of the test section. The test section is connected to the remaining part of the experimental loop through two brazed flanges.

The direct current is supplied at the extremities of the test section. The connection between the circular pipe of the experimental loop and the rectangular channel is

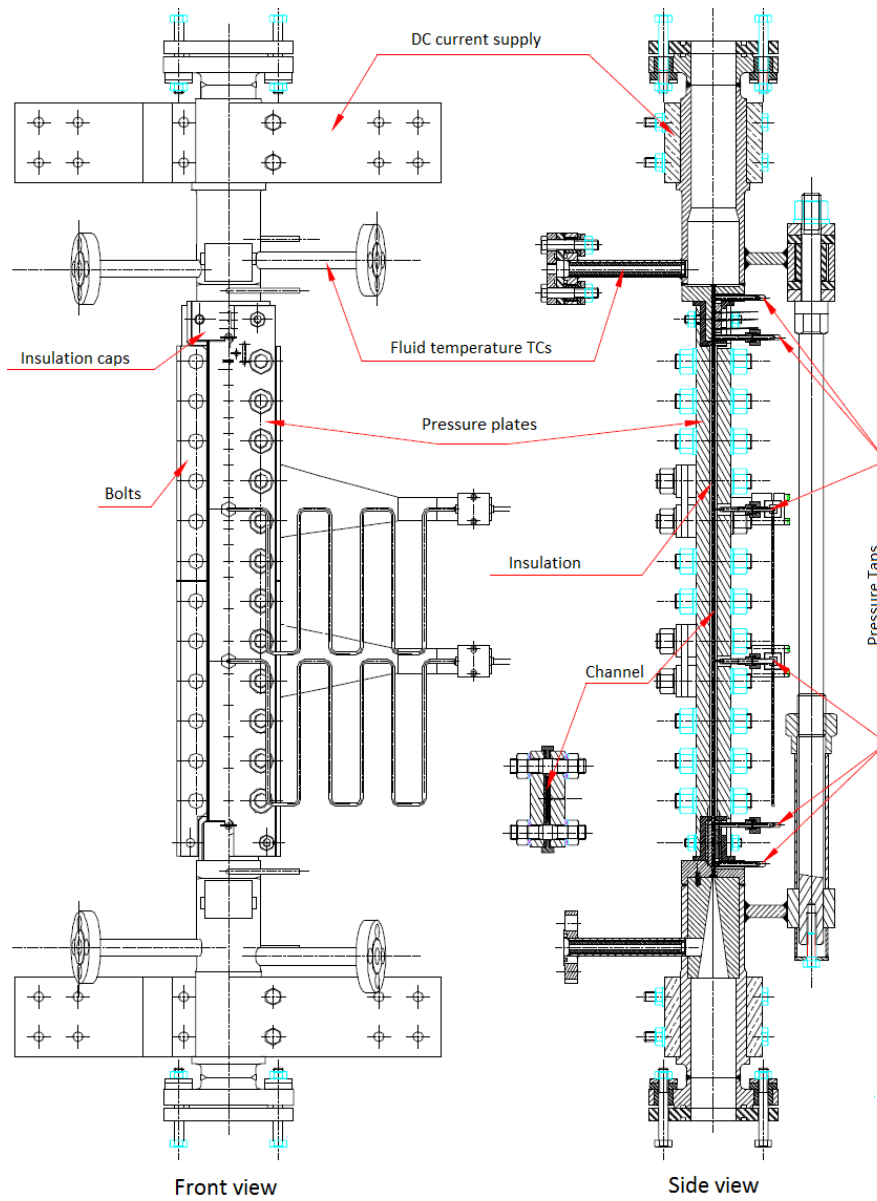


Figure 3.3: Front and side view of the SULTAN-JHR test section.

smooth at the entrance, while it is abrupt at the exit. The smooth entrance was decided in order to reduce the influence of entrance effects on the experiments.

Figure 3.4 depicts the main geometric features of the test section with the associated nomenclature used in this report.

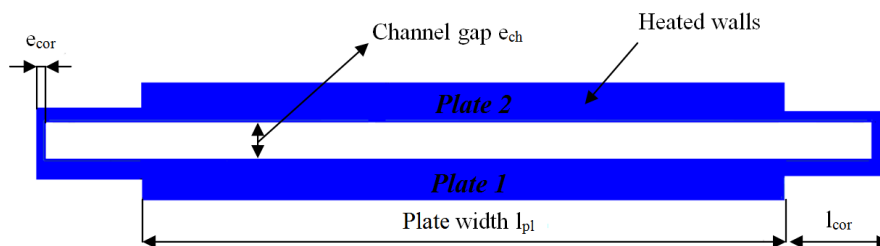


Figure 3.4: Geometry of the SULTAN-JHR rectangular channel.

The corners of the channel wall are thinner in comparison with the central part of the plates. This avoids heat concentration effects that would cause higher heat fluxes at the corners, with premature boiling and a possible local thermal crisis [22].

The dimensions of the test section with the associated nomenclature are reported in Table 3.2. The thickness of the corners was not measured, but given by the manufacturer.

Table 3.2: Test section geometry (dimensions in mm).

	SE3	SE4	SE5
Gap size (e_{ch})	1.509 ± 0.040	2.161 ± 0.050	1.540 ± 0.050
Heated height (H_{ch})	599.8 ± 0.1	599.7 ± 0.1	599.8 ± 0.1
Adiabatic zone height (H_{ad})	70.0 ± 0.1	70.0 ± 0.1	70.0 ± 0.1
Channel width without corners (l_{pl})	47.2 ± 0.1	47.15 ± 0.1	47.0 ± 0.1
Length of the corners (l_{cor})	3.15 ± 0.1	2.85 ± 0.1	3.0 ± 0.1
Thickness of the corners (e_{cor})	0.5	0.5	0.5
Averaged thickness of plate 1 (\bar{e}_{pl1})	1.0087 ± 0.006	1.003 ± 0.002	see Table 3.4
Averaged thickness of plate 2 (\bar{e}_{pl2})	0.9818 ± 0.018	1.004 ± 0.002	see Table 3.4

The gap size was proven to be approximatively constant along the channel by comparing the measurements of pressure drop performed in isothermal tests [23]. The surface roughness was evaluated to be equal to $0.4 \mu m$.

The averaged thickness of the two plates in SE3 were computed with a weighted average of the measurements reported in Table 3.3.

Table 3.3: Measured plate thickness of SE3 (dimensions in mm).

z_{pl1} [mm]	e_{pl1} [mm]	z_{pl2} [mm]	e_{pl2} [mm]
30	1.005	50	1.000
71	1.005	90	1.000
111	1.007	130	0.990
152	1.007	171	0.990
190	1.007	210	0.982
232	1.010	250	0.982
271	1.010	321	0.973
310	1.013	342	0.973
333	1.013	380	0.973
352	1.013	401	0.970
370	1.013	421	0.970
380	1.013	461	0.970
430	1.013	482	0.970
450	1.013	521	0.977
470	1.013	540	0.977
490	1.013	571	0.977
511	1.003	580	0.977
530	1.003	590	0.977
552	1.003	-	-
571	1.003	-	-

Plate 1 has a slightly bigger thickness compared to plate 2 in SE3. As regards SE4, the two plates are very similar between each other and they have thicknesses that are almost constant along the axial direction. Most of the calculations in the report were performed with the real plate thickness. The non-constant plate thickness determines a not-fully uniform heat flux along the channel, which may be important when high heat fluxes are involved.

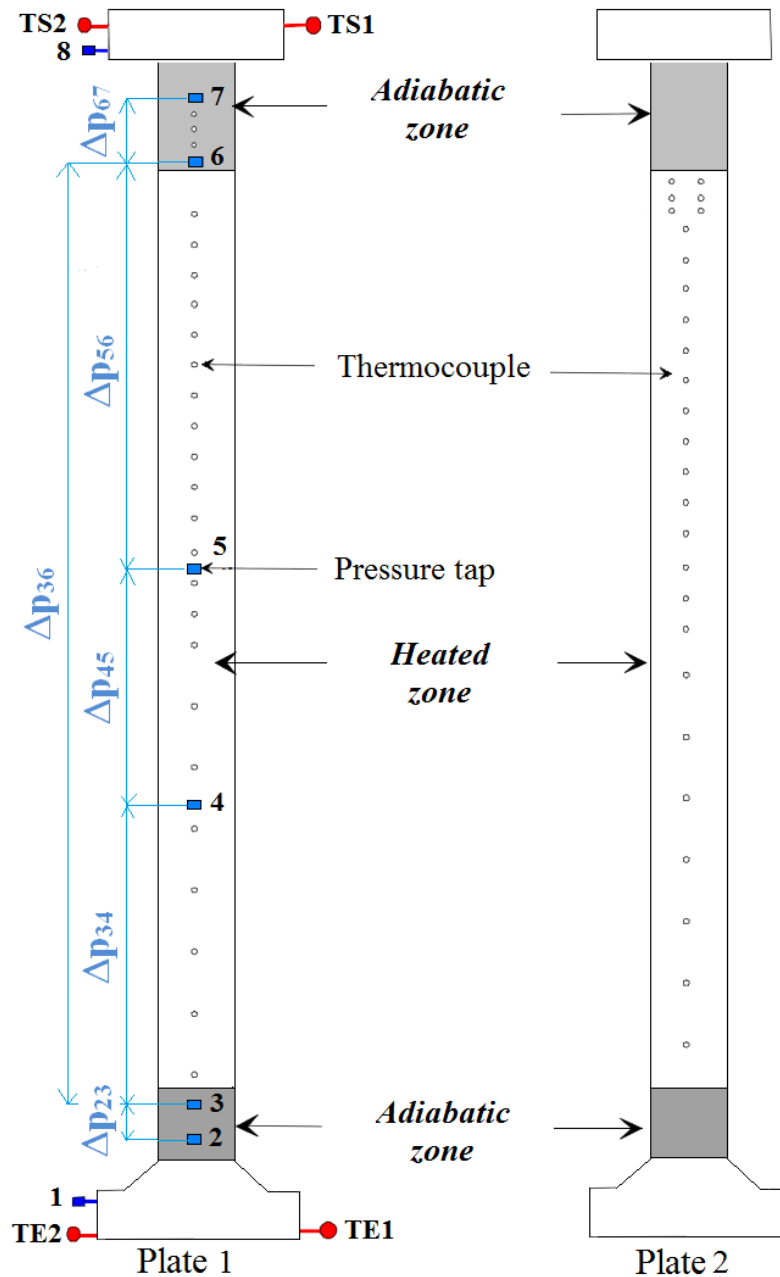


Figure 3.5: SULTAN-JHR axial geometry and instrumentation layout.

The rectangular channel can be divided in two regions, as shown in Figure 3.5:

- the *heated zone*, which corresponds to the central part of the rectangular channel, where the largest part of the electrical power is transferred to the fluid. The

heated height is approximately equal to 600 mm for both sections. Along this zone, the heat flux is approximately uniform.

- the *adiabatic zones*, which correspond to two 70 mm long low-power zones, one at the entrance and one at the exit of the rectangular channel. In these zones, the power (and consequently the heat flux) is much lower compared to the heated zone, but not completely negligible. Indeed, approximately 2 % of the total electrical power goes to the two adiabatic zones (see Section 3.1.3.5).

It is important to introduce some geometric definitions and quantities that are used in the work. The flow area A is calculated as:

$$A = l_{ch} \cdot e_{ch} \quad (3.1)$$

The wet perimeter P_w is:

$$P_w = 2(l_{ch} + e_{ch}) \quad (3.2)$$

where the channel width l_{ch} reads:

$$l_{ch} = l_{pl} + 2(l_{cor} - e_{cor}) \quad (3.3)$$

The hydraulic diameter D_h is then defined as:

$$D_h = \frac{4A}{P_w} \quad (3.4)$$

The averaged Inconel-600 cross-sectional area, where the electrical current flows and the heat is generated, can be calculated as:

$$S_{inc} = S_{inc,cor} + S_{inc,pl} \quad (3.5)$$

The averaged Inconel-600 cross section of the plates $S_{inc,pl}$ is the sum of the cross section of the two plates:

$$S_{inc,pl} = S_{inc,pl1} + S_{inc,pl2} = l_{pl} \cdot (\bar{e}_{pl1} + \bar{e}_{pl2}) \quad (3.6)$$

The evaluation of the Inconel-600 cross-sectional areas is important for determining the distribution of the electrical power and heat flux between the corners and the plates. The cross-section of the corners is then computed as:

$$S_{inc,cor} = 2 (2 l_{cor} \cdot e_{cor} + e_{ch} \cdot e_{cor}) \quad (3.7)$$

The calculation of the heat flux also requires the heated surface of the plates that is:

$$S_{heat} = l_{pl} \cdot (l_{ch} + l_{corr,voltage}) \quad (3.8)$$

where $l_{corr,voltage}$ is a correction to the channel height. The latter takes into account the fact that the electric tension is not measured exactly at the exit of the heated zone, as discussed in Section 3.1.3.5. The value of the correction is equal to 10 mm.

3.1.2.2 Test section with non-uniform heat flux (SE5)

The test section with non-uniform heat flux (SE5) is very similar to SE3, as shown in Figure 3.6 and Table 3.2.

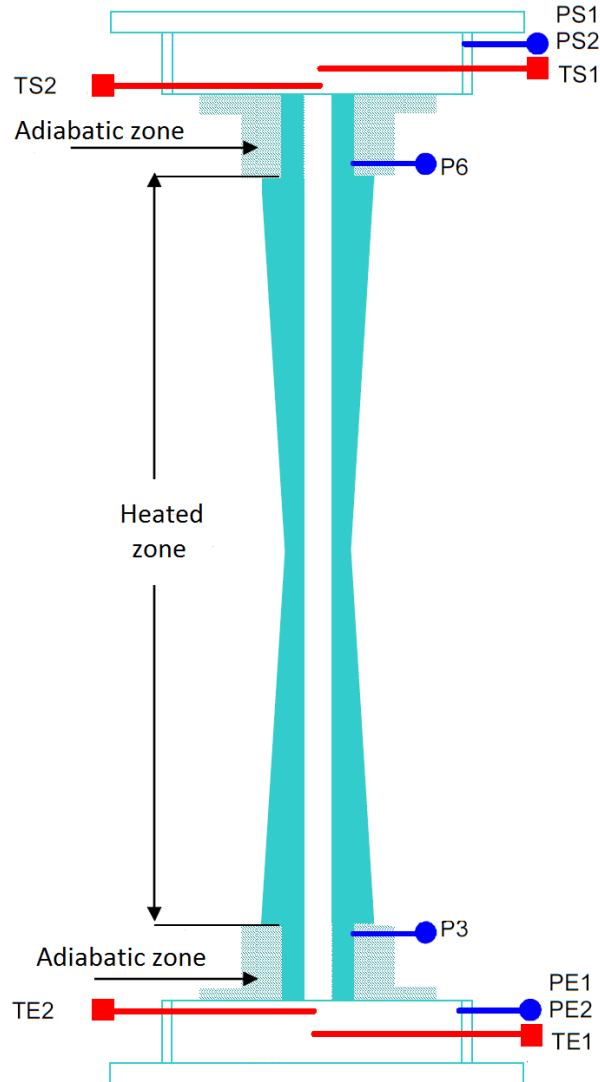


Figure 3.6: SULTAN-JHR axial geometry for Section 5 (non-uniform heat flux).

The main difference lies in the non-constant thickness of the plates, so that a non-uniform axial profile for the heat flux can be obtained. The thickness of the plates varies linearly along the channel approximatively from 1.0 mm at the center to 1.66 mm at the extremities. This configuration is meant to obtain a cosine shape of the heat flux profile that is peaked at mid-elevation of the channel. In particular, the ratio of the local heat flux and the average heat flux varies approximatively between 1.2 at the center and 0.8 at the extremities. The measured average thickness of the two plates is given in Table 3.4. Plate 1 has a slightly larger thickness compared to plate 2. A 1 mm *Cogetherm*[®] insulation layer is interposed between the plates and the pressure plates. The thickness of the Inconel plates summed to the thickness of the pressure plates is maintained almost constant along the whole channel.

Table 3.4: Measured average thickness of the plates in SE5.

z [mm]	e_{p11} [mm]	e_{p12} [mm]
50	1.566	1.554
100	1.469	1.457
150	1.383	1.368
200	1.242	1.235
250	1.143	1.123
300	1.075	1.056
350	1.180	1.157
400	1.274	1.249
450	1.352	1.328
500	1.477	1.453
550	1.595	1.584

Therefore extra-thicknesses were added to the pressure plates to counter-balance the non-constant axial profile of the plates.

3.1.3 Instrumentation

In this section a brief description of the instrumentation connected to the test section is provided. The following physical quantities are measured: wall temperature and pressure at several elevations, fluid temperature at the inlet and outlet, flow rate, electrical power.

All the raw data are automatically saved by means of a Hewlett-Packard (HP 3852S) data acquisition system, which integrates the signals from the sensors over a 20 ms time range, in order to obtain more stable measurements. The acquired measurements consist of a current signal (4 - 20 mA) coming from the sensors, which are converted into voltage signals with a 133 Ω precision resistor. The final values are obtained with an average of 100 acquisitions, in order to increase the stability and reliability of the data.

3.1.3.1 Pressure measurements

All the pressure taps (0.5 mm in diameter) are placed on plate 1, as indicated in Figure 3.5. Different locations along the channel were used:

- PE1 is in the lower plenum, at the entrance of the test section. Two sensors were used for a better precision.
- PS8 is in the upper plenum, at the exit of the test section. Two sensors were used for a better precision.
- P2 and P3 are in the adiabatic zone, at the entrance of the test section.
- P6 and P7 are in the adiabatic zone, at the exit of the test section.
- P4 and P5 are in the heated zone.

The exact position of the pressure taps can be found in Table 3.5.

Table 3.5: Location of the pressure taps (in mm, $z = 0$ refers to the lower end of the heated zone).

Pressure Tap	z SE3	z SE4	z SE5
PE1	-78	-158	-155
P2	-55	-55	-
P3	-5	-5	-5
P4	210	200	-
P5	400	390	-
P6	605	605	605
P7	655	655	-
PS8	681	727	732

Both absolute and differential pressure measurements were performed. In particular, the pressure drops were measured between the pressure taps: P2-P3; P6-P7; P3-P6; P3-P4; P4-P5; P5-P6, as shown in Figure 3.5. The differential pressures were detected with either small, medium or large range sensors, depending on the magnitude of the pressure drop, for a better precision.

3.1.3.2 Fluid temperature measurements

The water temperature is measured in the plenum at the entrance (TE1 and TE2) and at the exit (TS1 and TS2) of the test section (see Figure 3.5). Platinum probes (4 wire sensors) are used. The exact locations of the platinum probes can be found in Table 3.6.

Table 3.6: Fluid temperature thermocouples position in mm.

TC name	z SE3	z SE4	z SE5
TE1	-103	-170	-168
TE2	-92	-155	-155
TS1	702	700	700
TS2	695	690	690

3.1.3.3 Dry wall temperature measurements

The dry wall temperatures are measured with insulated K-thermocouples (1 mm in diameter) at 42 axial locations along the heated channel and 3 locations in the adiabatic zone at the exit of the test section. The first 36 thermocouples (TP1 to TP36) were placed in the central region of the channel, alternatively on the two plates. The 6 last thermocouples (TP37 - TP42) were only placed on plate 2. For this last group, two redundant measurements were taken for each location and the average between the two values was employed in the analysis. The exact position of the thermocouples is shown in Table 3.7. The values measured by TP23 in SE3 were excluded from the analysis, due to technical problems with the thermocouple.

Although the main interest is in the wet wall temperature, the thermocouples were not placed on the wet side of the heated surface. Only the 3 thermocouples in the adiabatic zone were directly brazed to the channel wall.

Table 3.7: Dry wall thermocouples position in mm.

TC name	z SE3	z SE4	N°plate	TC name	z SE3	z SE4	N°plate
TP1	30	30	1	TP24	421	421	2
TP2	50	50	2	TP25	430	430	1
TP3	71	70	1	TP26	450	450	1
TP4	90	90	2	TP27	461	461	2
TP5	111	111	1	TP28	470	470	1
TP6	130	130	2	TP29	482	482	2
TP7	152	152	1	TP30	490	490	1
TP8	171	171	2	TP31	511	511	1
TP9	190	190	1	TP32	521	521	2
TP10	210	210	2	TP33	530	530	1
TP11	232	232	1	TP34	540	540	2
TP12	250	250	2	TP35	552	552	1
TP13	271	271	1	TP36	571	571	1
TP14	310	310	1	TP37	571	571	2
TP15	321	321	2	TP38	571	571	2
TP16	333	333	1	TP39	580	580	2
TP17	342	342	2	TP40	580	580	2
TP18	352	352	1	TP41	590	590	2
TP19	370	370	1	TP42	590	590	2
TP20	380	380	1	TP43	615	615	1
TP21	380	380	2	TP44	625	625	1
TP22	401	401	2	TP45	635	635	1
TP23	-	410	1				

Conversely, all the thermocouples in the heated zone were placed behind the insulation layer so that they could be protected from the electric current.

Three different instrumentation layouts were employed during the experimental campaign, especially at the beginning when the effect of the layout on the measurements was unknown.

The first thermocouple configuration (called Instrumentation n° 1) can be seen in Figure 3.7. The figure shows all the relevant geometric parameters and the average thermal conductivity of the different materials as used in the modeling. The thermocouple is inside a 1.1 mm groove, directly in contact with the *Cogetherm*[®] insulation layer. The problem with this configuration is that the contact with the insulation layer could not be guaranteed and the eventual presence of air could lead to imprecise measurements.

The instrumentation n° 2A was introduced only for a limited set of measurements in SE3 and only on plate 2 (see Table 3.10 for more details), so that a comparison with instrumentation 1 could be possible. The main difference consisted in a glue layer which guaranteed the direct contact of the thermocouple with a thin Mica insulation layer. Here the thermocouple groove is drilled directly in the *Cogetherm*[®] insulation layer

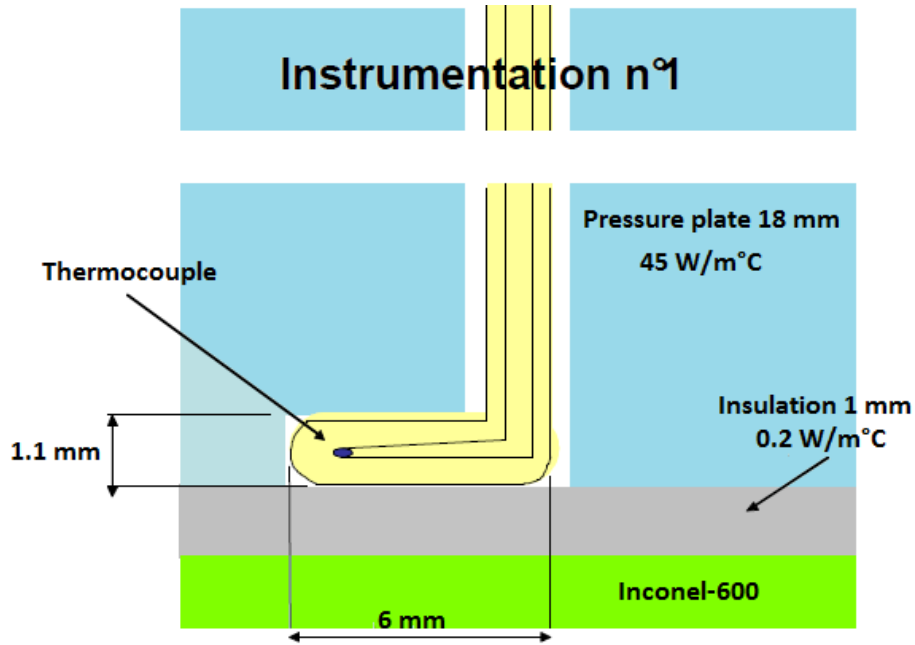


Figure 3.7: SULTAN-JHR thermocouple layout (Instrumentation n° 1).

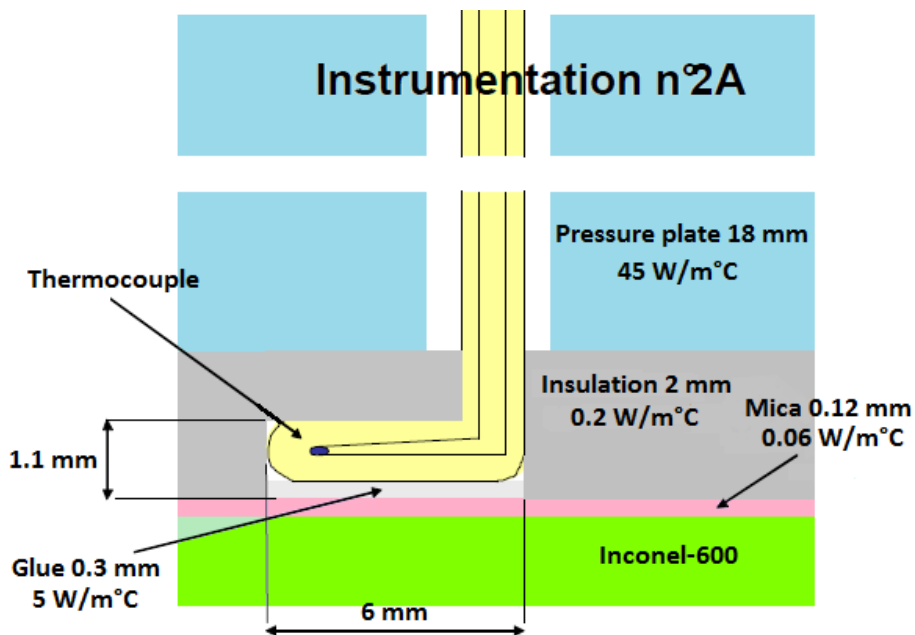


Figure 3.8: SULTAN-JHR thermocouple layout (Instrumentation n° 2A).

Finally, the instrumentation n° 2 is shown in Figure 3.9. This configuration is qualitatively similar to instrumentation n° 2A, but some differences are present. In particular, no Mica insulation layer is used (substituted with a thin *Cogetherm*[®] insulation layer) and the glue layer is thinner. This layout was employed in most of the tests (all the tests with SE4 and SE5 and 33 % of the SE3 tests), as summarized in Table 3.10.

All the layouts give similar and consistent results.

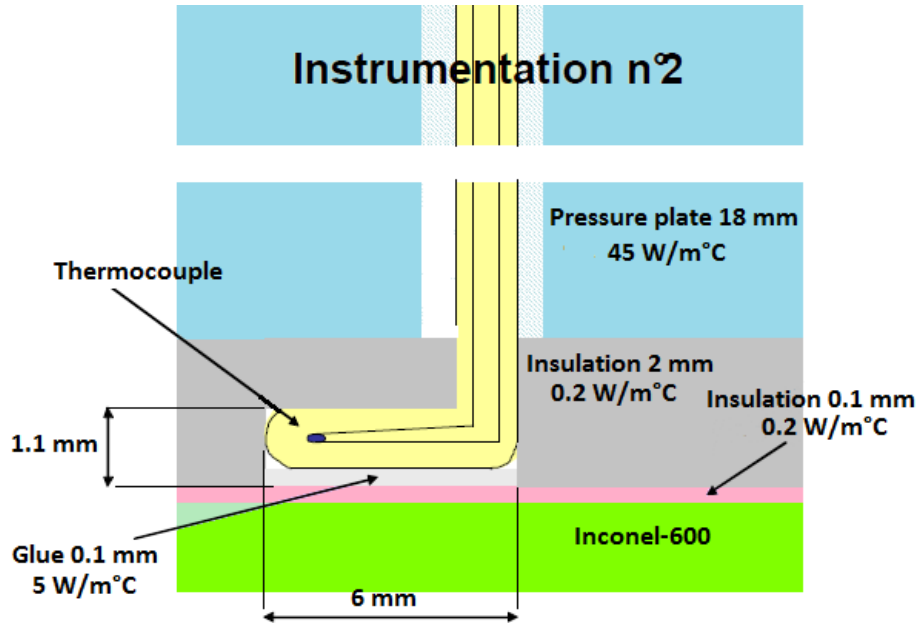


Figure 3.9: SULTAN-JHR thermocouple layout (Instrumentation n° 2).

The values measured by the thermocouples were verified with the use of a calibrated pyrometer [23] and proved to be correct. A maximum discrepancy of 2 °C was observed at high heat flux.

3.1.3.4 Critical heat flux detection

The critical heat flux is detected with 19 non-isolated thermocouples of type K placed at the end of the heated zone, as shown in Figure 3.5. These thermocouples are labeled with the acronym BO (which stands for boiling detection) at the end of the sensor name and they are numerated from TP0BO to TP18BO.

The thermocouples are located on the two plates at different axial locations:

- 6 TCs at $z = 575$ mm;
- 7 TCs at $z = 585$ mm;
- 6 TCs at $z = 595$ mm

The sensors are connected to a rapid critical heat flux detection system, which prevents the damage of the test section due to the Departure from Nucleate Boiling (DNB). The measured temperature is compared to three different thresholds:

- if $T > 300^{\circ}\text{C}$, then the electric power is automatically reduced of 8 %;
- if $T > 600^{\circ}\text{C}$, then the electric power is automatically reduced of 16 %;
- if $T > 1000^{\circ}\text{C}$, then the electric power is automatically cut off.

3.1.3.5 Voltage and electric current measurements

The power delivered to the test section is produced by Joule effect, with the passage of a DC current through the Inconel-600 plates. It is then defined as:

$$P = VI \quad (3.9)$$

where V indicates the voltage applied to the test section and I is the electric current. The current is measured at the copper bus-bar, where the DC current is supplied to the test section (see Figure 3.3). Two voltage measurements were performed:

- one at the entrance and exit of the heated zone (more precisely, at the elevations of the pressure taps P3 and P6);
- one in the plenum at the entrance and exit of the test section (more precisely, at the elevations of the pressure taps PE1 and PS1)

The voltage measurements in the plenum would be very useful for the evaluation of the power released in the adiabatic zone. Unfortunately, these data are not available for all the tests. In particular, these values are reported only for a small portion of tests in SE4. The analysis of the available data suggests that about 2 % of the total electric power was dispersed in the adiabatic regions. This value is used for the calculations in this work.

3.1.3.6 Measurement uncertainties

The uncertainties were evaluated for all the measured quantities, taking in account all the known sources of error [23]. The estimated values are listed in Table 3.8.

Table 3.8: Measurements uncertainties for the main parameters [23].

	Uncertainty		Uncertainty
Flow rate	$\pm 1\%$	Electric power	$\pm 1.4\%$
Absolute pressure	$\pm 0.8\%$	Differential pressure	$\pm 0.8\%$
Fluid temperature	$\pm 0.25^\circ\text{C}$	Dry wall temperature	$\pm 1.5^\circ\text{C}$

3.1.3.7 Instrumentation of the test section with non-uniform heat flux

The instrumentation of the test section with non-uniform heat flux (SE5) is quite similar to the one of SE3 and SE4. Nevertheless few differences can be observed. First of all, no dry wall temperature was measured. In fact, the main objective of the tests was the study of the flow redistribution and therefore of the pressure drops. The pressure drop was only measured between P3 and P6 (see Figure 3.6 and Table 3.5).

The position of the thermocouples for the fluid temperature is the same as for the other test sections (see Table 3.6). On the other hand, different locations are used for the detection of the thermal crisis, as shown in Table 3.9.

In Table 3.9, the axial position (z) is calculated from the bottom of the heated test section (i.e. $z = 0$), while the transversal position (x) is defined from the sides of the heated plates. The thermocouples for the detection of the thermal crisis are also

Table 3.9: Thermocouples for thermal crisis experiments in SE5 (z and x are the axial and transverse position in mm, respectively).

TC name	z	x	N°plate	TC name	z	x	N°plate
TP0BO	290	10	1	TP22BO	310	23.5	2
TP1BO	290	23.5	1	TP23BO	310	37	2
TP2BO	290	37	1	TP24BO	318	15	1
TP3BO	290	10	2	TP25BO	318	32	1
TP4BO	290	23.5	2	TP26BO	318	15	2
TP5BO	290	37	2	TP27BO	318	32	2
TP6BO	300	10	1	TP28BO	326	23.5	1
TP7BO	300	23.5	1	TP29BO	326	23.5	2
TP8BO	300	37	1	TP30BO	400	23.5	1
TP9BO	300	10	2	TP31BO	400	23.5	2
TP10BO	300	23.5	2	TP32BO	500	23.5	1
TP11BO	300	37	2	TP33BO	500	23.5	2
TP12BO	305	10	1	TP34BO	585	15	1
TP13BO	305	23.5	1	TP35BO	585	32	1
TP14BO	305	37	1	TP36BO	585	15	2
TP15BO	305	10	2	TP37BO	585	32	2
TP16BO	305	23.5	2	TP38BO	595	10	1
TP17BO	305	37	2	TP39BO	595	23.5	1
TP18BO	310	10	1	TP40BO	595	37	1
TP19BO	310	23.5	1	TP41BO	595	10	2
TP20BO	310	37	1	TP42BO	595	23.5	2
TP21BO	310	10	2	TP43BO	595	37	2

located at mid-elevation of the channel. In fact, the DNB may occur not only at the top of the test section, but also at mid-elevation where the heat flux is peaked. The same rapid detection system is employed to prevent burnout and failure of the test section. It should be mentioned that the thermocouples TP30BO and TP38BO were damaged during the assemblage of the test section, so they were not used.

3.2 Description of the test procedure

A summary of the tests performed during the whole SULTAN-JHR experimental campaign is shown in Table 3.10.

In the table, it can be seen that three different kinds of tests were carried out: Isothermal (ISO), Flow Redistribution (FR) and Critical Heat Flux (CHF) tests. In the isothermal tests, no power is provided to the test section. In the flow redistribution and CHF tests, the tests are performed at different power level under steady-state conditions.

A systematic nomenclature was employed to identify the tests in an unambiguously manner. Accordingly, the name of the test, from the left to the right, is such that:

- the first digit is a sequential number;
- the second and third digits are a C followed by the campaign number;

- the 4th and 5th digits are an S followed by the test section number;
- if it is a ISO test: the next digits are $P^*G^*W^*0T^*-0^{**}$ where P^* is related to the pressure value at the exit of the test section, G^* corresponds to the mass flux, $W0$ refers to zero power, T^* gives the fluid temperature at the entrance, 0^* is a sequential number;
- if it is a FR test: the next digits are $P^*W^*T^*-0^{**}$. The acronym MI indicates that the instrumentation is mixed (i.e. Instr. 1 on plate 1 and Instr. 2A on plate 2);
- if it is a CHF test: the next digits are $BOP^*W^*T^*-0^{**}$ whose only difference is the introduction of the acronym BO which indicates a boiling/thermal crisis test;

Table 3.10: Summary of the SULTAN-JHR tests.

Campaign	Section	Type	Instr.	N° tests	Test name
Campaign 1 <i>Uniform Flux</i> <i>1.5 mm gap</i>	SE3	ISO	1	52	2C1S3-P*G*W0T*-0**
		FR	1	35	3C1S3-P*W*T*-0**
		FR	1 (Plaql) 2A (Plaql2)	51	3C1S3-MIP*W*T*-0**
		FR	2	23	4C1S3-P*W*T*-0**
		CHF	2	20	5C1S3-BOP*W*T*-0**
Campaign 2 <i>Uniform Flux</i> <i>2.1 mm gap</i>	SE4	ISO	2	60	6C2S4-P*G*W0T*-0**
		FR	2	61	7C2S4-P*W*T*-0**
		CHF	2	10	7C2S4-BOP*W*T*-0**
Campaign 3 <i>Un. Flux, Gas</i> <i>2.1 mm gap</i>	SE4	FR	2	32	8C3S4-P*W*T*-0**
Campaign 4 <i>NonUn. Flux</i> <i>2.1 mm gap</i>	SE5	ISO	-	27	9C4S5-P*G*W0T*-0**
		FR	-	125	10C4S5-P*W*T*-0**
		CHF	-	NO tests	-
Campaign 5 <i>Uniform Flux</i> <i>2.1 mm gap</i>	SE4	ISO	2	10	11C5S4-P*G*W0T*-0** 14C5S4-P*G*W0T*-0**
		FR	2	72	12C5S4-P*W*T*-0** 14C5S4-P*W*T*-0**
		CHF	2	16	12C5S4-BOP*W*T*-0** 12C5S4-BO2P*W*T*-0**
Campaign 6 <i>Uniform Flux</i> <i>1.5 mm gap</i>	SE3	FR	2	11	13C6S3-P*W*T*-0**

3.2.1 Isothermal tests

The data collected in the isothermal tests are important for the validation of the models of friction and for the evaluation of the gap size along the channel. A total number of 149 tests is available.

The tests were initiated with a fixed pressure and mass flux, increasing the fluid temperature at the entrance up to the desired value. To ensure steady-state conditions in the channel, time was required for the stabilization of the temperature of the pressure steel plates (up to few hours for high fluid temperatures). When the temperature was stabilized, the pressure could be modified in order to obtain more experimental points at the same temperature level and without long waiting time for the stabilization.

3.2.2 Flow Redistribution tests

A total number of 410 flow redistribution tests were performed. In particular, 120 tests with SE3, 133 with SE4 and 125 with SE5.

The main focus of the tests was the study of the flow redistribution in narrow parallel rectangular channels, however also other models/correlations can be assessed (e.g. the single-phase forced convection heat transfer coefficient).

The pressure at the exit, the temperature at the entrance and the heat flux are fixed, while the flow-rate is decreased from a large value until the phenomenon of flow redistribution occurs. In fact, the reduction of the flow rate causes the pressure drop along the channel to decrease to a minimum and, then, to increase again. The minimum that is reached is the flow redistribution point, which determines a flow excursion (or Ledinegg) instability in the case of parallel channels. Such a condition can lead to a deterioration of the heat transfer with the possibility of extensive damage [24].

The time required for each experiment is quite long due to the slow stabilization of the pressure plate temperature and the necessity of increasing the heat flux slowly in order to avoid the damage of the test section.

3.2.3 Critical Heat Flux tests

The CHF tests were meant to study the thermal crisis limits. However, the risk of damaging the test section leads to the decision of performing a limited amount of tests (i.e. 46 tests) in favorable conditions. In particular, a pressure of 0.9 MPa and an intermediate heat flux were used.

During the tests, the pressure at the exit, the heat flux and the flow-rate are kept constant while the temperature at the entrance is increased of 0.2 °C/min until the thermal crisis is detected by the BO thermocouples. The thermal crisis is considered to start when the BO thermocouples at the end of the heated length measure a rapid increase of temperature. When this happens, the parameters at the CHF point are registered and the heat flux is decreased. Then, the procedure is repeated with a lower heat flux, so that a new CHF point is obtained.

3.2.4 Dissolved gas tests

The influence of the dissolved gases in the fluid was studied with 32 flow redistribution tests with the test section SE4. The procedure is the same as in Section 3.2.2, but the tests are performed with nitrogen dissolved into the fluid. The measure of the nitrogen concentration is performed at the entrance of the test section, taking a certain amount of water from the pressure taps.

The nitrogen measurement is not done continuously, but only at the end of the test in order to avoid any effect on the stabilization of the flow.

3.3 Experimental data reduction

As a result of the SULTAN-JHR experimental campaigns, several measurements are available and include: the inlet water temperature, the electrical power supplied to the test section, the mass flow-rate, the pressure drops and the dry wall temperatures along the channel. However these measurements need to be carefully analyzed and eventually converted to quantities, which can be more easily compared to the simulation results.

In this section, the evaluation of the wet wall temperatures from the measurements of the dry wall temperature is discussed. In addition, some considerations about the Inconel conductivity, the heat losses and the stability analysis of the tests are also presented.

3.3.1 Calculation of the wet wall temperature

In order to assess the validity of the heat transfer correlations both in single and two-phase flow, the wet wall temperature T_w needs to be obtained from the measured dry wall temperature T_{dw} . The calculation is based on the one-dimensional Fourier's law of conduction:

$$\phi = -k \frac{\partial T}{\partial x} \quad (3.10)$$

where ϕ indicates the local heat flux and k is the thermal conductivity of the wall.

For the estimation, some assumptions are made. As a result of the hypothesis of steady state 1-D conduction between the different wall layers, the axial conduction is neglected. The contact between the different wall materials is assumed to be perfect and the thermal dilatation is also neglected.

The volumetric heat source in the Inconel wall layer is modeled as a constant. This approximation is reasonable, since the electrical resistivity of the Inconel-600 slightly varies between 20 and 500 °C (see Table 3.11). Thus the heat production per unit length is not sensitive to the temperature variations along the channel.

Table 3.11: Inconel-600 electrical resistivity [25].

Temperature [°C]	20	100	200	300	400	500
Electrical resistivity [$\mu\Omega \cdot m$]	1.03	1.04	1.05	1.07	1.09	1.12

The wall materials properties are assumed to be constant in the temperature range of interest, with the exception of the Inconel-600. In particular, it was observed that the thermal conductivity of the Inconel plays an important role in the determination of the wet wall temperatures, as discussed in Section 3.3.2.

The procedure for obtaining the wet wall temperature is only explained for the instrumentation layout n° 2 of Figure 3.9. For the other instrumentation layouts, the same approach is used.

As shown in Figure 3.9, the thermocouple is placed in the insulation layer and it is separated from the Inconel heating plate by a thin mica-based insulation Cogetherm®

plate and a glue layer. Therefore three wall layers need to be considered in the calculations, namely the glue, insulation and Inconel layer. The thermal conductivities of the glue and of the insulation are assumed to be equal to a constant value, so that the temperature at the interface between the insulation and the Inconel plate can be written as:

$$T_{iw} = T_{dw} + \phi_{loss} \left(\frac{e_{co}}{k_{co}} + \frac{e_{gl}}{k_{gl}} \right) \quad (3.11)$$

where e_{co} is the thickness of the insulation, e_{gl} is the thickness of the glue, k_{co} is the thermal conductivity of the insulation and k_{gl} is the thermal conductivity of the glue. The calculation takes into account of the heat losses, which were experimentally evaluated (see Section 3.3.3).

In the Inconel plate, the volumetric local heat source χ is defined as:

$$\chi = \frac{W_{pl}}{V_{pl}} = \frac{W_{pl}}{S_{heat} e_{wl}} = \frac{\phi_{pl} + \phi_{loss}}{e_{pl}} \quad (3.12)$$

where W_{pl} is the portion of the total electrical power which goes to one Inconel plate, V_{pl} is the volume of the plate and ϕ_{wl} is the heat flux which goes to the fluid (i.e. the heat flux at the interface with the fluid, as shown in Figure 3.10).

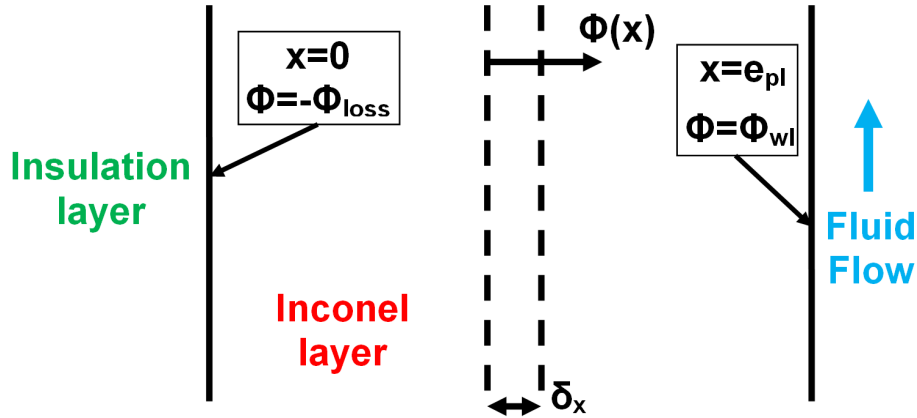


Figure 3.10: Schematic representation of the heat fluxes in the Inconel plate.

The distribution of the power between the corners and the two plates is based on the different Inconel cross sections (i.e. the available flow areas for the electric current), which implies that the electric resistivity of the Inconel is not affected by the difference in average temperature between the plates and corners. As said above, the hypothesis is reasonable since the Inconel-600 electrical resistivity does not significantly change.

Based on Figure 3.10, a heat balance for an infinitesimal slab of Inconel δx can be written. Thus, using the boundary conditions shown in the figure, an expression for the heat flux inside the plate can be obtained:

$$\phi(x) = \frac{\phi_{wl} + \phi_{loss}}{e_{pl}} x - \phi_{loss} \quad (3.13)$$

Combining Eqn. (3.13) with Eqn. (3.10), an ordinary differential equation can be

written and solved, so that the wet wall temperature reads:

$$T_w = \frac{1}{a} \left(\sqrt{b^2 - a(e_{pl}(\phi_{wl} - 2\phi_{loss}) - aT_{iw}^2 - 2bT_{iw}) - b} \right) \quad (3.14)$$

where a and b are the coefficients from the linear relationship for the Inconel conductivity $k_{inconel} = b + a \times T$ (see details in Section 3.3.2).

This approach for the evaluation of the wet wall temperatures was verified with 2D and 3D numerical simulations of the temperature fields in the walls [23]. These calculations pointed out that the axial conduction in the test section may actually be neglected.

The errors on the wet wall temperatures were derived from a propagation of the experimental uncertainties and vary between ± 1.6 and $\pm 6.3^\circ\text{C}$. The uncertainties on the geometry in Table 3.2 and on the measured quantities in Table 3.1.3.6 were taken into account. The obtained errors depend on the value of the heat flux and of the dry wall temperature, so that the highest errors are observed at high heat fluxes and wall temperatures.

3.3.2 Inconel conductivity

As seen from Eqn. (3.14), the Inconel-600 thermal conductivity may significantly affect the estimation of the wet wall temperature.

An extensive literature review and several measurements were performed at CEA in order to choose an appropriate Inconel-600 thermal conductivity. These efforts will be briefly summarized in this subsection.

The thermal conductivity was studied in a temperature interval that is of interest for the SULTAN-JHR tests, i.e. between 20 and 500 °C.

The Inconel-600, which is used in the test section, was manufactured by Special Metals Wiggin Alloys Limited. The certified chemical compositions for the material in SE3 and SE4 are reported in Table 3.12.

Table 3.12: Inconel-600 composition [mass fraction %].

	C	Si	Cu	Fe	Mn	Cr	Co	Ni	S
SE3	0.048	0.26	0.28	8.22	0.15	15.68	0.28	balance	0.004
SE4	0.07	0.44	0.27	8.36	0.20	15.02	0.54	balance	0.004
Corsan [26]	0.06	0.29	0.05	8.2	0.2	16.0	n/a	74.4	0.002
Clark [27]	0.065	0.29	0.05	8.25	0.2	16.05	0.02	balance	0.002
Blumm [28]	n/a	0.29	n/a	8.2	0.2	16.0	n/a	74.4	n/a
Filoni [29]	0.087	0.24	0.13	8.38	0.16	15.49	0.2	balance	0.001
Special Metals [25]	n/a								

Figure 3.11 shows that large discrepancies can exist between the measured Inconel-600 thermal conductivities by different laboratories.

These discrepancies could not be explained since the materials had similar chemical compositions, as listed in Table 3.12.

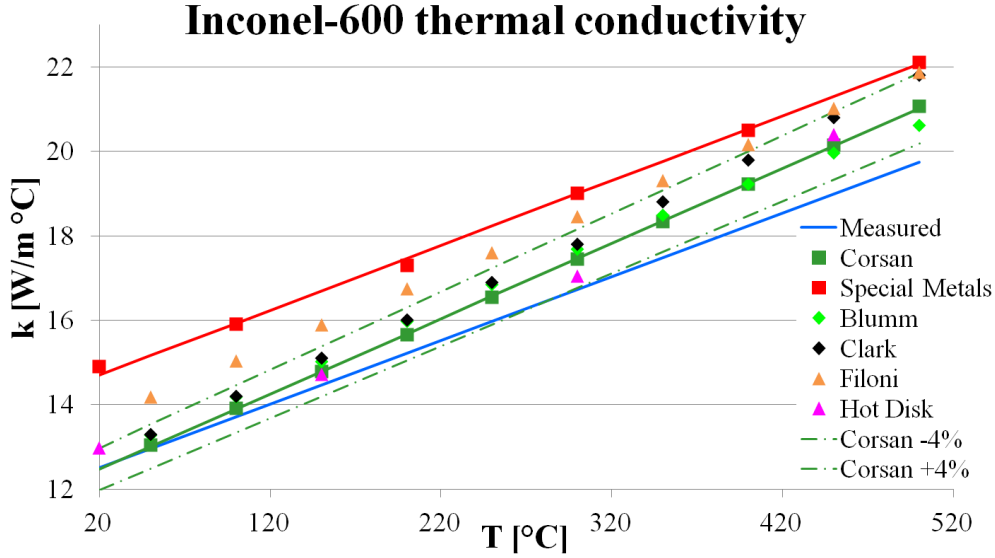


Figure 3.11: Comparison between different Inconel-600 thermal conductivity measurements.

The conductivity of the Inconel-600 used in the SULTAN-JHR facility was measured by two French independent laboratories (LMEE-CEA and LNE) and by a British laboratory (NPL). In all the three cases, a flash laser technique was applied. The linear best-fitting of the LMEE-CEA and LNE measurements, in the temperature range 25 - 470 °C, led to the following relationship [23]:

$$k_{inconel,Measured} \left[\frac{W}{m^{\circ}C} \right] = 12.206 + 0.0151 \times T [^{\circ}C] \quad (3.15)$$

An uncertainty of $\pm 5\%$ was estimated based on the standard deviation of the experimental data. This best-fitting is indicated by the blue line in Figure 3.11. It should be noticed that the Inconel used in SE3 was measured by LMEE-CEA (Saclay, France), while the one for SE4 by LNE.

In 2009, two measurements on the same SE4 Inconel (not the same sample) were performed by NPL, giving significantly different results when compared to each other. In fact, the first set of measurements gave conductivity values very similar to the one measured by Corsan, while the second were similar (or slightly smaller) to the one of Filoni. It was then decided to disregard these sets of measurements.

The manufacturer provided some thermal conductivity data [25] (indicated as Special Metals) which could be best-fitted as:

$$k_{inconel,SpecialMetals} \left[\frac{W}{m^{\circ}C} \right] = 14.44 + 0.0152 \times T [^{\circ}C] \quad (3.16)$$

No documentation was provided for these data though. It can be seen from Figure 3.11 that the values obtained from the Special Metals data significantly deviate from the other available datasets.

Several other measurements from the open literature were reviewed. One of them is the Corsan conductivity [26] and it can be modeled as:

$$k_{inconel,Corsan} \left[\frac{W}{m^{\circ}C} \right] = 12.12 + 0.0178 \times T [^{\circ}C] \quad (3.17)$$

Eqn. (3.17) is obtained with a least-square fit between 50 and 500 °C. The data are from both direct and indirect measurement methods. The direct method is such that the conductivity is evaluated from the measurements of heat flux and temperature. In the indirect case a flash laser technique is used, and the thermal conductivity is estimated from the measurement of the thermal diffusivity [27]. The total experimental uncertainty was quantified to be 4 %. In the current work, the Corsan conductivity was selected for several reasons:

- The experimental database is more extensive, since measurements with both direct and indirect methods were taken in account.
- It is consistent with the available open literature. The experimental points reported in [28], [27] and [30] fall within the 4 % uncertainty band, as shown in Figure 3.11. Only Special Metals and Filoni's data are outside the uncertainty band. In addition, no documentation is available for the Special Metals data.
- It is consistent with the set of measurements performed by the two laboratories LMEE-CEA and LNE on a sample of Inconel used in SULTAN-JHR.
- It gives slightly more conservative results than the conductivity calculated with Eqn. (3.15). In fact, the estimated wet wall temperatures are relatively higher with the Corsan conductivity.

From the analysis of the discrepancies, it is suggested that the uncertainty associated to the Corsan conductivity could be taken equal to $\pm 6\%$. In fact, the majority of the available data would be enveloped by this larger uncertainty band, including the two sets of measurements performed by NPL.

3.3.3 Heat losses

The generated heat in the Inconel is mainly transferred to the fluid, however a small portion may dissipate away from the test section. The heat losses are minimized by the presence of the 200 mm-thick thermal insulation layer. Nevertheless they were taken into account in the calculation of the wet wall temperatures.

The total power loss W_{loss} was empirically estimated with specific experiments where the test section was disconnected from the rest of the loop, filled with air and closed at the extremities. A certain electrical power was then supplied to the channel until the temperature stabilized and the injected power was suppose to be equal to the heat losses. The same experimental procedure was repeated at different power levels, so that the evolution of the heat losses as a function of the dry wall temperature T_{dw} could be reconstructed. Thus, linear best-fitting with respect to the temperature measured by the thermocouple n° 14 were obtained for both SE3 and SE4. These relationship are, respectively:

$$W_{loss,tot,SE3} = (0.3924 T_{dw} [^{\circ}C] - 4.7253) \quad (3.18)$$

$$W_{loss,tot,SE4} = (0.6646 T_{dw} [^{\circ}C] - 19.122) \quad (3.19)$$

The total experimental heat losses were found to be very small and their contribution can be assumed negligible.

These total heat losses can be further divided in two main contributions: the heat losses from the disconnected extremities and the ones along the channel.

The heat dispersed along the channel was evaluated by making use of thermocouples located at 4 different elevations, on both the internal surface of the channel and the dry side. From these measurements, it was possible to quantify the temperature differences between the two sides of the heated wall and to conclude that 45 % of the total heat losses occurred along the channel. Therefore, in the calculation of the wet wall temperature, the heat loss W_{loss} is equal to $0.45 W_{loss,tot}$ and the related heat flux is $\phi_{loss} = \frac{W_{loss}}{2S_{heat}}$.

It should be noticed that the heat losses has a negligible effect on the calculation of the wet wall temperatures ($< 0.8^\circ\text{C}$ at high heat flux [23]).

3.3.4 Analysis of the test stability

It was observed that a certain number of tests in the database had an unstable behavior in terms of pressure drop, flow rate and wall temperatures.

Each measurement is an average of 100 acquisitions recorded in time, and is characterized by a certain standard deviation σ . The values of the standard deviation are usually small ($\leq 1\%$), but they may become large because of the presence of flow instabilities.

For example, one may consider the test 12C5S4_P9W124G16_005. The pressure measured at the pressure tap P2 was equal to 1.03 MPa (average of the 100 acquisitions) with an associated measurement fluctuation of $2\sigma = 0.07$ MPa. This suggests that the level of accuracy of the experimental pressure P2 is affected by strong fluctuations in the measurement. Analogously, the pressure drop Δp_{56} was equal to 58.6 kPa with $2\sigma = 43.7$ kPa, which gives a relative error of about 75 %.

These instabilities are mainly associated with large void fractions at the channel exit ($\alpha > 0.7$ according to CATHARE calculations), which may indicate the incipience of pressure-drop oscillations in the experimental loop [31].

From this analysis, it was found that all the CHF tests and 19 flow redistribution tests in Campaign 5 (see Table 3.13) showed strong fluctuations in the measured pressure drops. In particular, the CHF tests had the strongest fluctuations as to be expected due to the high void formation during the thermal crisis.

Since these tests were not under proper steady-state conditions, they were removed from the study.

Table 3.13: Unstable tests removed from the analysis.

Unstable tests in Campaign 5		
12C5S4_P9W124G16_003	12C5S4_P9W124G16_005	12C5S4_P9W124G16_006
12C5S4_P9W124G16_010	12C5S4_P9W124G16_012	12C5S4_P9W124G16_014
12C5S4_P9W200G3_003	12C5S4_P9W200G3_004	12C5S4_P5W124G13_001
12C5S4_P5W124G13_002	12C5S4_P5W124G13_003	12C5S4_P5W200G3_003
12C5S4_P5W200G3_004	12C5S4_P5W260G45_002	12C5S4_P5W260G45_003
12C5S4_P5W260G45_004	12C5S4_P45W325G61_002	12C5S4_P45W325G8_003
12C5S4_P45W325G8_004	-	-

3.4 CATHARE model of the test section

The SULTAN-JHR test section was modeled in CATHARE as a one-dimensional channel with hydraulic diameter from Eqn. (3.4).

The 1-D channel is coupled with several heat structures (or walls), which are representative of the experimental test section's walls. Both the heated and adiabatic zones of the test section are modeled. The power generated in the adiabatic zones sums up to 2 % of the total electric power, as discussed in Section 3.1.2.1.

A schematic representation of the axial nodalization is shown in Figure 3.12.

The heated length of the channel was divided in 150 meshes of 4 mm each. The adiabatic zones at the entrance and at the exit of the channel were modeled with 21 and 17 axial nodes respectively.

This nodalization was chosen to have the center of the meshes in the same positions as the thermocouples in the experiments, so that the wall temperature predictions could be easily compared to the experimental values without interpolation between different nodes.

A constant volumetric heat production χ is modeled in the Inconel, so that a uniform heat flux is obtained at the wall-fluid interface.

The two Inconel plates are modeled separately so that different heat fluxes can be imposed. This fact is advantageous for the case of SE3, because the difference in thickness of the two plates was non-negligible (see Table 3.2). The axial variation of the thickness was however disregarded and the averaged values from Table 3.2) were used.

In order to be consistent with the experimental set-up, a further heat structure for the two corners is added. This heat structure preserves the heated perimeter of the two corners and it transfers the generated power W_{cor} to the fluid. The conduction between the heated plates and the corner heat structure is neglected. This approach was verified with dedicated numerical simulations, as discussed in [23].

In Figure 3.12, the red structures are the heated walls. The details of the radial mesh are depicted in Figure 3.13.

The geometric dimensions and thicknesses of the different layers are obtained according to the real geometric features of the test sections. The properties of the materials are provided according to the values presented in Figure 3.9 and discussed in Section 3.3.1 and 3.3.2. A slightly different configuration of the radial mesh is employed for the tests with instrumentation n° 1 and n° 2A.

An heat transfer coefficient equal to $5W/m^2 \text{ } ^\circ C$ is imposed as boundary conditions at the end of the thermal insulation layer. The external air temperature is assumed to be $25 \text{ } ^\circ C$. As predicted by CATHARE, the heat losses to the environment are small and are in agreement with the experimental evidence.

The outlet pressure p_7 , the total electric power, the inlet liquid temperature and the mass flow-rate are imposed as boundary conditions in the calculations.

The mesh independence of CATHARE results was proven. An example is shown in Figure 3.14 and 3.15.

The typical calculation time for one simulation is around 90 seconds.

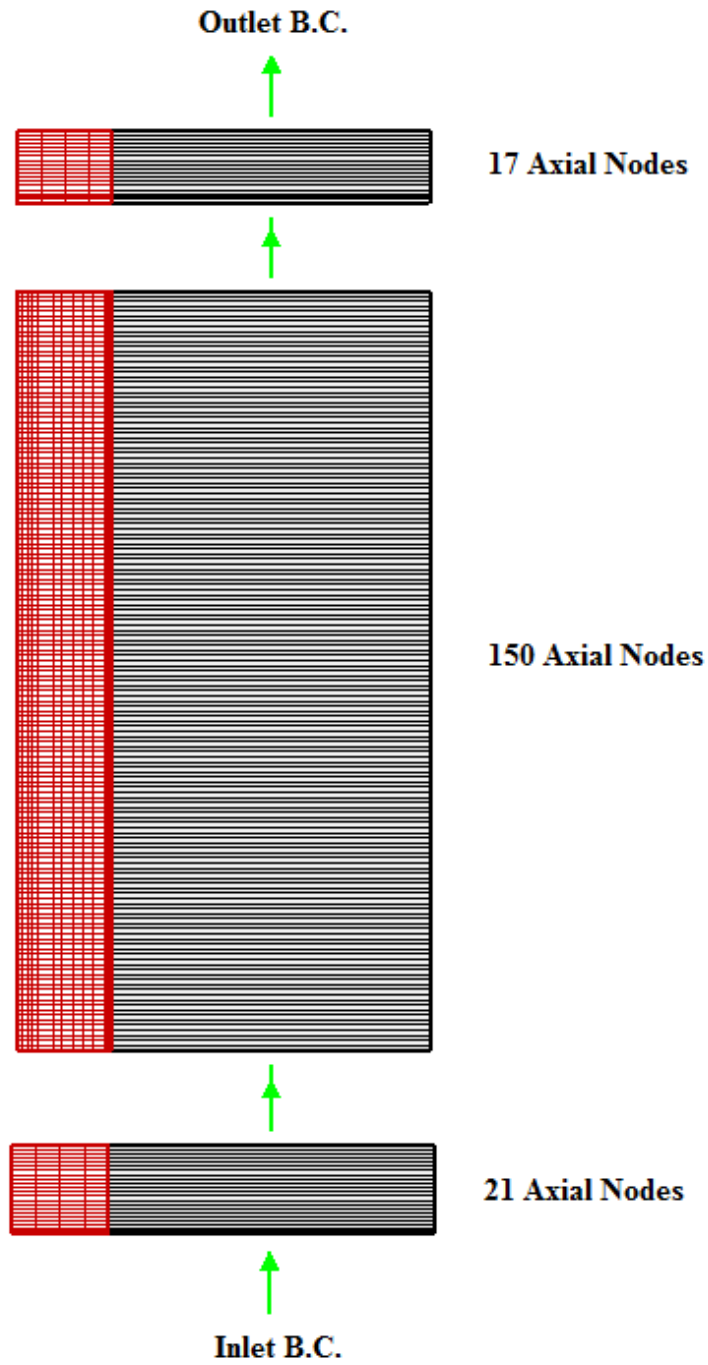


Figure 3.12: Axial nodalization in the CATHARE model.

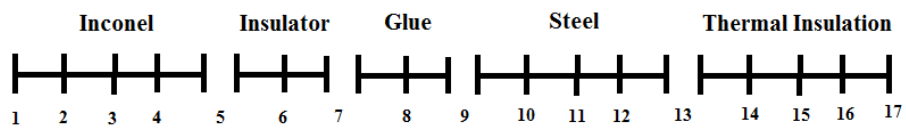


Figure 3.13: Radial nodalization of the wall in the CATHARE model (Instr. n° 2).

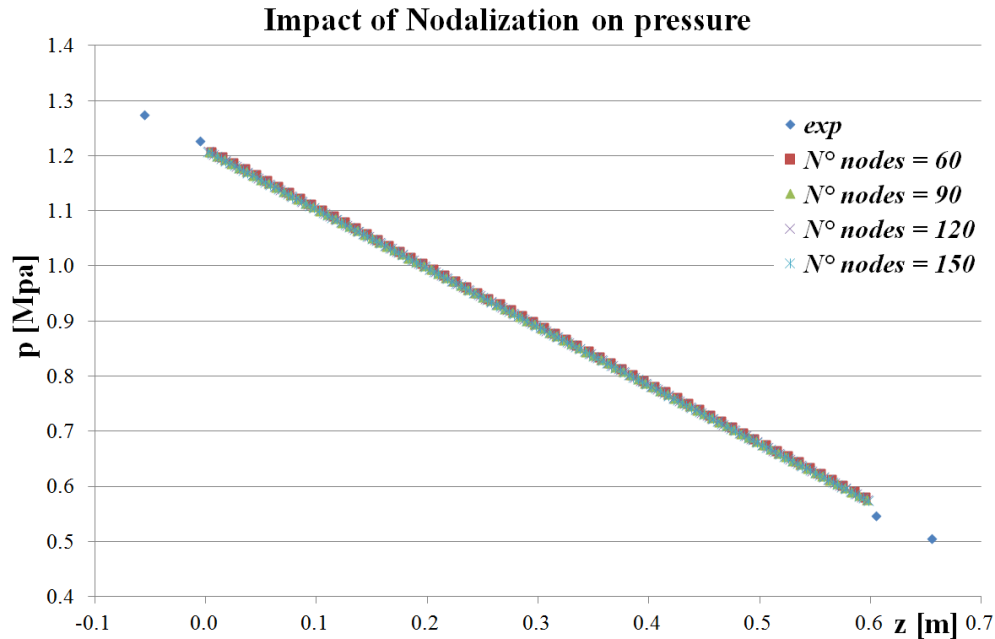


Figure 3.14: Mesh independence of CATHARE results (axial pressure profile in test 4C1S3_P5W124G25_001)

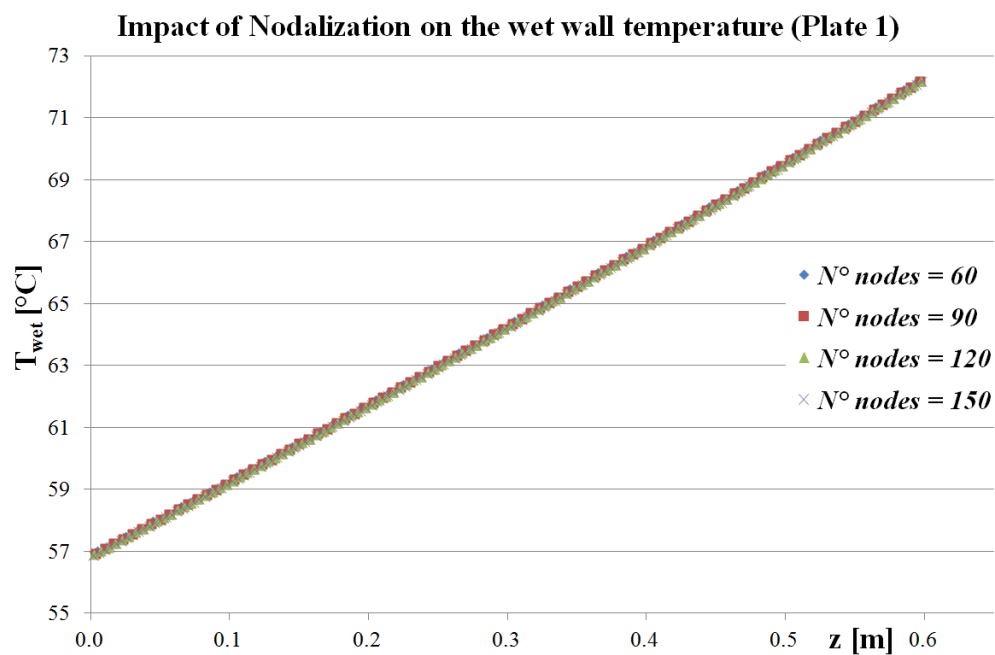


Figure 3.15: Mesh independence of CATHARE results (wet wall temperature profile in test 4C1S3_P5W124G25_001)

3.5 Simplified model for single-phase flow

For the sake of simplicity, a basic model was implemented in Matlab for the analysis of the experimental data in single-phase flow.

Analogously to the CATHARE model, the test section was modeled with a 1D channel of hydraulic diameter D_h . Only the liquid phase was modeled and the wall

heat structures were substituted with an uniform heat flux boundary condition. The mesh used is the same described in the previous section (see Figure 3.12).

The estimation of the liquid bulk temperature is based on a heat balance for the fluid, which gives the fluid enthalpy i as a function of the axial distance z :

$$i(z) = i_{z=0} + \frac{\phi P_w}{\dot{m}} z \quad (3.20)$$

The pressure drops are calculated according to the following expression:

$$\Delta p = \Delta p_{grav} + \Delta p_{fric} + \Delta p_{acc} \quad (3.21)$$

The acceleration term was neglected since it has a minor effect in single-phase flow (in the SULTAN-JHR tests, $\Delta p_{acc} < 10^{-4} \cdot \Delta p$). The gravity term reads:

$$\Delta p_{grav} = \rho_l g \Delta z \quad (3.22)$$

and the friction term is:

$$\Delta p_{fric} = 4f \frac{\Delta z}{D_h} \frac{G^2}{2\rho_l} \quad (3.23)$$

The friction factor f is modeled as:

$$f = F_{cor} \times f_{iso} \quad (3.24)$$

In the equation above, the friction factor f_{iso} is optimized over the isothermal SULTAN-JHR experiments:

$$f_{iso} = \frac{0.0505}{Re^{0.196}} \quad (3.25)$$

The corrective factor F_{cor} is for the diabatic tests (see Section 4.2.4) and it is given by:

$$F_{cor} = 1 - \frac{P_h}{P_w} \frac{0.0085(T_w - T_b)}{1 + 2 \left[\frac{T_w + T_b}{200} \right]^{1.5}} \quad (3.26)$$

where P_h and P_w indicates the heated and the wet perimeter respectively.

In these calculations, the physical properties of the fluid are evaluated at the bulk temperature and pressure of the fluid. The inlet pressure p_2 , the total electric power, the inlet liquid temperature and the mass flow-rate are imposed as boundary conditions in the calculations.

It should be noticed that the differences in results between the CATHARE and the simplified model are negligible for single-phase flows when the same friction and heat transfer correlations are used.

This Matlab model was used to evaluate correlations for single-phase friction and for heat transfer. Thus, the experimental friction and heat transfer coefficients are needed for the purpose of comparison.

The experimental friction factor was derived from the isothermal tests as:

$$f_{exp} = \frac{2\rho_l D_h (\Delta p_{exp} - \rho_l g \Delta z)}{G^2 \Delta z} \quad (3.27)$$

The formula evaluates Darcy's friction factor, which is equal to four times the Fanning's one (i.e. $f_{exp} = 4f$).

For the assessment of the single-phase heat transfer correlations, the experimental Nusselt number was calculated:

$$Nu_{exp} = \frac{h_{exp} D_h}{k_l} \quad (3.28)$$

The experimental heat transfer coefficient is defined as the ratio between the imposed local heat flux ϕ and the difference between the experimental wet wall and calculated liquid bulk temperature:

$$h_{exp} = \frac{\phi}{(T_w - T_l)} \quad (3.29)$$

Chapter 4

Single-phase modeling

In this chapter, the validity of the single-phase friction and heat transfer correlations in narrow rectangular channels is assessed. The available correlations from the literature are compared to the experimental SULTAN-JHR data and new correlations are eventually developed.

Different flow regimes are analyzed, namely the laminar, transition and turbulent flow regimes under forced convection conditions.

The laminar regime occurs at low velocities of the fluid, when it flows in parallel layers with no turbulent eddies and lateral mixing. This regime is rarely encountered during the nominal operation of reactors, but it may be important during accidental scenarios. A flow can evolve from laminar to turbulent when a critical Reynolds number Re_{cr} is exceeded. The process is gradual and a transition zone is observed between the fully laminar and the fully turbulent flow regimes. It is therefore possible to define a lower and upper limit of the transition zone with respect to the Reynolds number.

...

The correlations both in laminar and the laminar-turbulent transition flows, and the transition criterion are evaluated. This work is based on previous findings reported in the literature and on suitable experiments available in the SULTAN-JHR database, at low Reynolds numbers.

The chapter is divided in four main sections. The first part reviews CATHARE's code structure for the transition between laminar and turbulent flows. The second part analyzes the friction factors both in laminar, transition and turbulent flows together with the laminar-turbulent transition criterion. The focus is then shifted to the heat transfer modeling. The heat transfer correlations for laminar and transition forced convection flows is reviewed in the third part. The last part addresses the modeling of the turbulent heat transfer coefficient, providing an extension of the work published in Paper I (see full paper at the end of the thesis). Finally conclusions are drawn and a set of correlations for the improvement of the modeling in CATHARE is suggested.

4.1 Improvement of CATHARE code structure

The convection heat transfer coefficient in CATHARE is computed as the maximum of four different correlations, as shown in Eqn. (2.36). The four correlations calculate the heat transfer coefficient for the laminar and turbulent flow regime in natural and

forced convection. Therefore, the transition from the laminar to the turbulent flow regime is modeled without a transition zone.

In the literature, the laminar-turbulent transition is usually defined for a range of the Reynolds number (in the case of pipe flow: 2500-4000) according to the experimental evidence. Thus, CATHARE approach may be not conservative, as shown in Figure 4.1.

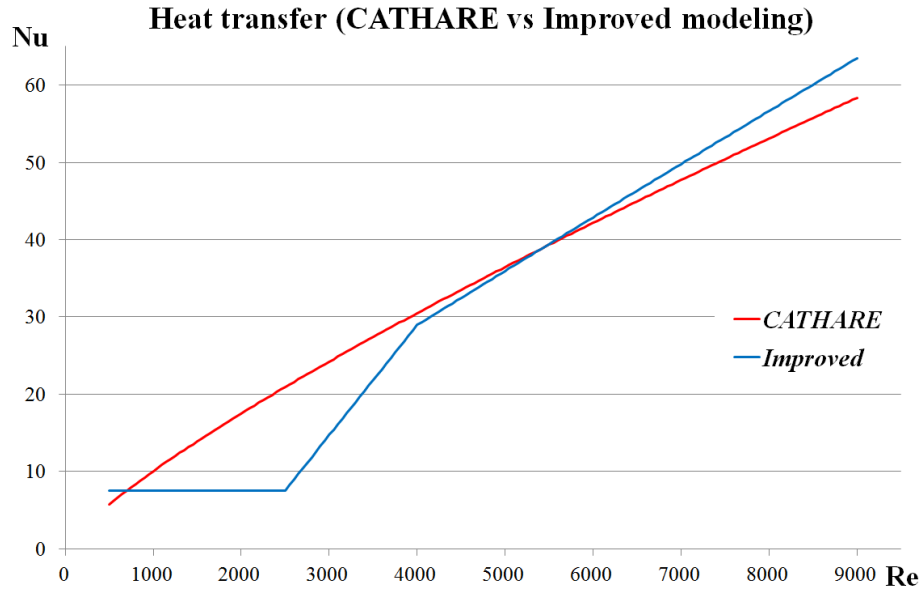


Figure 4.1: Comparison of the heat transfer coefficient predicted by CATHARE and the improved modeling suggested in Section 4.5 ($Pr = 4$, SE4)

The calculations in the figure suggests that CATHARE may over-predict the heat transfer coefficient when the flow is either in the laminar or transition region. In particular, CATHARE is not able to correctly predict the beginning of the laminar flow regime, leading to the use of the correlations for turbulent flows over almost all the range of values of the Reynolds number.

The two curves were obtained using a Prandtl number equal to 4 (i.e. the typical value of the SULTAN-JHR tests). The improved modeling that includes the transition between the laminar and turbulent region (named *Improved* in the figure) is derived from the literature and from the analysis of proper SULTAN-JHR experimental data, as discussed in the following sections. In particular, the curve is obtained with a laminar-turbulent transition for Reynolds number between 2500 and 4000. The correlations suggested for SE4 in Section 4.5 are used.

It should be noticed that other system codes (e.g. TRACE [6]) uses the same maximum approach. However, TRACE uses the Gnielinski correlation (see Eqn. (4.20)) for the turbulent heat transfer coefficient. This correlation is applicable also to the transition region, so that the over-prediction observed with the Dittus-Boelter correlation is avoided [6].

As regards the wall friction factor in CATHARE, the maximum between the laminar and turbulent isothermal friction factor is taken (see Eqn. (2.24)). Again, the validity of the criterion may be questionable, as shown in Figure 4.2.

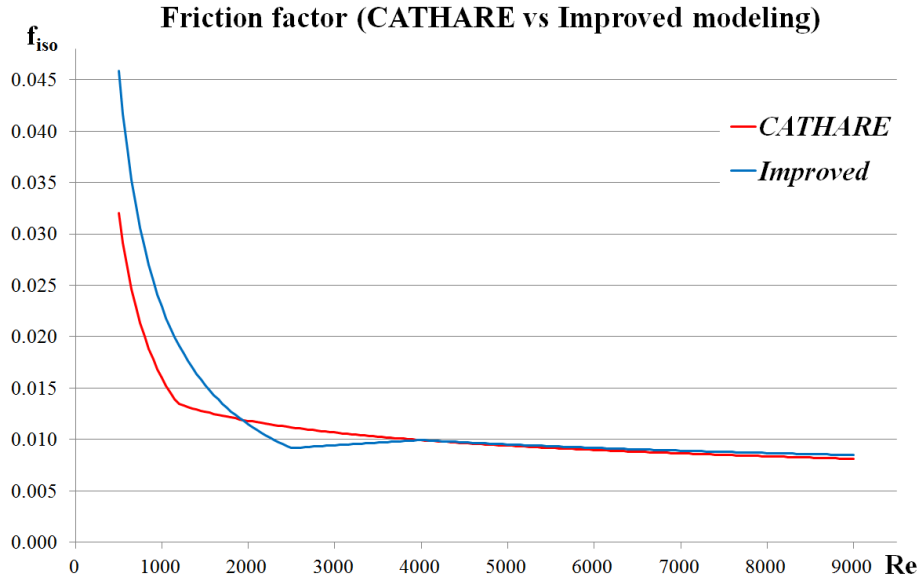


Figure 4.2: Comparison of the Fanning friction factor predicted by CATHARE and the improved modeling suggested in Section 4.5

The code structure in CATHARE has been therefore improved in order to have a more consistent modeling of the laminar-turbulent transition phenomenon. In particular, the laminar-turbulent transition in a fixed range of the Reynolds number has been implemented both for the friction and the forced convection heat transfer, while the original CATHARE approach is retained for the choice between the natural and forced convection correlations. The implemented correlations and transition Reynolds range are discussed in the following sections.

4.2 Friction and laminar-turbulent transition modeling

In this section, the laminar, transition and turbulent friction correlations are discussed and compared to the SULTAN-JHR experimental data. The laminar-turbulent transition are also analyzed.

4.2.1 The friction factor in laminar flow

The laminar Fanning friction factor in CATHARE is modeled with the expression valid for circular ducts:

$$f_l = \frac{16}{Re} \quad (4.1)$$

where the fluid properties are evaluated at the liquid bulk temperature and the Reynolds number is calculated with the hydraulic diameter of the rectangular test section. Nevertheless, a different formulation of the laminar friction factor in rectangular channels is usually suggested in the literature.

This is the Shah-London correlation [32]:

$$f_l = \frac{24}{Re} f(AR) = \frac{24}{Re} (1 - 1.3553AR + 1.9467AR^2 - 1.7012AR^3 + 0.9564AR^4 - 0.2537AR^5) \quad (4.2)$$

The Shah-London correlation modifies the friction factor computed in the case of two infinite vertical plates with a correction factor $f(AR)$ that depends on the aspect ratio AR of the rectangular channel. The latter is defined as:

$$AR = \frac{e_{ch}}{l_{ch}} \quad (4.3)$$

The correction factor $f(AR)$ (and consequently the friction factor) decreases with an increase in aspect ratio (i.e. the more squared the channel becomes), as shown in Figure 4.3. In addition, one can see that $f(AR)$ is equal to unity in the case of infinite plates ($AR = 0$).

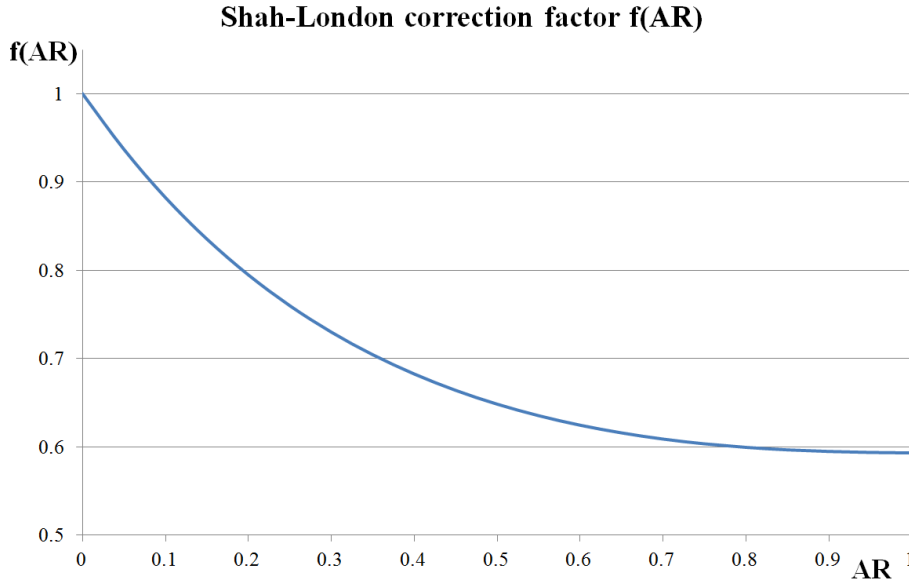


Figure 4.3: Correction factor $f(AR)$ in the Shah-London correlation.

This correlation was tested with experiments in micro-channels [33] and in narrow rectangular channels similar to the SULTAN-JHR test sections [34] [35], and it was proved reliable.

Wang et al. [34] analyzed the data measured in a vertical narrow rectangular channel of 2 x 40 x 1100 mm at the pressure of 0.8 MPa (i.e. conditions very similar to the ones in SULTAN-JHR) and demonstrated that Eqn. (4.2) gives good predictions for isothermal tests.

Ma et al. [35] derived an empirical formula based on their experimental data:

$$f_l = \frac{22.33}{Re} \quad (4.4)$$

This formula was obtained for a rectangular channel (2 x 40 x 1092 mm) at atmospheric pressure, with an aspect ratio equal to 0.05. If this value of aspect ratio is introduced

in the Shah-London correlation, then one can achieve the relationship $f_l = \frac{22.49}{Re}$, which is very close to Eqn. (4.4).

The Shah and London was also verified theoretically on the whole aspect ratio range in [36].

Therefore the most appropriate correlation for the laminar friction factor seems to be the Shah-London correlation. This is also confirmed by the comparison with the SULTAN-JHR experimental points in laminar conditions (even though they are few), as shown in Figure 4.4.

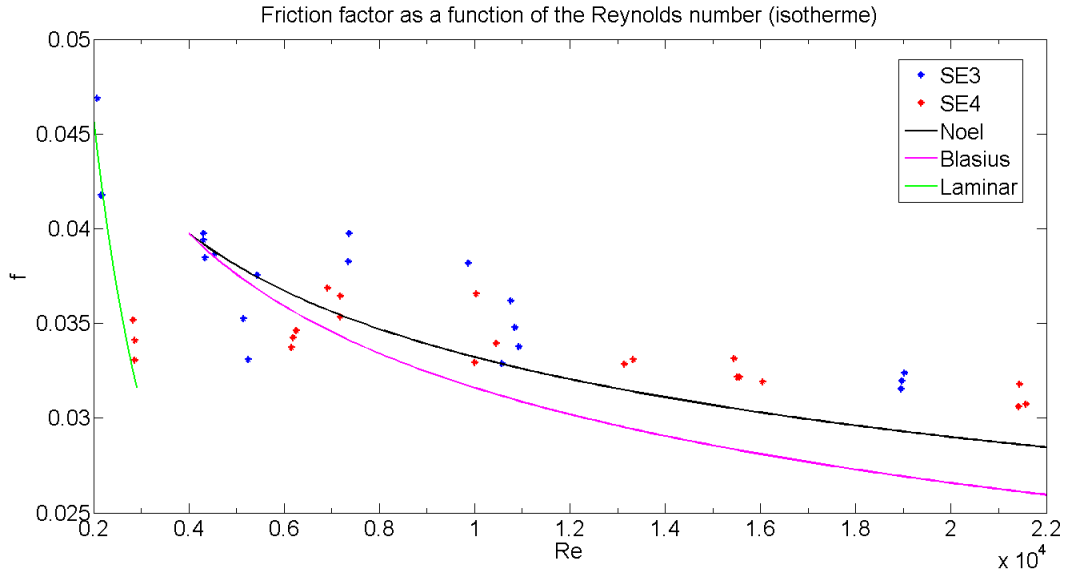


Figure 4.4: Comparison of the experimental and calculated Darcy friction factors at low Reynolds number (isothermal tests).

In this figure, the experimental Darcy friction factor (equal to four times the Fanning friction factor) in the isothermal tests of SE3 and SE4 at relatively low values of the Reynolds number is compared with some selected correlations. The experimental friction factor is obtained from the analysis of the measured pressure drops in the central part of the channel (i.e. Δp_{45}) according to Eqn. (3.27). All the other measured pressure drops are excluded from the analysis in order to rule out the potential entrance effects.

The *Laminar* friction coefficient in the figure is computed with the Shah and London equation with an intermediate aspect ratio between SE3 and SE4 ($AR = 0.0352$). Thus, Eqn. (4.2) becomes:

$$f_{iso,lam} = \frac{22.91}{Re} \quad (4.5)$$

The use of an unique expression of the laminar friction coefficient has the advantage of simplifying the modeling and the implementation in CATHARE.

Since Eqn. (4.5) provides relatively accurate results (see the green line in Figure 4.4), it is then suggested for the JHR modeling when laminar flow comes into play.

4.2.2 The laminar-turbulent transition

The laminar-turbulent transition is a gradual process that arises when a critical Reynolds number Re_{cr} is exceeded. The laminar-turbulent transition region has also an upper Reynolds number beyond which the flow becomes purely turbulent.

The entrance configuration of the channel (i.e. smooth or abrupt inlet), the pipe roughness and possible external disturbances play an important role in the determination of the laminar-turbulent transition [16]. Therefore no limits for the transition region can be defined a priori for all the geometric and flow configurations. Nevertheless there is a lower limit below which a laminar flow remains laminar, no matter how large are the disturbances at the inlet of the channel. For circular ducts, this lower limit is $Re_{cr} = 2300$.

In rectangular ducts, the lower limit was theoretically evaluated in [36] as:

$$Re_{trans} = 2691(1 - 1.6805AR + 1.6956AR^2 - 0.5639AR^3 - 0.0452AR^4) \quad (4.6)$$

This correlation gives good results when compared to experiments with different aspect ratios and hydraulic diameters [36]. Therefore, considering section SE4 of the SULTAN-JHR experiments, the flow will remain laminar, at least, up to $Re = 2510$. However, higher values for the departure from the laminar regime are possible, as reported in Table 4.1 [16].

Table 4.1: Laminar-turbulent transition for smooth rectangular channels [16].

Smooth Entrance		Abrupt Entrance	
AR	Re_{cr}	AR	Re_{cr}
0	3400	0	3100
0.1	4400	0.1	2920
0.2	7000	0.2	2500
0.33	6000	0.26	2400
1.0	4400	0.34	2360
		1.0	2200

The table summarizes the results from experiments with different aspect ratio, where $AR = 0$ indicates a flat duct and $AR = 1$ a square duct. The differences between smooth and abrupt entrance point out the importance of the inlet configuration. In particular, the critical Reynolds is increased when a smooth entrance is used because less disturbances are introduced.

In order to determine the transition regime boundaries, the isothermal friction factor and the Nusselt number are usually analyzed as a function of the Reynolds number, as shown schematically in Figure 4.1 and 4.2.

The main results from the literature about laminar-turbulent transition in narrow channels are summarized below.

Ma et al. [35] observed the occurrence of the transition between Reynolds number equal to 2500 and 4000. Isothermal experiments in a rectangular channel with aspect ratio equal to 0.05 and gap size of 2 mm were analyzed.

From the experimental data of Liang et al. [37], it seems possible to identify a transition Reynolds range between 2900 and 4000. The experimental facility consisted of a rectangular test section with aspect ratio equal to 0.036 and gap size 1.8 mm.

However, it must be emphasized that the transition region was not investigated in the work.

Wang et al. [34] determined the transition Reynolds range based on the isothermal tests approximatively equal to 2700-3800.

Sudo et al. [38] performed experiments with a rectangular channel of 2.25 x 50 x 750 mm with either one or two plates heated. Both the downward and the upward flows were studied in a Reynolds range of 100 - 50000. A transition range of 2000-4000 was approximatively observed.

The results under isothermal conditions in narrow rectangular channels are quite consistent with each other despite the different experimental setup and the intrinsic difficulty in defining clear limits for the transition. Thus, it may be concluded that the transition occurs approximatively between a Reynolds number of 2500 and 4000 in isothermal conditions. This Reynolds range is consistent with the SULTAN-JHR experimental data, as shown in Figure 4.4.

The evaluation of the transition region is more difficult for the heated tests because a delay in the departure from laminar flow is experienced. In this case the transition depends on the Nusselt number, the Reynolds number, and the Prandtl number [39]. In particular, the lower and upper limits of the region increase with the decrease of the Prandtl number.

The phenomenon is explained by the empirical observation that a flow becomes more stable if the liquid velocity profile flatten more [40]. In fact a higher Prandtl number in laminar flow implies a flatter velocity profile that is steeper in the near-wall region. This is due to the fact that the heat flux changes the fluid viscosity at the wall.

Similar conclusions were drawn by Silin et al. [41]. This study proved that an high heat flux reduces the fluid viscosity at the wall, with a stabilizing effect on the flow. The experiments were performed in a heated test section of 2.7 x 60 x 620 mm, at 0.16 MPa. The departure from the laminar flow regime was observed at increasing Reynolds values (from 2900 to 3700) by increasing the imposed heat flux.

It may be thus concluded that a more flattened velocity profile in the heated tests causes a shift of the transition flow regime boundaries towards higher Reynolds number, as further discussed in Section 4.3.2.

4.2.3 The friction factor in transition flow

The modeling of the transition flow regime is usually avoided due to the high uncertainties. Nevertheless this flow regime may be important in accidental reactor transients with small coolant mass flow rates.

No reliable and well-established formula for the friction factor in transition flow for rectangular channels is available [16]. Kakaç suggested the use of the correlations for circular ducts by making use of a proper hydraulic diameter [16]. This approach seems reasonable, even though these correlations are not-fully validated.

A linear interpolation between the laminar and turbulent correlations in the Reynolds range 2500-4000 is therefore proposed for the modeling of the transition friction factor in CATHARE:

$$f_{iso,trans} = f_{iso,lam,2500} + [f_{iso,turb,4000} - f_{iso,lam,2500}] \frac{Re - 2500}{4000 - 2500} \quad (4.7)$$

This expression was chosen because it is simple to implement in CATHARE and it guarantees the continuity of the friction factor. Moreover, no experimental data are available in SULTAN-JHR to support any more sophisticated modeling.

The analysis of the measured pressure drops in the non-isothermal SULTAN-JHR tests revealed that no data are available in the laminar and transition flow regime. The minimum value of the Reynolds number in the central part of the channel is equal to 7000, which is already in the turbulent region. Therefore no comparison was possible with the non-isothermal tests.

4.2.4 The friction factor in turbulent flow

The turbulent friction factor plays an important role in the determination of the pressure drops both in nominal and accidental conditions of nuclear reactors. The standard correlation in CATHARE is the Blasius correlation [42]:

$$f_{iso,turb} = \frac{0.079}{Re^{0.25}} \quad (4.8)$$

It was developed for smooth circular pipes and it is applicable in the range $4000 \leq Re \leq 10^5$.

Siman-Tov et al. [43] suggested the use of a modified Filonenko correlation for narrow rectangular channels:

$$f_{iso,turb} = \frac{1}{4} \frac{\left[1.0875 - 0.1125 \left(\frac{e_{ch}}{l_{ch}} \right) \right]}{(1.82 \log_{10} Re - 1.64)^2} \quad (4.9)$$

It is valid in the range $10000 \leq Re \leq 230000$. Filonenko correlation was initially developed for circular pipes, but it was extended to rectangular channels by introducing a correction factor based on the aspect ratio [43]. The friction factor predicted with Eqn. (4.9) is equal to the Blasius one when the aspect ratio is equal to unity, and it increases with the decrease of the aspect ratio. It was therefore observed that the friction factor in narrow rectangular channels may be under-estimated by the Blasius correlation, as shown in Figure 4.5.

In this figure, the curve calculated with the Filonenko correlation refers to an aspect ratio equal to 0.0352, that is between the values for SE3 and SE4. This intermediate value was selected as representative of both the test sections since the differences in friction prediction are negligible.

The isothermal SULTAN-JHR tests both in SE3 and SE4 have been already analyzed at CEA-Grenoble and the following correlation was obtained by B. Noel:

$$f_{iso,turb} = \frac{0.0505}{Re^{0.196}} \quad (4.10)$$

This correlation was developed with a best-fitting of the SE3 tests, minimizing the discrepancies on the whole turbulent Reynolds range ($4000 \leq Re \leq 300000$). Then, it was also verified with the experimental data of SE, in the range $4000 \leq Re \leq 440000$. Small discrepancies were observed between the experimental data in SE3 and SE4, so that the correlation developed for SE3 was adopted for the JHR modeling.

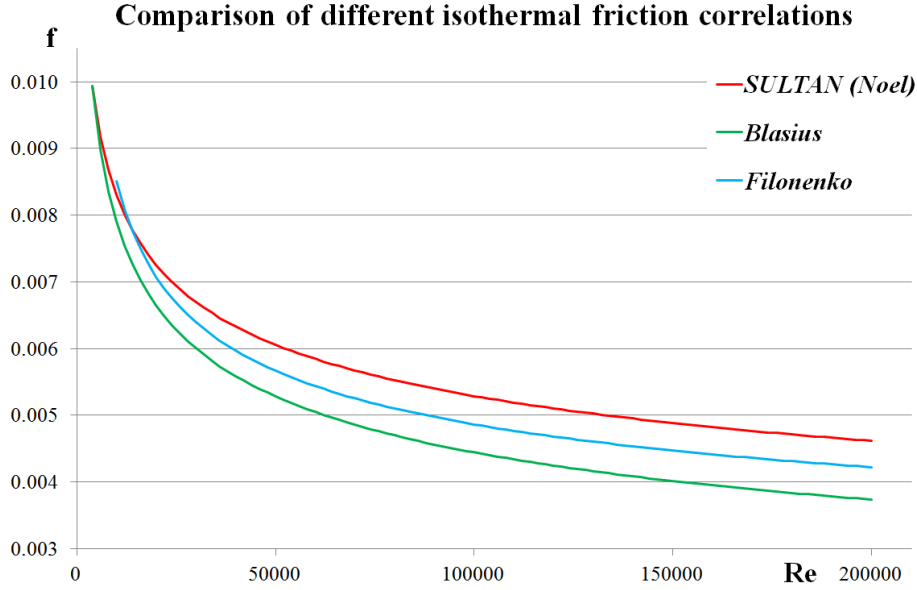


Figure 4.5: Comparison of the different turbulent Fanning friction factor correlations.

Figure 4.5 shows that the best-fitting over SULTAN-JHR experiments (indicated as *SULTAN (Noel)*) predicts an higher friction factor compared to Filonenko correlation. In particular, the average discrepancy between the two correlations was estimated equal to 7 %.

The assessment of the turbulent friction factor in the heated experiments led a modified isothermal friction correlation with a corrective factor F_{cor} :

$$f_{turb} = F_{cor} \times f_{iso,turb} \quad (4.11)$$

$$F_{cor} = 1 - \frac{P_h}{P_w} \frac{0.0085(T_w - T_b)}{1 + 2 \left[\frac{T_w + T_b}{200} \right]^{1.5}} \quad (4.12)$$

The corrective factor is based on the models used in the sub-channel thermal-hydraulic code FLICA-4 [44], but the coefficients were optimized with respect to the SULTAN-JHR data for SE3. This expression was also verified for the experimental data of SE4.

The correlations in Eqn. (4.10), (4.11) and (4.12) have been therefore selected for JHR modeling and implemented in CATHARE.

4.3 Laminar and transition heat transfer modeling

In this section, the prediction of the laminar and transition heat transfer coefficients is assessed. A literature review is first presented; then the different models are compared with the available SULTAN-JHR experimental data.

4.3.1 Laminar heat transfer coefficient

The heat transfer coefficient in fully-developed laminar flows is constant and does not depend on the Reynolds and Prandtl number. In CATHARE, Eqn. (2.45) is applied, where the Nusselt number is equal to 3.66.

For rectangular channels, a different equation is usually suggested (e.g. in [15], [34], [35] and [33]). It is the Marco and Han correlation [45]:

$$Nu = 8.235 f(AR) = 8.235 (1 - 2.0421AR + 3.0853AR^2 - 2.4765AR^3 + 1.0578AR^4 - 0.1861AR^5) \quad (4.13)$$

It was developed for the case of heat flux imposed to walls with high thermal conductivity.

From the literature review, the Marco and Han relationship is considered the best option for fully-developed laminar single-phase heat transfer in rectangular channels. The possible entrance effects on the heat transfer coefficient are discussed in Section 4.3.3.

From this analysis, the Marco and Han correlation, with an aspect ratio equal to 0.0352 (i.e., intermediate between the one for SE3 and SE4), is recommended for the modeling of JHR. It has been implemented in CATHARE as:

$$Nu_{lam} = 7.67 \quad (4.14)$$

4.3.2 Transition heat transfer coefficient

As in the case of the friction factor, no fully-established correlation for the modeling of the heat transfer in the transition flow regime could be found.

Hausen equation (as reported in [39]) could be mentioned:

$$Nu = 0.116(Re^{2/3} - 160)Pr^{1/3} \left[1 + \left(\frac{D_h}{L} \right)^{2/3} \right] \left(\frac{\mu_b}{\mu_w} \right)^{0.11} \quad (4.15)$$

It is valid in the transition zone (i.e. $2300 < Re < 6000$) for a parallel plate duct configuration with uniform wall temperatures at both walls. The presence of a term that takes into account of the eventual entrance effect at the beginning of the test section.

The Hausen correlation was modified by Wang et al. [39]:

$$Nu = 0.04(Re^{2/3} - 160)Pr^{1.5} \left[1 + \left(\frac{D_h}{L} \right)^{2/3} \right] \left(\frac{\mu_b}{\mu_w} \right)^{0.11} \quad (4.16)$$

This new version was derived from experiments in a rectangular channel with aspect ratio 0.05, and it is valid in the ranges: $2500 < Re < 7500$, $2.2 < Pr < 3.5$. The main difference between Eqn. (4.15) and (4.16) is the exponent for the Prandtl number: in rectangular channels the dependency on the latter seems stronger.

4.3.3 Entrance effects

In the previous sections, the discussion was focused on the assessment of the correlations for fully developed flows (i.e. far away from the entrance). When the flow is not fully developed, three possible conditions are possible, namely [16]:

- *Hydro-dynamically developing flow*
- *Thermally developing flow*
- *Simultaneously developing flow*

The hydro-dynamically developing flow is important in the isothermal cases when the velocity profile is not fully developed. In the thermally developing flow, the radial temperature profile has not yet reached its final shape while the velocity profile is fully developed. This regime is described by the use of the Graetz number:

$$Gz = \frac{D_h}{z} RePr \quad (4.17)$$

which indicates the time (or distance) needed by the heat in order to reach the center of the fluid. This dimensionless number can be used as an effective way to define the boundaries of the thermal entrance region. It was also observed that the length of the developing region in laminar flows is longer compared to the one for the turbulent case [16].

In the case of turbulent flows, the use of the standard correlations for the heat transfer in the developing region is conservative and leads to small discrepancies between the predicted and measured wall temperatures. Furthermore, the effect of the entrance plays a role only in a small part of the duct and it can be assumed that the flow becomes fully developed if $L/D_h > 20$.

Conversely, the entrance effects are particularly important for laminar flows. Theoretical solutions of the momentum and energy equations valid for specific laminar flow conditions and specific geometries may be found. Several works have been reported in literature (e.g. [46] and [47]) where the entrance effects improve significantly the heat transfer. This improvement is generated by the growth of the thermal boundary layer. In fact, the change in temperature profile (from uniform at the entrance to parabolic when the flow is fully developed) determines an increase of the heat transfer coefficient [48]. Unfortunately these results are very difficult to generalize.

It can be also noticed that the laminar heat transfer coefficient and the laminar-turbulent transition in the developing flow region are dependent on several parameters: the entrance configuration (e.g. abrupt or smooth), the distance from the entrance, the boundary conditions (e.g. uniform heat flux or constant wall temperature), the channel geometry and the flow conditions (e.g. Reynolds and Prandtl number). Therefore it is very difficult to obtain a reliable correlation, which is valid in all geometries and flow conditions, if the flow is not fully-developed.

4.3.4 Comparison with SULTAN-JHR data

In this section the few data, at low Reynolds numbers, that are available from the SULTAN-JHR heated tests, are analyzed. These data are related to four selected tests performed in SE3: 3C1S3_P9W30T25_015, 3C1S3_P9W30T25_016, 3C1S3_MIP2W30T25_005 and 3C1S3_MIP2W30T25_006. In all of them the transition flow regime could be observed at the entrance of the test section, where the Reynolds number is sufficiently low.

Figure 4.6 shows an example of the measured and simulated behavior of the wet wall temperature along the channel (red lines compared with the black marks). The CATHARE calculation is based on Eqn. (4.32), that is the turbulent heat transfer correlation developed from the SE3 experiments (details of the correlation are discussed in Section 4.4.2). The main fact from this figure is that the axial profile of the wet wall temperature cannot be fully captured when the standard approach of CATHARE is used, since the turbulent heat transfer correlation is applied along the entire channel (see also discussion in Section 4.1). In particular, the temperature is under-estimated in the first half of the pipe, where the laminar-turbulent transition occurs.

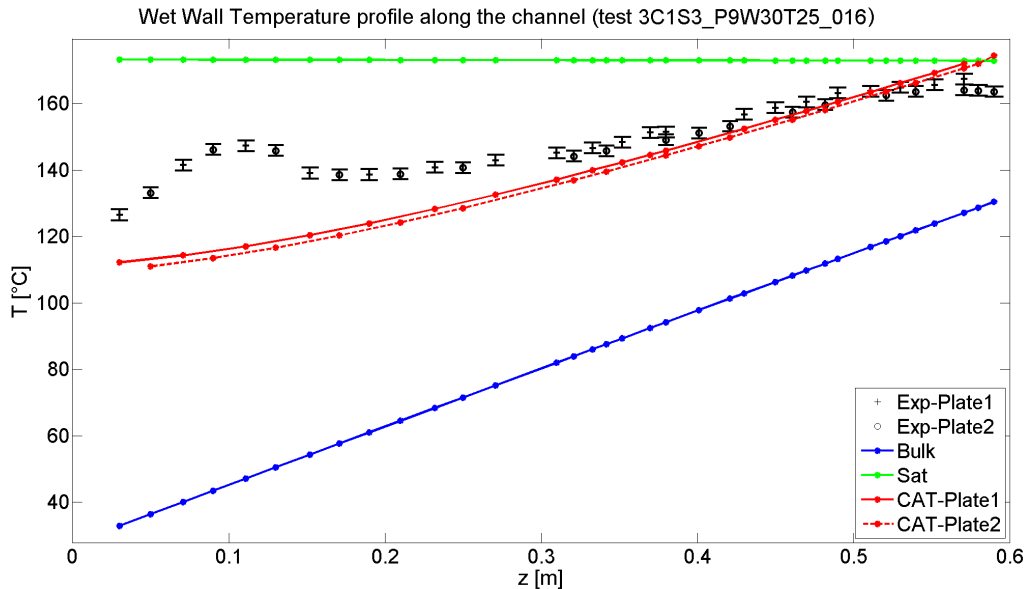


Figure 4.6: Axial temperature profile of the test 3C1S3_P9W30T25_016.

Assuming that the laminar-turbulent transition occurs in the Reynolds range equal to 3500-5500, the wall temperature profile (dashed red line) in Figure 4.7 is obtained. In the figure, the wall temperatures are calculated with CATHARE using the turbulent heat transfer correlation in Eqn. (4.32). Two simulations are compared: one with the standard modeling approach (Eqn. (2.36)) and one with a transition in the range $3500 < Re < 5500$. The use of this transition Reynolds range seems to capture reasonably the onset of the fully turbulent flow, but the wall temperatures at the entrance of the channel are significantly over-estimated. It is thus confirmed that the entrance effects are important for an accurate prediction of the heat transfer coefficient in the laminar and transition flow regime. In particular, the correlations valid for fully developed flows may under-predict the heat transfer when applied in the region close to the channel inlet.

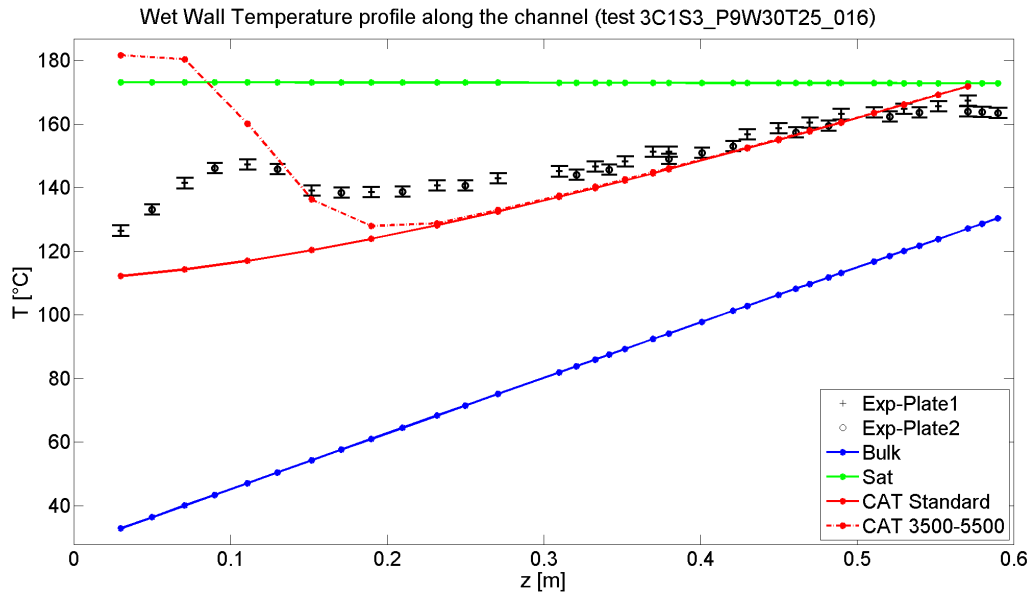


Figure 4.7: Predicted temperature profile of the test 3C1S3_P9W30T25_016 without modeling of the entrance effects.

As discussed in Section 4.2.2, a general and unique definition of the transition Reynolds range for heated tests is very difficult to obtain since it depends on the geometry (e.g. abrupt or smooth entrance) and on the flow conditions (e.g. Prandtl number). Such a complexity comes out from the experiments as well; in fact, different onsets of the fully-developed turbulent flow are observed in the different tests. This can be deduced comparing Figure 4.7 and 4.8, where the transition is modeled in the same range $3500 < Re < 5500$.

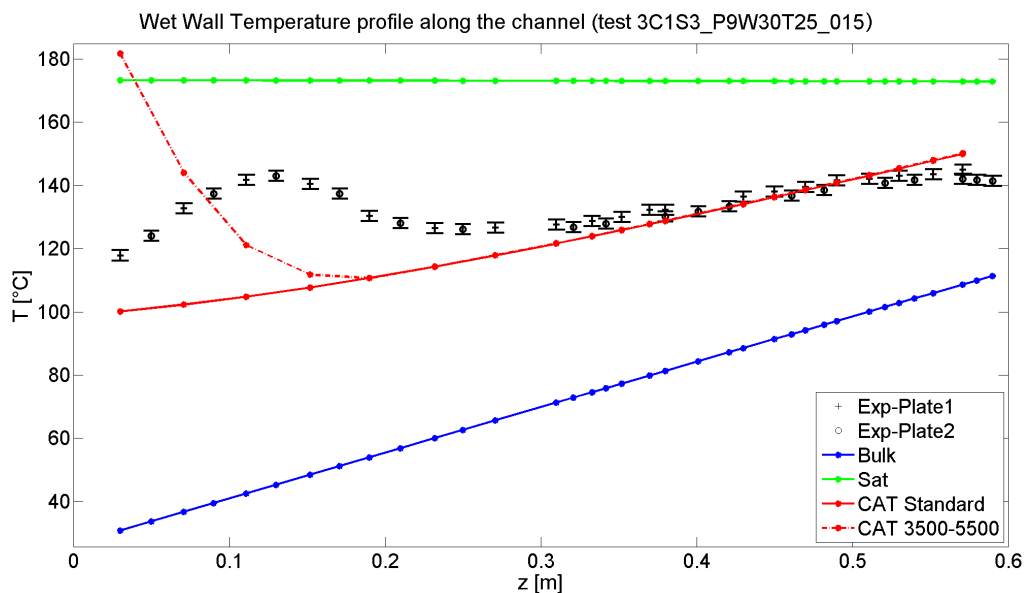


Figure 4.8: Predicted temperature profile of the test 3C1S3_P9W30T25_015 without modeling the entrance effects.

The onset of the fully-developed turbulent flow in the analyzed heated tests varied

approximately between Reynolds number equal to 5000 and 7000, confirming the delay in the departure from laminar flow reported in the literature (see Section 4.2.2). However, no clearly defined transition Reynolds range could be identified due to the complexity of the phenomenon and the lack of experimental data.

The experimental heat transfer coefficients in the transition zone (assumed to occur in the Reynolds range 3500-5500) are compared to the correlations in the literature.

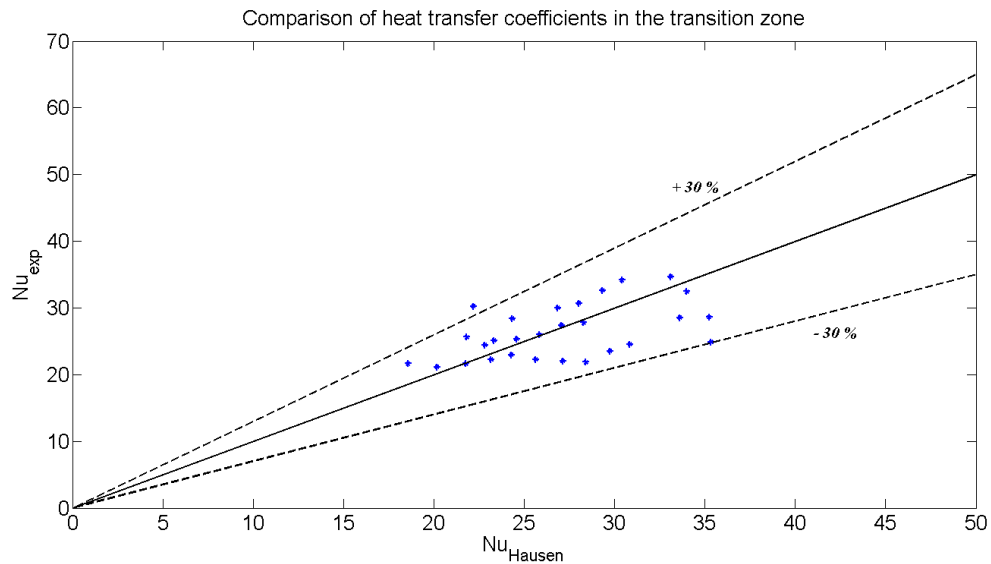


Figure 4.9: Comparison between the experimental Nusselt number and the one predicted by Hausen correlation in the transition zone.

The Hausen correlation (see Eqn. (4.15)), which was designed for a parallel plate configuration and takes into account the entrance effects, gives reasonable results. Most of the experimental points are found in the range $\pm 30\%$, as shown in Figure 4.9.

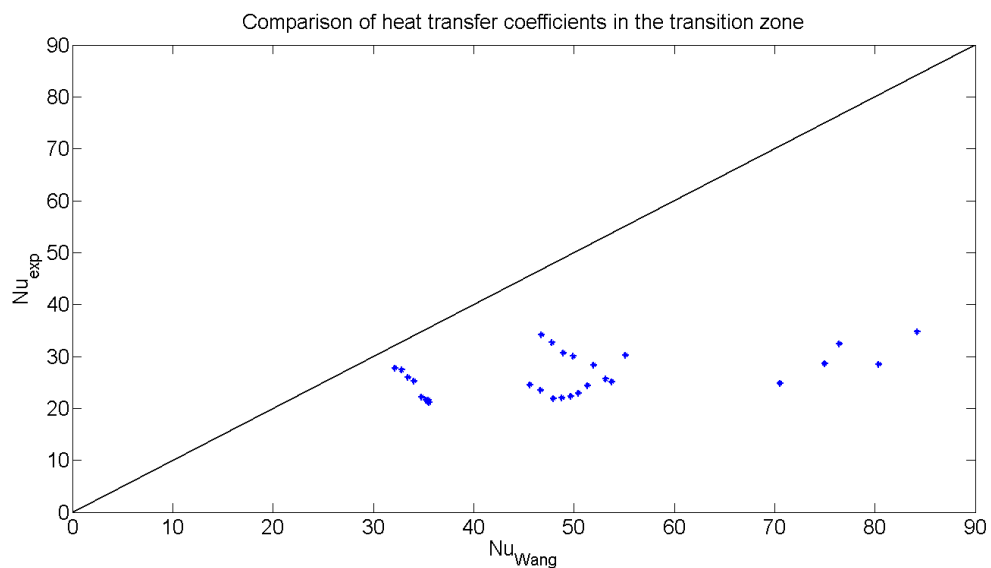


Figure 4.10: Comparison between the experimental Nusselt number and the one predicted by Wang correlation in the transition zone.

On the contrary, Wang correlation in Eqn. (4.16) is not able to predict the correct values, as shown in Figure 4.10. The discrepancies may be explained with the excessive importance given to the Prandtl number.

The use of Hausen equation may determine an improvement of the wall temperature prediction, but large uncertainties remain in the estimation of the laminar-turbulent transition interval. Future investigations would be essential for a better understanding of the laminar-turbulent transition and for a more accurate modeling.

4.4 Turbulent heat transfer modeling

In this section, the analysis is focused on the improvement of the single-phase turbulent heat transfer coefficient for narrow rectangular channels in forced convection. The results from *Paper I* [49] are discussed, improved and complemented.

For the assessment of the heat transfer coefficient, the SULTAN-JHR experimental data have been selected according to the following criteria:

- Single-phase flow, i.e. wet wall temperature below the saturation temperature: $T_w < T_{sat} - 5 \text{ }^\circ\text{C}$
- Stable flow, i.e. only stable tests were considered, as discussed in Section 3.3.4
- Turbulent flow, i.e. $Re > 10000$
- Only the central part of the test section was taken into account, as shown in Table 4.2. To avoid entrance effects, L/D_h was taken larger than 60 for SE3 and larger than 40 for SE4. This led to the exclusion of the temperature measured at the locations of the first 4 thermocouples. The last thermocouples at the end of the heated length (4 in SE4 and 9 in SE3) were also removed in order to rule out the possible influence of the axial conduction on the results. More thermocouples were excluded in SE3 due to their incoherent behavior. In particular, an axial decrease (or reduced increase) in the wall temperature profile was occasionally observed in the last 100 mm of the heated test section. This phenomenon did not occur in SE4.

Table 4.2: List of the thermocouples for the current study.

SE3	TP5 - TP30	$111 \leq z \text{ [mm]} \leq 490$
SE4	TP5 - TP35	$111 \leq z \text{ [mm]} \leq 552$

- $T_w - T_l > 5 \text{ }^\circ\text{C}$. The reason of this condition is to reduce the influence of the experimental errors of the wet wall temperature. In fact the experimental Nusselt number is equal to the imposed heat flux divided by the temperature difference $T_w - T_l$ (see Eqn. (3.28)). Thus, if the temperature difference is too small (as in the case of low heat flux and high mass flow rate), the Nusselt number would be highly affected by the experimental error of the wet wall temperature.

Based on these requirements, a coherent group of experimental data for the analysis could be identified. A total number of 1723 and 1036 experimental points were retrieved for SE3 and SE4, respectively.

The Reynolds number is therefore in the range: $1.0 \cdot 10^4 < Re < 2.69 \cdot 10^5$ and the Prandtl number: $1.2 < Pr < 6$.

These criteria represent an improvement in comparison to the ones used in *Paper I* [49]. The differences between the two selection criteria are:

- the flow was considered fully turbulent when $Re > 5500$ (in the current study, $Re > 10000$)
- less thermocouples were considered for SE4 analysis, as shown in Table 4.3. This selection was based on the conservative criterion $L/D_h > 60$ and the same length was eliminated from the analysis both at the entrance and at the exit of the channel.

Table 4.3: List of analyzed thermocouples in *Paper I* [49].

SE3	TP5 - TP30	$111 \leq z [mm] \leq 490$
SE4	TP9 - TP24	$190 \leq z [mm] \leq 421$

The new database is larger since more experimental points are included for SE4. This allows a better statistics for the best-fitting of a new correlation. Nevertheless, it should be highlighted that the main results (e.g. the correlations from the best-fitting of the experimental results) and conclusions have minor differences between the two cases.

In the following sections, only the results obtained for the updated database are analyzed and discussed.

4.4.1 Selected correlations from the literature

The modeling of the single-phase turbulent heat transfer coefficient in narrow rectangular channels at high Reynolds number have been investigated in a limited number of publications. These studies were carried out in the 1960s and led to contradictory results. In particular, Levy et al. [50] studied the turbulent heat transfer in a rectangular channel of 2.54×63.5 mm in the range $10^4 < Re < 10^5$. An under-prediction of the heat transfer coefficient by 30-45 % compared to the Seider-Tate correlation was reported. Conversely, Gambill and Bundy [22] found slightly higher heat transfer coefficients than the one predicted by the Seider-Tate correlation, using several rectangular channels with gap sizes in the range 1.09-1.45 mm and water flowing upward in a range $9000 < Re < 2.7 \cdot 10^5$.

In the open literature, because of the lack of experimental data, it is usually suggested the use of standard correlations for circular pipes (e.g. the Dittus-Boelter correlation) where the hydraulic diameter is introduced as characteristic length [16].

On the other hand, over the last 20 years, several studies were performed in micro-channels for micro-electronics applications. Short channel lengths and small hydraulic diameters ($D_h \leq 1$ mm) have been usually employed and an heat transfer enhancement has been often observed (e.g. in [51]). Adams et al. [51] performed experiments in circular micro-channels in the diameter range 0.102-1.09 mm, with water flow in the

Reynolds range 2600-23000. The experimental Nusselt numbers were higher than those estimated with the standard Gnielinski correlation. Moreover, an increased enhancement was observed as the channel diameter decreased. This suggested an effect of the channel geometry with narrow flow areas. These investigations in micro-channels were however realized at low Reynolds numbers (usually $Re < 20000$), so that they are not particularly suitable for the application in the JHR reactor.

The lack of reliable experimental data for the turbulent heat transfer in narrow rectangular channels led to the decision of performing the SULTAN-JHR experiments. In the following sub-sections, the experimental Nusselt number will be compared to the predictions of selected correlations from the literature.

Dittus-Boelter correlation

The Dittus-Boelter correlation [17] was derived for circular pipes and its application may be extended to other geometries with the use of the hydraulic diameter. This equation, as introduced by McAdams [52], can be written as:

$$Nu = 0.023Re^{0.8}Pr^{0.4} \quad (4.18)$$

The correlation is applicable for $0.7 < Pr < 120$, $10000 < Re < 1.24 \cdot 10^5$ and $L/D_h > 60$. As discussed in Section 2.2.5, the Dittus-Boelter correlation is the standard model implemented in CATHARE.

The comparison with the SULTAN-JHR experimental data shows that the Dittus-Boelter correlation significantly under-estimates the heat transfer coefficient, especially at high Reynolds number (see Figure 4.11).

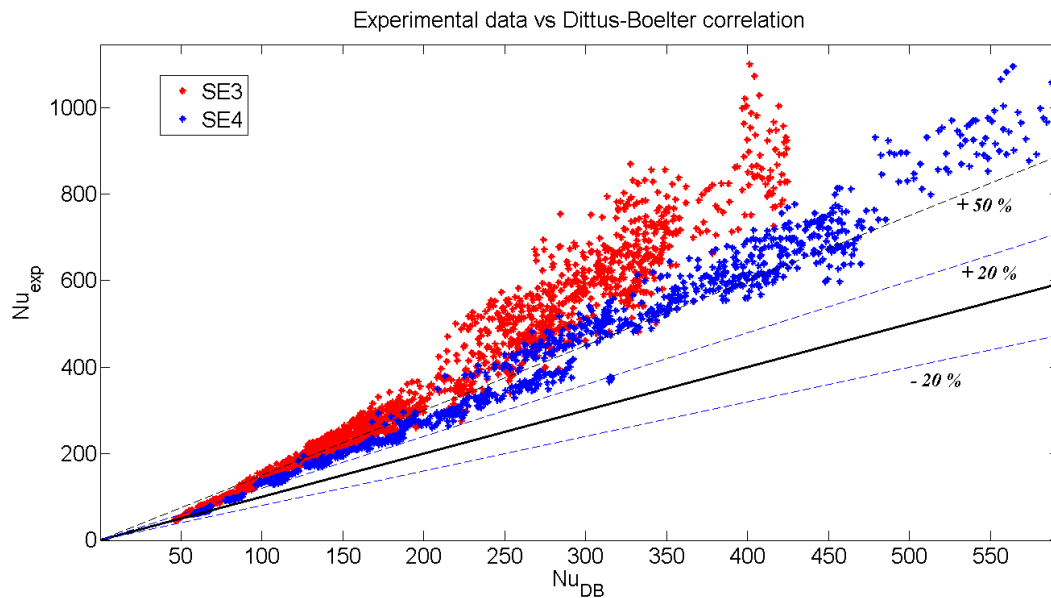


Figure 4.11: Comparison of the experimental data with Dittus-Boelter correlation.

The correlation may be considered to be accurate both for SE3 and SE4 up to a Reynolds number equal to 25000, but then the discrepancies grow bigger with the increase of the Reynolds number. The observed discrepancies between the experimental data in SE3 and SE4 due to the channel geometry will be discussed in Section 4.4.3.

The under-estimation of the heat transfer coefficient leads to the over-prediction of the wall temperatures.

Sieder-Tate correlation

The Sieder-Tate correlation [53] was derived for circular pipes and it reads:

$$Nu = 0.027 Re^{0.8} Pr^{\frac{1}{3}} \left(\frac{\mu}{\mu_w} \right)^{0.14} \quad (4.19)$$

The correlation is applicable for $0.7 < Pr < 120$, $Re > 10000$ and $L/D_h > 60$. The difference of liquid viscosity between the wall and bulk is taken into account with the viscosity ratio $\frac{\mu}{\mu_w}$.

The comparison with the experimental data in Figure 4.12 shows a significant under-prediction of the heat transfer coefficient. Nevertheless, an improvement of the predictions can be observed compared to the Dittus-Boelter correlation.

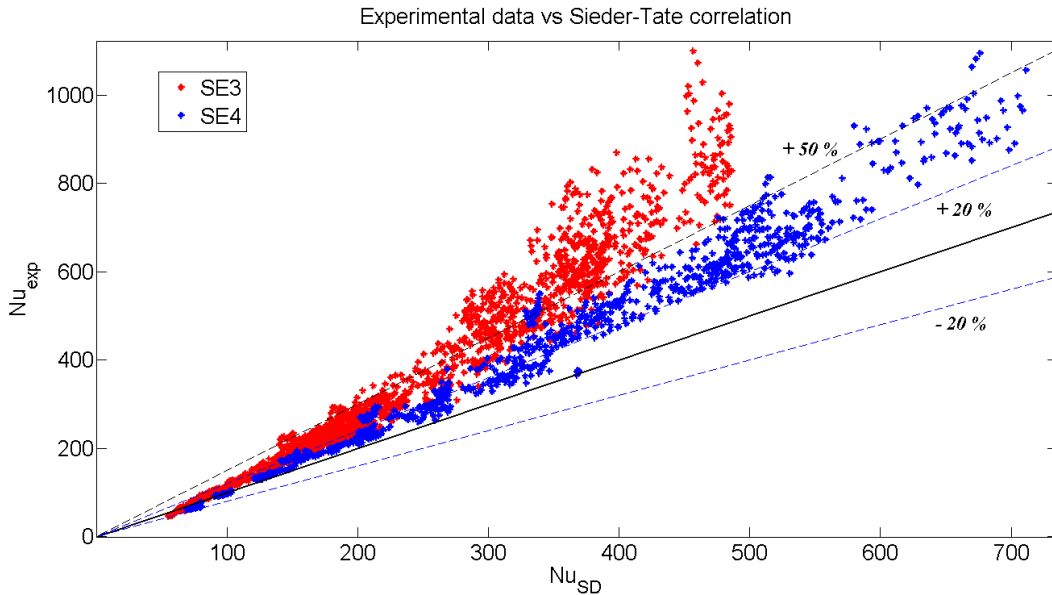


Figure 4.12: Comparison of the experimental data with Sieder-Tate correlation.

Gnielinski correlation

The Gnielinski correlation [54] was obtained from the Popov-Petukhov correlation [55] for circular pipes:

$$Nu = \frac{\frac{f_G}{2} (Re - 1000) Pr}{1 + 12.7 \left(\frac{f_G}{2} \right)^{0.5} \left(Pr^{\frac{2}{3}} - 1 \right)} \quad (4.20)$$

$$f_G = (1.58 \ln Re - 3.28)^{-2} \quad (4.21)$$

It is valid in the range: $2300 < Re < 5 \cdot 10^6$, $0.5 \leq Pr \leq 2000$ and it can be therefore used in the laminar-turbulent transition zone.

The correlation is usually regarded as one of the most accurate [16] and it is implemented in the system code TRACE [6].

The Gnielinski correlation also under-estimates the heat transfer coefficient, as shown in Figure 4.13.

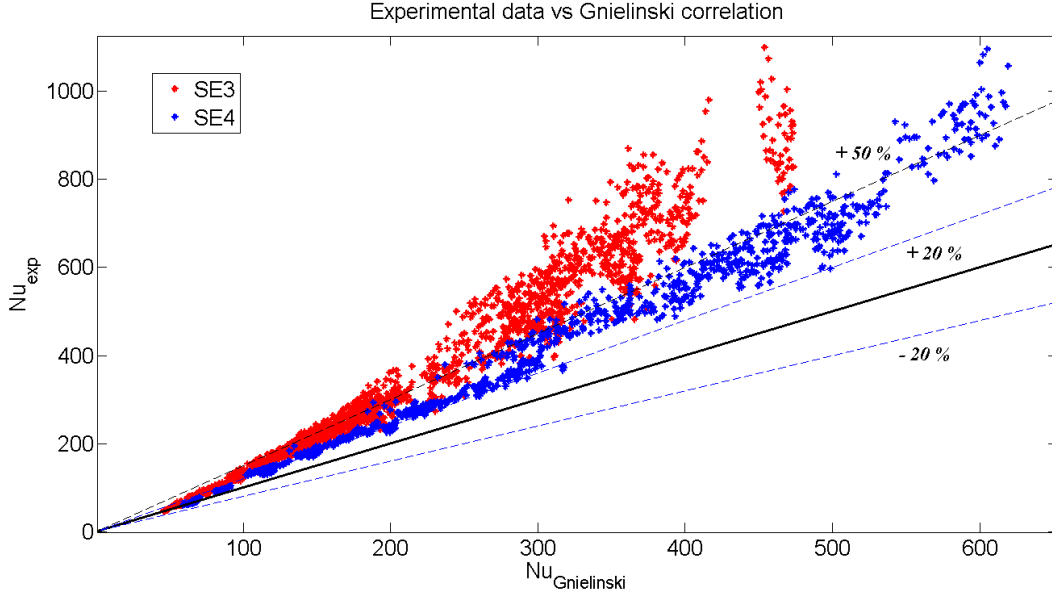


Figure 4.13: Comparison of the experimental data with Gnielinski correlation.

Popov-Petukhov correlation

The Popov-Petukhov correlation [55] reads:

$$Nu = \frac{\frac{f_P}{8} Re Pr \left(\frac{\mu}{\mu_w} \right)^{0.11}}{(1 + 3.4 f_P) + \left[11.7 + \frac{1.8}{Pr^{\frac{1}{3}}} \right] \left(\frac{f_P}{8} \right)^{0.5} \left(Pr^{\frac{2}{3}} - 1 \right)} \quad (4.22)$$

The Popov-Petukhov correlation was originally developed for fully-developed turbulent flow in circular pipes. It was therefore corrected by Siman-Tov et al. [43] for rectangular geometry, by making use of the Filonenko friction correlation:

$$f_P = \frac{\left[1.0875 - 0.1125 \left(\frac{e_{ch}}{l_{ch}} \right) \right]}{(1.82 \log_{10} Re - 1.64)^2} \quad (4.23)$$

Also, the correction for the change of the physical variables at the wall (under the form of the viscosity ratio) was introduced by Siman-Tov et al. [43]. The validity range of the modified correlation is: $10000 < Re < 1.25 \cdot 10^5$, $2.0 \leq Pr \leq 140$.

This correlation was used for the preliminary modeling and design of the Advanced Neutron Source Reactor (ANSR) at Oak Ridge National Laboratory (ORNL), which had a similar design to the JHR reactor (i.e. parallel aluminum-clad fuel plates with water channel gaps of 1.27×70 mm). Experimental evidence from the Thermal-Hydraulic Test Loop (THTL) with a 1.27×12.7 mm rectangular channel, seemed

to indicate a significant under-estimation of the heat transfer coefficient [56]. Nevertheless, the THTL experimental heat transfer coefficients were not considered to be reliable, due to the high uncertainties associated to the wet wall temperature measurements in the rectangular channel made of aluminum. In fact, the measurements of temperature were highly affected by the oxidation of the heated surface and the non-constant electrical resistivity of the aluminum with the temperature. Furthermore, the use of a short channel width (equal to 12.7 mm, i.e. $AR = 0.1$) was believed to cause a significant heat conduction towards the two corners. It should be noticed that the use of the Inconel-600 in the SULTAN-JHR experiments solves the issues connected to the aluminum and the larger channel width reduces the effects of the heat conduction towards the corners, allowing an almost uniform heat flux in the plates [23] (see also discussion in Section 3.3.1 and 3.3.2).

As the other standard correlations, the modified Popov-Petukhov correlation still underestimates the experimental points, (see Figure 4.14).

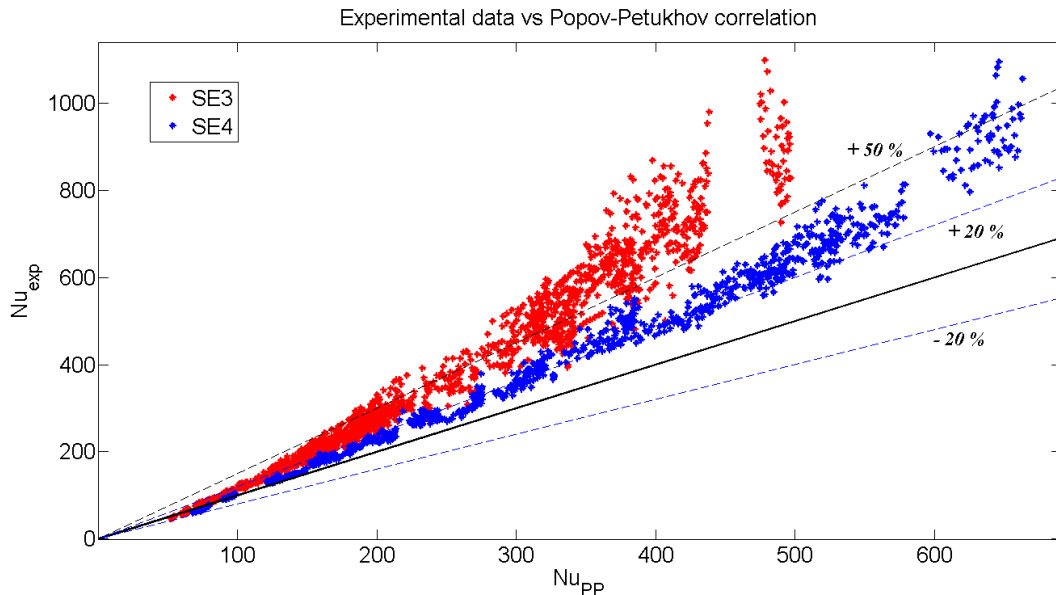


Figure 4.14: Comparison of the experimental data with Popov-Petukhov correlation.

Rique-Siboul correlation

The correlation of Rique-Siboul [57] was developed at CEA-Grenoble in 1972 for the forced convection of water in circular pipes of small diameters (i.e. 2 and 4 mm), at high heat flux ($1.5 < \phi < 8 \text{ MW}/\text{m}^2$), and low pressure ($0.15 < p < 0.5 \text{ MPa}$). It reads:

$$Nu = 0.0092 Re^{0.88} Pr^{0.5} \left(\frac{\mu}{\mu_w} \right)^{0.14} \quad (4.24)$$

The correlation is valid in the range: $10000 < Re < 147000$, $2.5 < Pr < 9.2$. It was therefore developed for conditions that are similar to the ones in the SULTAN-JHR tests. In spite of this, Figure 4.15 shows that the heat transfer is still under-predicted.

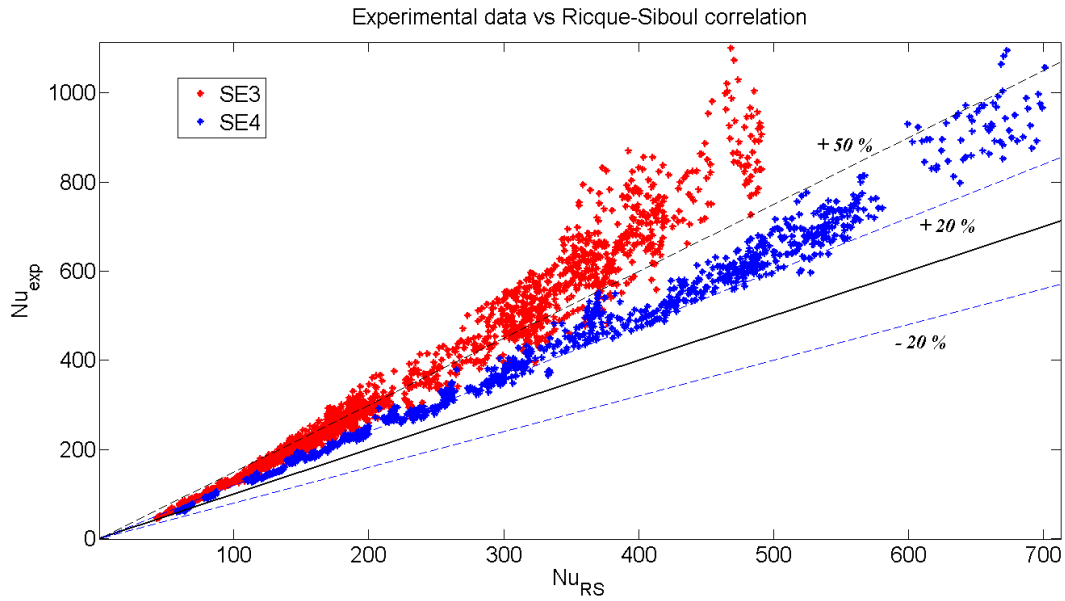


Figure 4.15: Comparison of the experimental data with Ricque-Siboul correlation.

Liang correlation

The correlations that were specifically developed for narrow rectangular channels by Liang et al. [37] and by Ma et al. [35] were also tested.

The correlation of Liang et al. is based on experimental data for a rectangular test section of 1.8 x 50 x 800 mm, with a pressure range between 0.5 and 5 MPa; low heat fluxes between 4 and 50 kW/m²; and Reynolds number between 2300 and 6150. It reads:

$$Nu = 0.00666 Re^{0.933} Pr^{0.4} \quad (4.25)$$

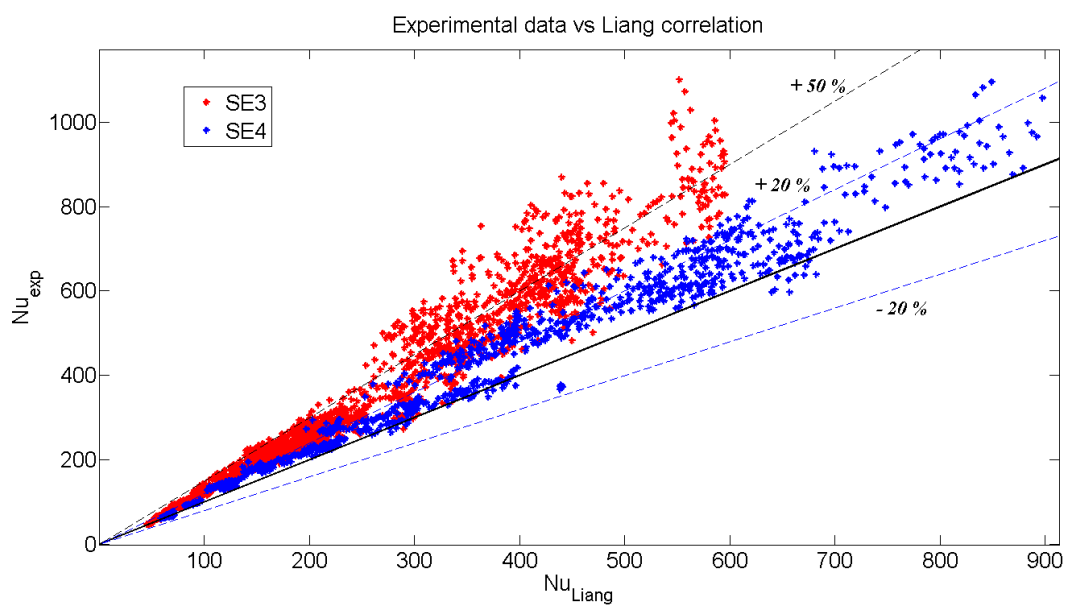


Figure 4.16: Comparison of the experimental data with Liang correlation.

The correlation underestimates the SULTAN-JHR experimental data, even though it performs relatively better for test section SE4 (see Figure 4.16).

This correlation was built in a Reynolds number interval that corresponds mainly to the transition from laminar to turbulent flow in narrow rectangular channels, so its validity may be quite questionable in the turbulent region.

Ma correlation

The correlation of Ma et al. [35] was developed from experiments performed in a rectangular test section of 2 x 40 x 1092 mm, at atmospheric pressure, with heat fluxes between 14 and 214 kW/m² and Reynolds numbers between 4000 and 13000. It reads:

$$Nu = 0.00354Re^{1.0}Pr^{0.4} \quad (4.26)$$

The geometry of the test section is close to the one in SE4, although the heat fluxes are lower and the range of variation of the Reynolds number is smaller in comparison with the SULTAN-JHR tests.

The results for this correlation are shown in Figure 4.17.

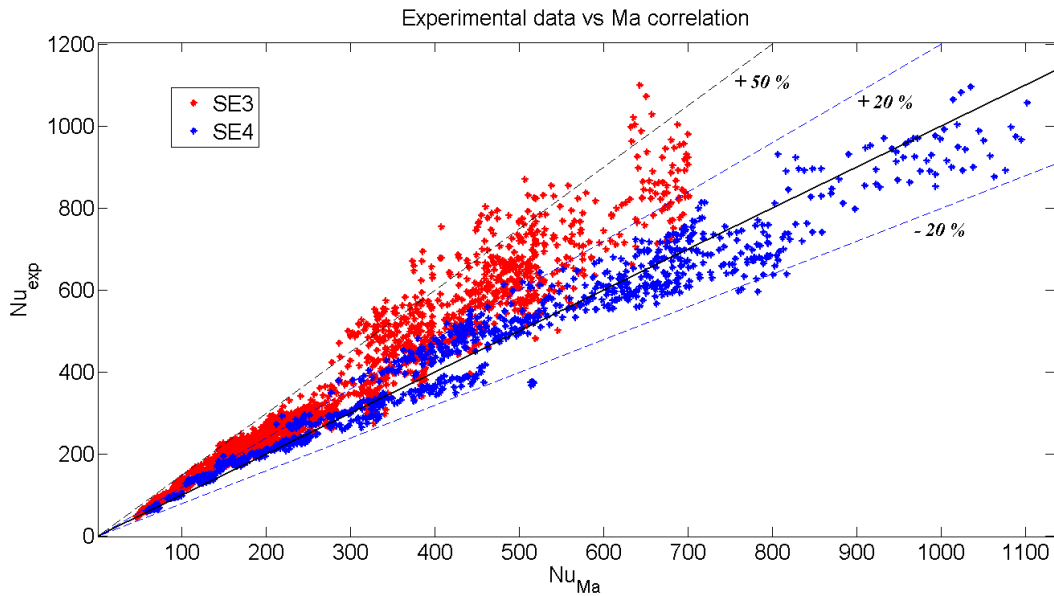


Figure 4.17: Comparison of the experimental data with Ma correlation.

A good agreement was reached with the experimental points from test section SE4 (i.e. the test section similar to the one used by Ma et al.): the error is within $\pm 20\%$ and no significant bias could be observed. On the other hand, a large underestimation is again obtained for SE3.

4.4.2 Development of a correlation based on the SULTAN-JHR data

As previously discussed, no reliable correlation is available in the open literature for highly turbulent flow in narrow rectangular channels.

Furthermore, the comparison of the SULTAN-JHR experimental data with the most promising existing correlations showed that the heat transfer coefficients may be significantly under-estimated. Therefore, a new correlation was developed from a best-fitting of the SULTAN-JHR data. Two different forms of the correlation were considered, i.e.

- Dittus-Boelter form:

$$Nu = aRe^{b_{Re}} Pr^{c_{Pr}} \quad (4.27)$$

- Seider-Tate form:

$$Nu = aRe^{b_{Re}} Pr^{c_{Pr}} \left(\frac{\mu}{\mu_w} \right)^{0.14} \quad (4.28)$$

The coefficients of Eqn. (4.27) and (4.28) were optimized with a multiple linear regression approach. This procedure was applied to the data for SE3 and SE4 separately, since an effect of the channel geometry was observed (see Section 4.4.3).

Best-fitting of the SE4 experimental data

The best fitting correlation for the test section SE4 with the Dittus-Boelter form reads:

$$Nu = 0.0047Re^{0.961} Pr^{0.581} \quad (4.29)$$

The statistical analysis of this best-fitting gives a coefficient of determination $R^2 = 0.992$ and a standard deviation $\sigma = 0.0612$, which indicates that the experimental points are well fitted by the correlation as also shown in Figure 4.18.

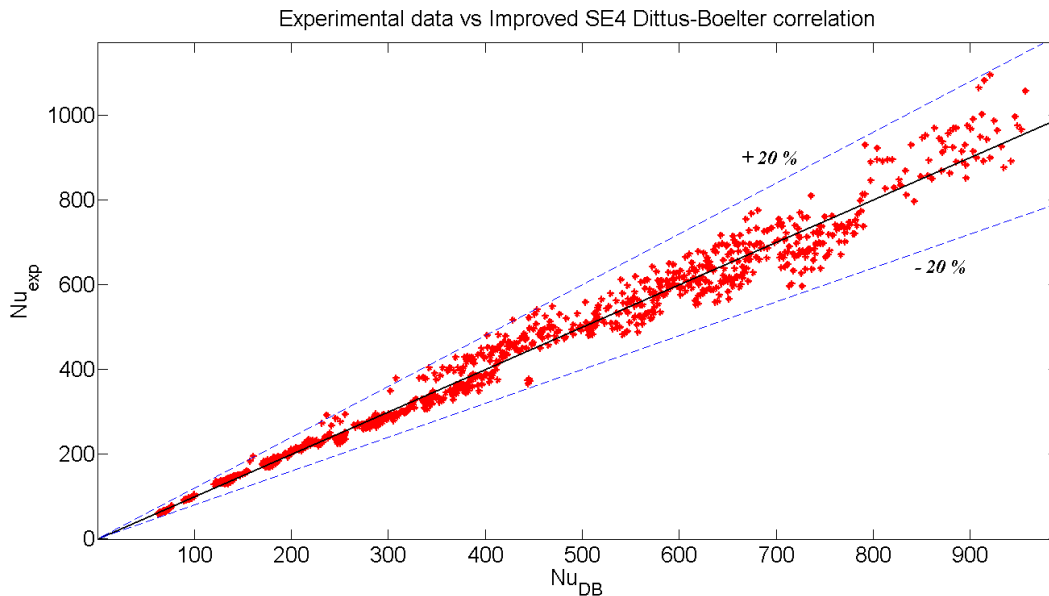


Figure 4.18: SE4 Dittus-Boelter best-fitting (4.29).

The residuals of the correlation were computed as:

$$\frac{Nu_{predicted} - Nu_{exp}}{Nu_{exp}} \quad (4.30)$$

where $Nu_{predicted}$ and Nu_{exp} are the predicted and the experimental Nusselt numbers.

The residuals are distributed according to a Gaussian curve (Figure 4.19 and 4.20). The correlation has a bias (calculated as the average of the residuals) equal to 0.19 %.

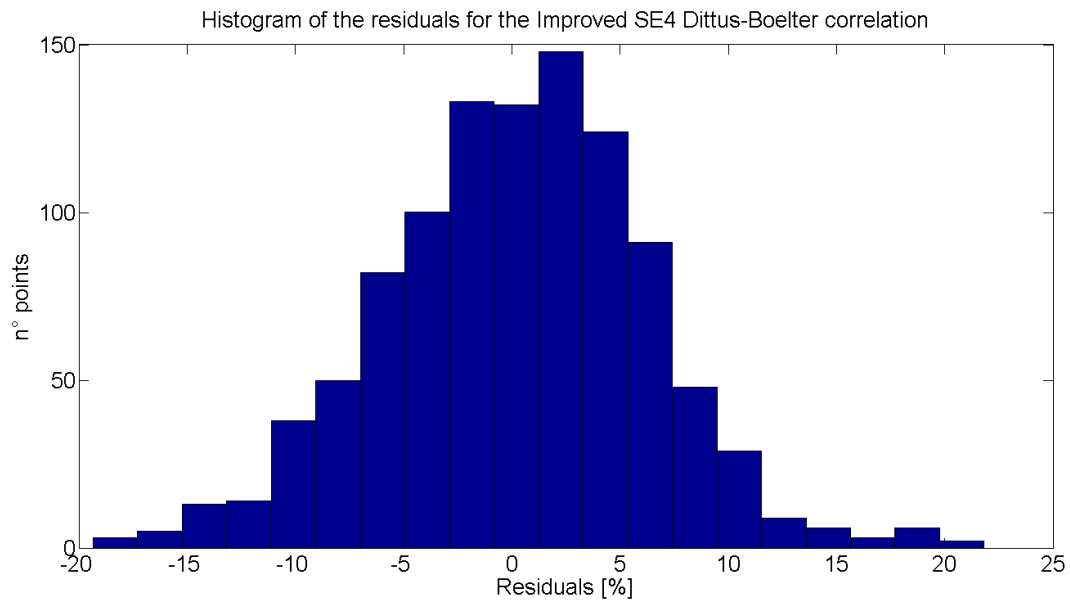


Figure 4.19: Histogram of the residuals for the SE4 Dittus-Boelter best-fit (4.29).

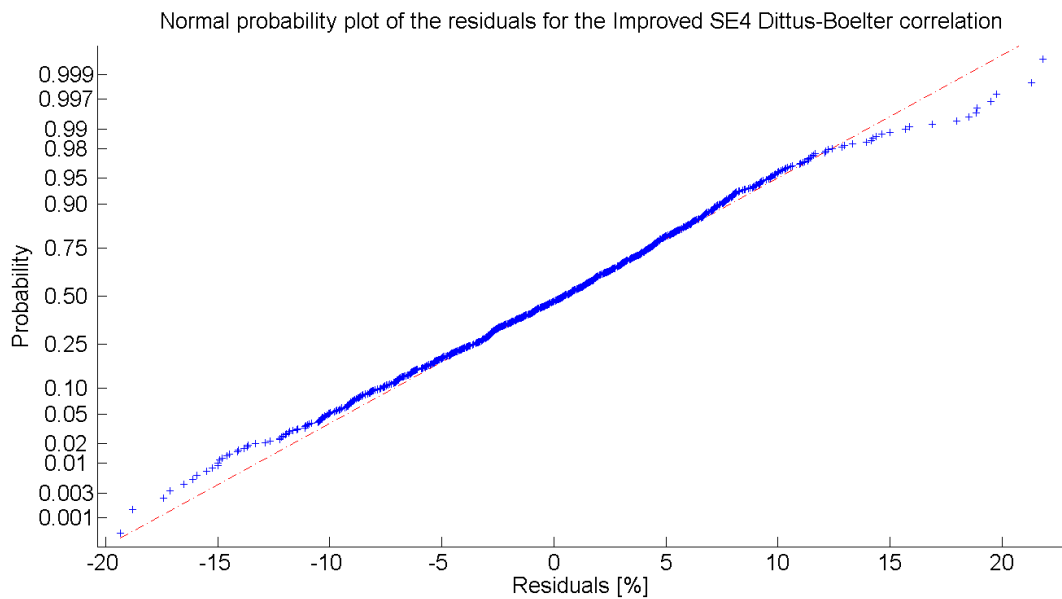


Figure 4.20: Normal probability plot of the residuals for the SE4 D-B best-fit (4.29).

Analogously, the best fitting correlation with the Seider-Tate form was obtained:

$$Nu = 0.0045 Re^{0.960} Pr^{0.568} \left(\frac{\mu}{\mu_w} \right)^{0.14} \quad (4.31)$$

The correlation fits well the experimental points, as shown in Figure 4.21, 4.22 and 4.23.

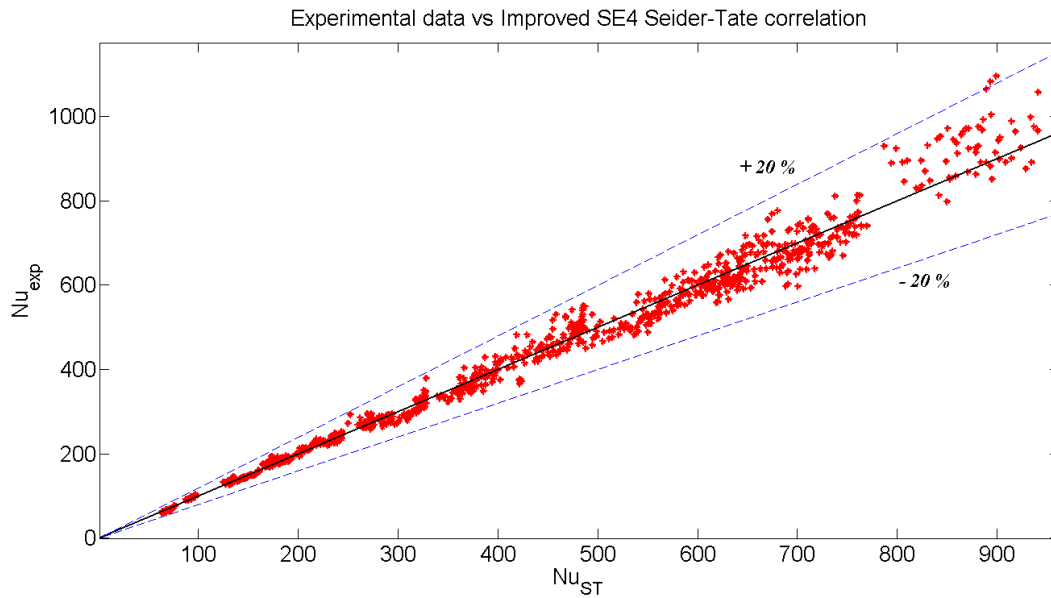


Figure 4.21: SE4 Seider-Tate best-fitting (4.31).

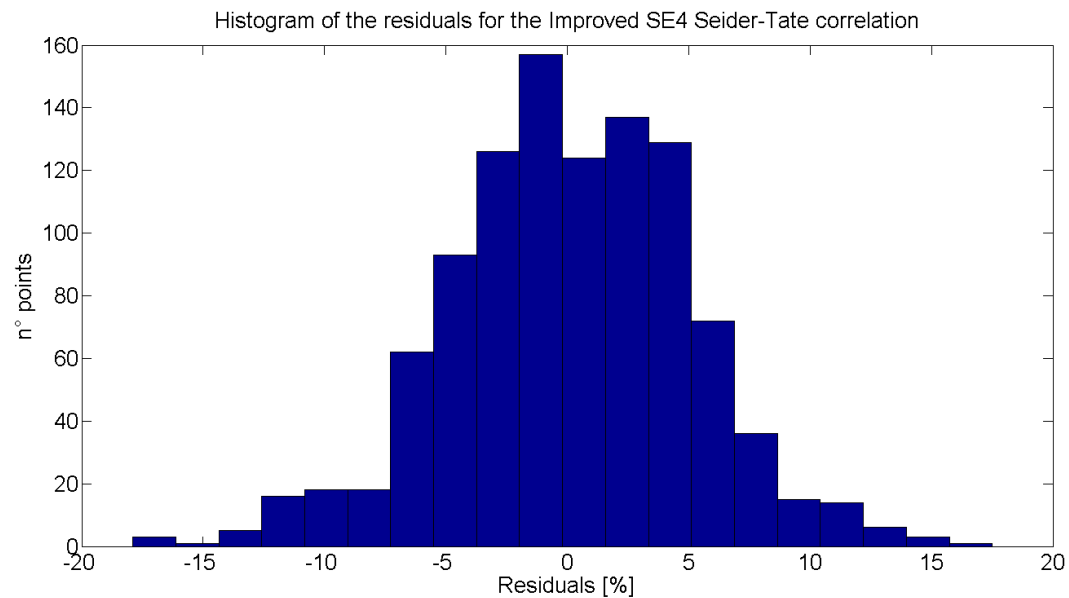


Figure 4.22: Histogram of the residuals for the SE4 Seider-Tate best-fit (4.31).

Its associated uncertainty is equal to 10.04 % and the bias is 0.13 %, and it is slightly better than the best-fitting with the Dittus-Boelter form given by Eqn. (4.29).

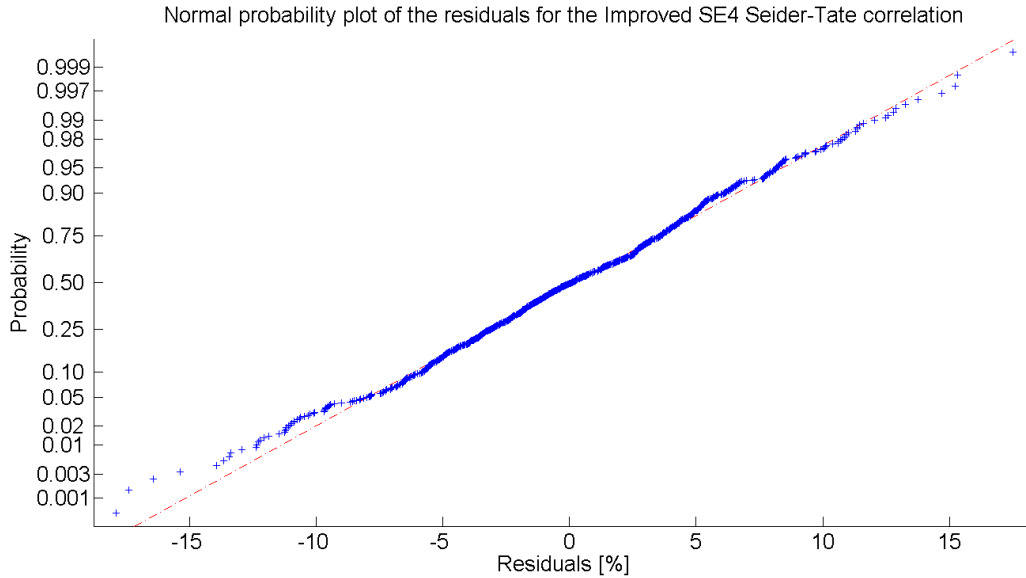


Figure 4.23: Normal probability plot of the residuals for the SE4 S-T best-fit (4.31).

The Seider-Tate based best-fitting was chosen for the SE4 tests since better predictions could be achieved at high heat flux. This is due to the fact that the correlation includes the viscosity ratio. In fact the tests at high heat fluxes usually present a lower viscosity at the wall (in comparison with the liquid bulk) that flattens the velocity profile, so that the heat transfer coefficient improves. Nevertheless, this enhancement is not very marked: Figure 4.24 and 4.25 show that, at different heat fluxes, similar Nusselt numbers are obtained if the same Reynolds number is considered.

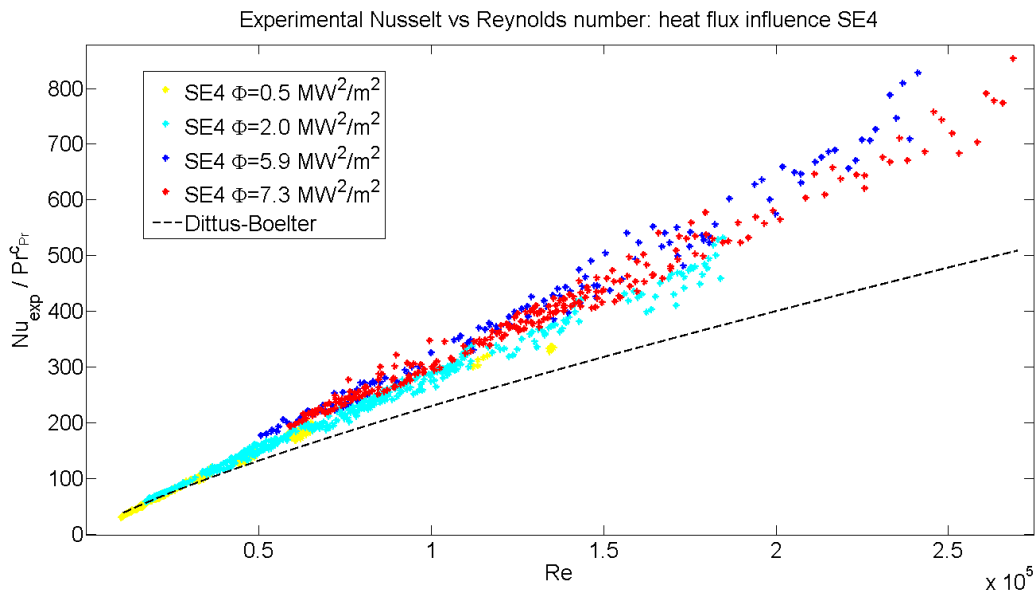


Figure 4.24: Heat flux influence over the experimental Nusselt number for SE4.

In these figures, it is possible to visualize more clearly the effect of the Reynolds number on the heat transfer. To do so, in the y-axis the experimental Nusselt number is divided by the Prandtl number to the power of the coefficient c_{Pr} , as it is from the Dittus-Boelter best-fitting.

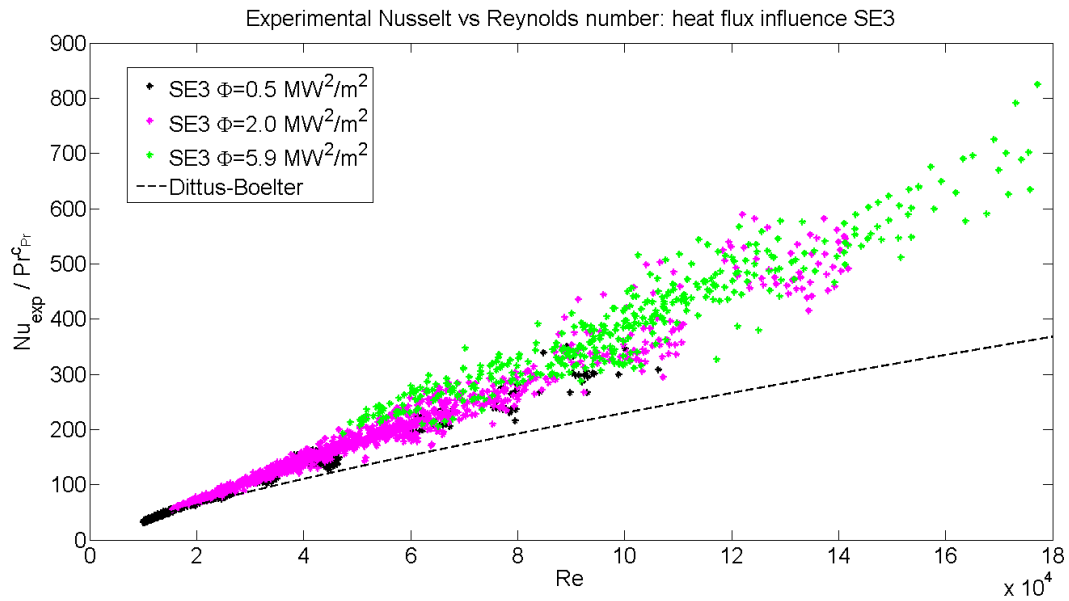


Figure 4.25: Heat flux influence over the experimental Nusselt number for SE3.

Best-fitting of the SE3 experimental data

As regards test section SE3, the best fitting with the Dittus-Boelter form is:

$$Nu = 0.0021 Re^{1.050} Pr^{0.627} \quad (4.32)$$

with a coefficient of determination equal to 0.983.

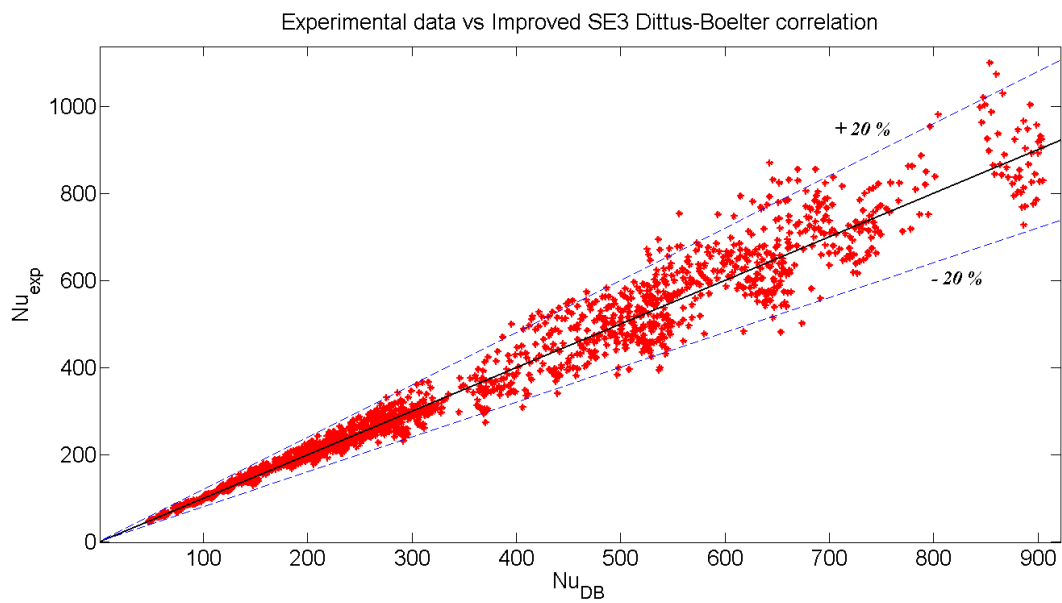


Figure 4.26: SE3 Dittus-Boelter best-fitting (4.32)

The SE3 experimental data has a larger dispersion compared to the ones in SE4, as shown in Figure 4.26, 4.27 and 4.28. The correlation has therefore a larger (but still small) associated uncertainty 2σ equal to 17.64 % and a bias equal to 0.38 %.

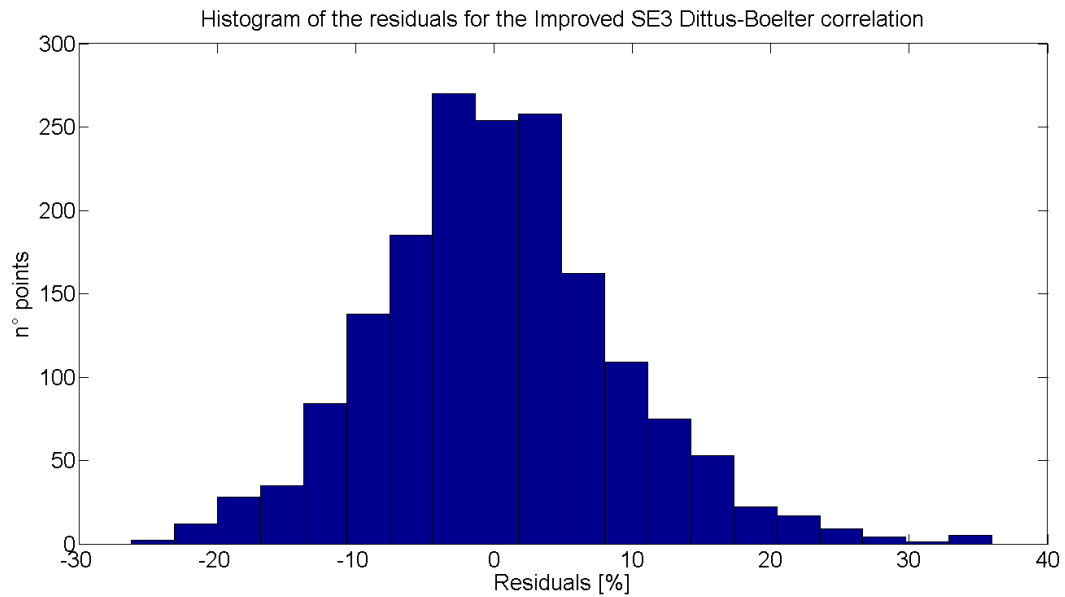


Figure 4.27: Histogram of the residuals for the SE3 Dittus-Boelter best-fit (4.32).

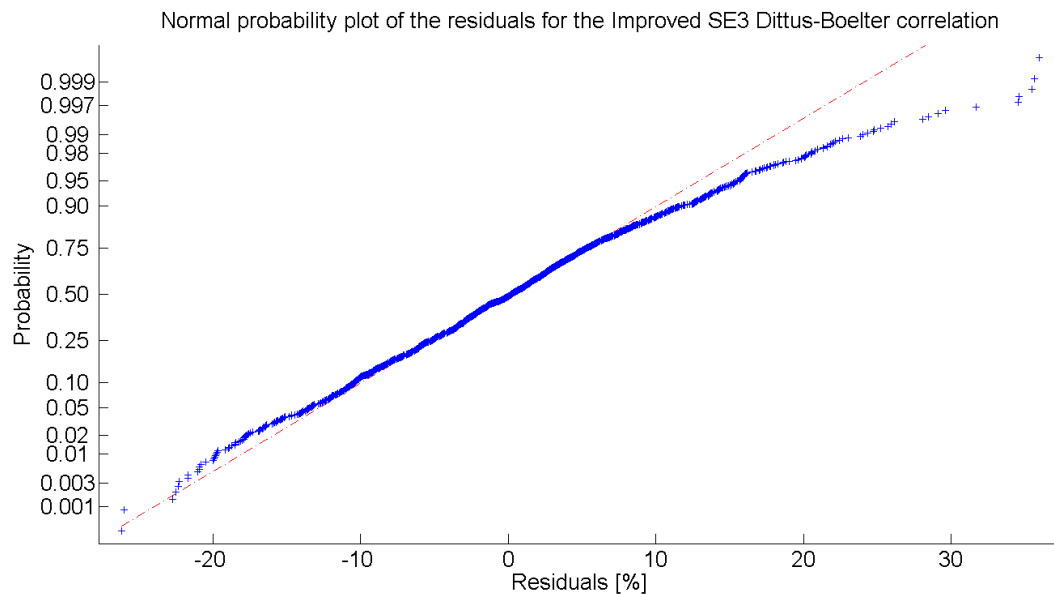


Figure 4.28: Normal probability plot of the residuals for the SE3 D-B best-fit (4.32).

The best fitting correlation with the Seider-Tate form becomes:

$$Nu = 0.0019 Re^{1.056} Pr^{0.618} \left(\frac{\mu}{\mu_w} \right)^{0.14} \quad (4.33)$$

The correlation has a very similar statistics to the one with the Dittus-Boelter form, but a slight improvement can be observed in the associated uncertainty, which is equal to 16.72 %. This correlation has been therefore chosen for the SE3 modeling.

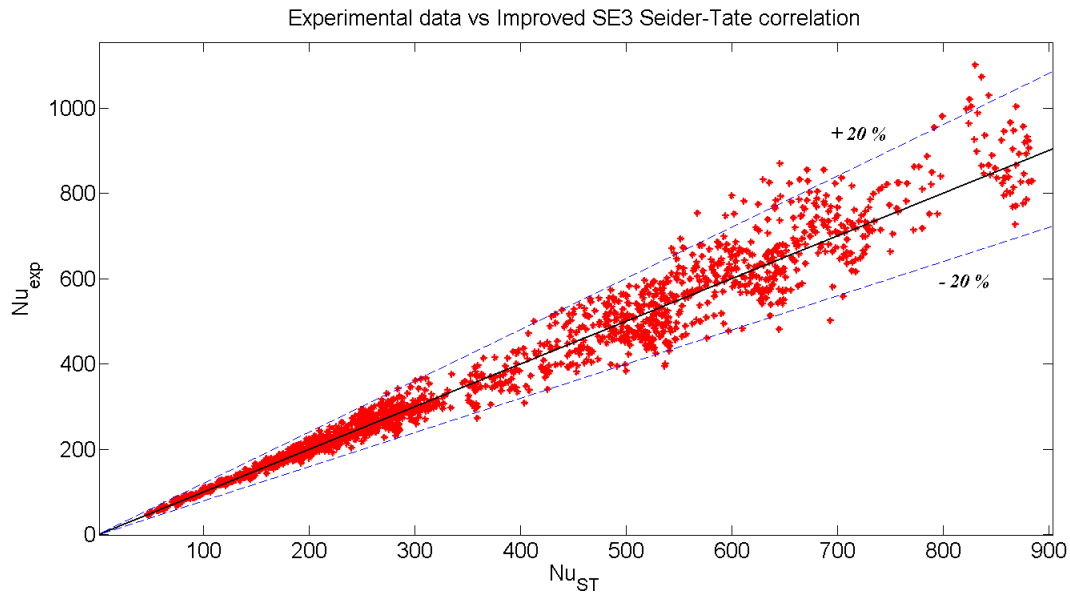


Figure 4.29: SE3 Seider-Tate best-fitting (4.33).

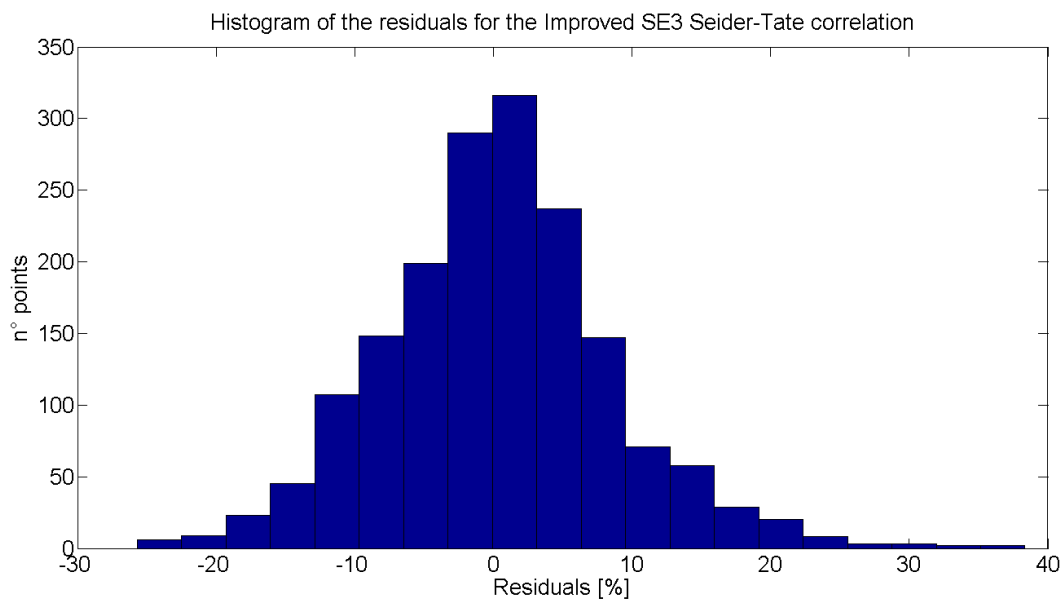


Figure 4.30: Histogram of the residuals for the SE3 Seider-Tate best-fit (4.33).

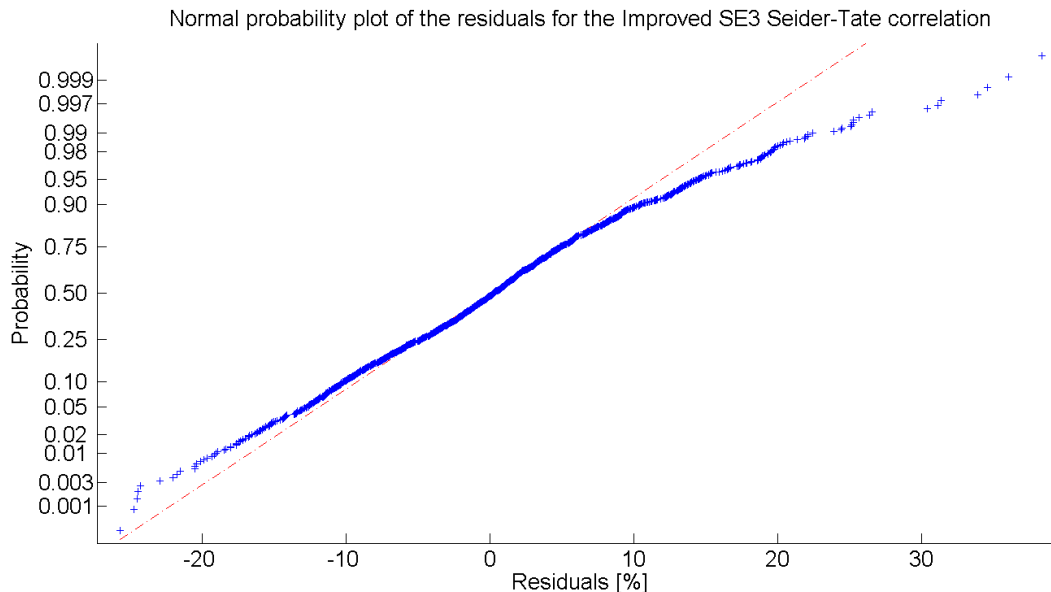


Figure 4.31: Normal probability plot of the residuals for the SE3 S-T best-fit (4.33).

Summary of the best-fitting correlations

The best-fitting correlations with their coefficients and the specific geometric parameters of the relative test section are summarized in Table 4.4.

Table 4.4: Summary of the best-fitting coefficients and geometry of the channel.

Correlation	gap[mm]	AR	a	b _{Re}	c _{Pr}	$\frac{\mu}{\mu_w}$
DB SE4 (4.29)	2.16	0.0417	0.0047	0.961	0.581	-
ST SE4 (4.31)	2.16	0.0417	0.0045	0.960	0.568	0.14
DB SE3 (4.32)	1.51	0.0287	0.0021	1.050	0.627	-
ST SE3 (4.33)	1.51	0.0287	0.0019	1.056	0.618	0.14
Dittus-Boelter	-	1	0.023	0.8	0.4	-
Seider-Tate	-	1	0.027	0.8	0.333	0.14

The statistical properties of the best-fitting are given in Table 4.5, and they demonstrate that the procedure applied to derive the correlations was successful.

Table 4.5: Summary of the best-fitting statistics.

Correlation	points	R ²	2σ [%]	Bias [%]	95 per. [%]	Min-Max [%]
DB SE4 (4.29)	1036	0.992	12.24	0.19	-12.1 - 11.6	-19.3 - 21.8
ST SE4 (4.31)	1036	0.995	10.04	0.13	-10.7 - 10.1	-17.9 - 17.5
DB SE3 (4.32)	1723	0.983	17.64	0.38	-16.7 - 19.7	-26.2 - 36.0
ST SE3 (4.33)	1723	0.985	16.72	0.35	-15.7 - 18.8	-25.7 - 38.3

In Table 4.5, the column "95 per." provides the range in which 95 % of the residuals falls. "Min-Max" indicates the maximum and minimum values of the calculated residuals.

As previously discussed, the best-fitting correlations with the Seider-Tate form (i.e. Eqn. (4.31) and (4.33)) have been chosen for the modeling in narrow rectangular channels because of the better statistics and an improved performance at high heat flux. These correlations are valid for fully-developed turbulent flows in the range: $1.0 \cdot 10^4 < Re < 2.69 \cdot 10^5$ and $1.2 < Pr < 6$.

4.4.3 Influence of the channel geometry

The comparison between the two test sections SE3 and SE4 points out that the channel geometry can affect the heat transfer coefficient, as displayed in Figure 4.32.

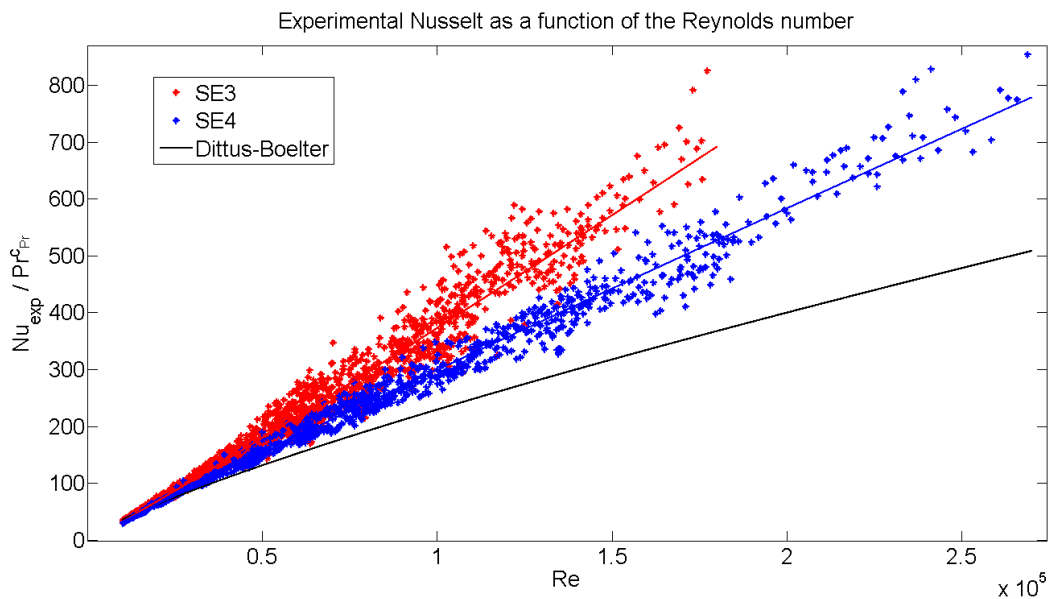


Figure 4.32: Nusselt number as a function of the Reynolds number.

The heat transfer coefficient becomes higher in SE3 which has a smaller channel gap. Therefore an enhancement of the heat transfer occurs with the decrease of the channel gap. The discrepancies between the two test sections grow with the increase of the Reynolds number, as indicated by the different power coefficient b_{Re} associated to the Reynolds number (see Table (4.4)). In fact, the change of the channel gap mainly impacts the proportional coefficient a , as well as the power coefficient b_{Re} , rather than the contribution related to the Prandtl number. Table 4.4 also includes the aspect ratio AR . This dimensionless parameter is often used for the characterization of the heat transfer in rectangular channels. It is particularly important in laminar flow (see Section 4.3.1), and it is also used in the Filonenko friction correlation for turbulent flows (see Eqn. (4.9)). In the case of the test sections SE3 and SE4 the reduction of the gap corresponds to smaller values of AR , as the channel width remains approximately constant. Thus, it was not possible to deduce which parameter between the gap and the aspect ratio play the major role in the heat transfer. This question along with a generalized correlation for narrow rectangular channel of any gap/ AR size, require further studies.

4.5 Summary and suggested correlations

A summary of the suggestions for the improvement of CATHARE with respect to the single-phase modeling of JHR is presented.

The turbulent flow regime is of major interest in the analysis. Nevertheless, the improved modeling of the transition zone could reduce the non-conservatism and be useful for the analysis of particular accidental scenarios with low mass flow rates (see Sections 4.1 and 4.3.4).

In addition, it must be emphasized that the entrance effects can be important but they are difficult to be taken in proper account with system codes, such as CATHARE. In fact, the use of correlations which depends on the distance from the inlet (e.g. Hausen correlation) would determine a loss of generality of the code. Furthermore the correlations valid for the SULTAN-JHR tests are not necessarily valid for the JHR fuel assemblies, where the entrance to the core channels is abrupt. Therefore the modeling of possible entrance effects has not been included in CATHARE, even though this issue can impact the transient behavior of the core flow. In particular, the entrance effects may determine an improvement of the heat transfer coefficient both in laminar and turbulent flows, so that neglecting them may be considered to be conservative. This improvement is more marked in the case of laminar flows.

From the literature review and from the analysis of the isothermal tests, it is expected that a Reynolds range between 2500 and 4000 is reasonably appropriate for the modeling of the laminar-turbulent transition. The suggested isothermal friction correlations are listed below.

- In the laminar region ($Re < 2500$), Shah-London correlation computed with an intermediate aspect ratio between SE3 and SE4 (equal to 0.0352):

$$f_{iso,lam} = \frac{22.91}{Re} \quad (4.34)$$

- In the turbulent region ($Re > 4000$): Noel correlation based on SULTAN-JHR data:

$$f_{iso,turb} = \frac{0.0505}{Re^{0.196}} \quad (4.35)$$

- In the transition region ($2500 < Re < 4000$): linear interpolation between the laminar and turbulent correlation:

$$f_{iso,trans} = f_{iso,lam,2500} + [f_{iso,turb,4000} - f_{iso,lam,2500}] \frac{Re - 2500}{4000 - 2500} \quad (4.36)$$

The linear interpolation may be considered arbitrary, but it is used to have a continuous friction profile in the transition region. This is necessary for the numerical stability of the CATHARE code.

In case of heated walls, the friction factor in turbulent flow is obtained according to:

$$f_{turb} = F_{cor} \times f_{iso,turb} \quad (4.37)$$

where the corrective factor F_{cor} in Eqn. (4.12) is used. Due to the lack of experimental data, the same correction factor is assumed to be applicable to the laminar and

transition flow regimes. This solution was implemented in CATHARE. However, more studies and experimental data would be required for a full validation of the use of the correction factor in laminar and transition flows.

When heated walls are considered, the departure from laminar flow is known to shift towards higher Reynolds values. Nevertheless, no clear boundaries of the transition region could be identified from both the experiments and the available literature.

The use of a transition range equal to $3500 < Re < 5500$ seems to be excessively conservative (see Figure 4.7 and 4.8), since the entrance effects on the heat transfer cannot be taken into account in a system code. On the other side, the standard approach of CATHARE for the determination of the heat transfer coefficient is clearly non-conservative, as shown in Figure 4.6 and discussed in Section 4.1. Therefore, the use of the isothermal transition range (i.e. $2500 < Re < 4000$) for the heated tests is believed to be a reasonable compromise between the two extremes.

The single-phase heat transfer correlations suggested are reported below:

- In the laminar region ($Re < 2500$): Marco and Han correlation computed with an intermediate aspect ratio between SE3 and SE4 (equal to 0.0352):

$$Nu_{lam} = 7.67 \quad (4.38)$$

- In the turbulent region ($Re > 4000$): improved correlations based on the best-fitting of the SULTAN-JHR SE3 and SE4 experimental data respectively:

$$Nu = 0.0019 Re^{1.056} Pr^{0.618} \left(\frac{\mu}{\mu_w} \right)^{0.14} \quad (4.39)$$

$$Nu = 0.0045 Re^{0.960} Pr^{0.568} \left(\frac{\mu}{\mu_w} \right)^{0.14} \quad (4.40)$$

- in the transition region ($2500 < Re < 4000$): linear interpolation between the laminar and turbulent correlation

$$Nu = Nu_{lam} + [Nu_{turb}(Re = 4000) - Nu_{lam}] \frac{Re - 2500}{4000 - 2500} \quad (4.41)$$

No experimental points are available in the laminar flow regime and the correlation is deduced exclusively from the literature review. Nevertheless the Marco and Han correlation seems to be well established and it was successfully applied in several works. Because of the lack of experimental data, a linear interpolation that guarantees the continuity of the heat transfer coefficient is suggested in the transition region.

The analysis of the turbulent heat transfer coefficient based on the SULTAN-JHR experimental data shows that the standard correlations of Dittus-Boelter, Sieder-Tate, Gnielinski and Popov-Petukhov significantly under-estimate the heat transfer, especially at high Reynolds numbers. In addition, the correlations of Liang et al. and Ma et al., that were specifically designed for narrow rectangular channels, have a limited range of validity and could not lead to accurate results. Therefore, a correlation for each of the two test sections has been developed with a best-fitting approach.

For the best-fitting, the Seider-Tate form of the correlation has been preferred to the Dittus-Boelter one, due to the slightly reduced uncertainties and the improved capabilities at high heat flux. These correlations are valid in the range: $1.0 \cdot 10^4 < Re < 2.69 \cdot 10^5$ and $1.2 < Pr < 6$.

It is also pointed out that the geometry of the narrow rectangular channel plays an important role in the determination of the heat transfer coefficient. In particular, a decrease of the channel gap (or of the aspect ratio) leads to an improvement of the heat transfer coefficient. Further research would be needed to investigate the possibility of having an unique heat transfer correlation that can be valid for both test sections.

These correlations for the friction and heat transfer coefficients have been implemented in CATHARE.

Chapter 5

Two-phase heat transfer modeling

The main goal of the reactor safety analysis is to ensure that the fuel and cladding temperatures are kept below the limits imposed by the safety authorities. In this context, it is important to have a clear understanding of two-phase flows and of the boiling mechanisms, so that reliable predictions can be obtained.

The boiling is a very complex phenomenon and it has been studied for many decades. An extensive analysis of the two-phase heat transfer and its modeling may be found, for example, in [58] and [59]. Nevertheless there are still knowledge gaps and approximations in such a modeling, especially when unconventional flow conditions and channel geometries, as in JHR, are considered.

The two-phase heat transfer may occur either in *pool* or *flow* boiling. The pool boiling is encountered when an heated surface is submerged in a stagnant liquid, while the flow boiling is related to a fluid that flows, under forced or natural convection, in a heated channel. The boiling can be further classified into *steady-state* and *transient* boiling and, depending on the liquid bulk temperature, into *sub-cooled* and *saturated* boiling.

In this chapter, steady-state flow boiling is analyzed in a vertical narrow rectangular channel, in both saturated and sub-cooled conditions. The SULTAN-JHR experimental data are used to assess the validity of the existing models in CATHARE and support recommendations for the application to JHR. In particular, the correlations for the prediction of the wall superheat in Fully Developed Boiling (FDB) are discussed and evaluated. This chapter is based on the research work included in Paper II.

5.1 Physics of flow boiling and modeling

A description of the flow boiling in vertical heated channels is briefly presented in this section, along with a discussion on the possible modeling approaches.

The heat transfer and boiling process in a vertical pipe, with forced sub-cooled liquid at the inlet, and with uniform heat flux at the wall, can be divided in different regimes [58]. These are shown in Figure 5.1.

Accordingly, in the lower part of the channel, the heat transfer is usually governed by single-phase forced convection. At the Onset of Nucleate Boiling (ONB), sub-cooled boiling starts with evaporation of liquid in micro-cavities (or nucleation sites) at the heated walls.

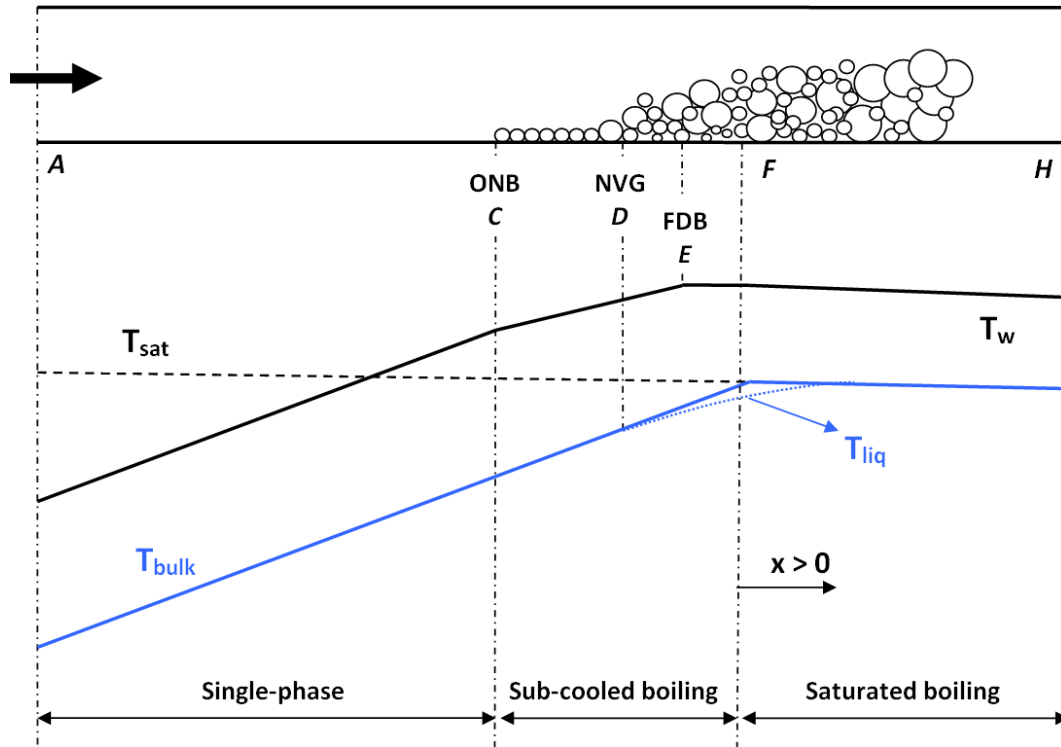


Figure 5.1: Sub-cooled flow boiling schematic in a vertical channel.

The ONB indicates the point along the channel where the first bubbles appear. At the beginning, the bubbles are created in a small number of micro-cavities and do not detach from the heated surfaces since the bulk is highly sub-cooled. The void fraction, which is mainly determined by the balance between the steam generation at the walls and the condensation in the sub-cooled liquid, remains very close to zero. Nevertheless, the increasing formation of vapor at the nucleation sites determines a gradual improvement of the heat transfer coefficient which causes the establishment of relatively low wall superheat ($T_w - T_{sat}$). Thus, the heat transfer mechanism gradually changes from single-phase forced convection to two-phase fully developed nucleate boiling. In particular, the heat transfer regime is characterized by a co-existence of the forced convection and the nucleate boiling mechanism which is thus called *partial boiling* in the literature. The partial boiling region is schematically represented in Figure 5.1 between the ONB (i.e. point C) and the FDB (i.e. point E).

When the bubbles reach a critical size, they detach from the heated surfaces and the net production of void starts to grow significantly. This condition is known as Net Vapor Generation (NVG) or Onset of Significant Void (OSV). The NVG is usually modeled with the Saha-Zuber correlation [19], as discussed in Section 2.2.5.

When the convective heat transfer mechanism becomes negligible, the Fully Developed Boiling (FDB) heat transfer regime starts. Experimentally, it was observed that the FDB heat transfer coefficient depends mainly on the system pressure and the imposed heat flux, while it does not depend on the fluid velocity (or Reynolds number) [58]. This heat transfer mode is very efficient and low wall superheat is observed.

When the flow reaches the saturation conditions, i.e. the steam quality is equal to 0, the region of saturated boiling begins. The void fraction grows and different flow patterns can develop along this region, namely bubbly, slug and annular. The

heat transfer mechanism for saturated boiling is very similar to the one in FDB and similar correlations are often used. Nevertheless, the heat transfer may be enhanced with increasing steam quality thanks to the contribution of the forced convection mechanism. The magnitude of the contribution depends mainly on the heat flux and the mass flow-rate (or liquid velocity) in the channel. As a consequence, the forced convection may be neglected for a flow with high heat flux combined with a relatively low mass flow-rate, while it may play a role if a low heat flux and/or a high mass flow-rate are present [58]. The heat transfer enhancement may be particularly relevant for the annular flow pattern, where the liquid film in contact with the wall moves at high velocity. As a matter of fact, very high heat transfer coefficients has been reported in the literature [58].

The liquid film thickness in the annular flow is constantly reduced along the channel and eventually it goes to zero due to evaporation. The direct contact between the vapor and the heated walls determines a deterioration of the heat transfer coefficient, which causes a significant increase in wall temperature (with a possible damage of the heated wall). This phenomenon is called Dry-Out.

Another thermal crisis process is the so-called Departure from Nucleate Boiling (DNB). During DNB, the boiling mechanism suddenly changes from nucleate boiling to film boiling. A vapor layer prevents the liquid from reaching the heated walls and a sudden deterioration of the heat transfer occurs.

In research reactors (such as JHR), the CHF can also be triggered by the flow excursion phenomenon, which can cause flow-rate redistribution between parallel channels [60].

5.1.1 Modeling of two-phase heat transfer

The modeling approach for the two-phase heat transfer is briefly described here.

The beginning of the sub-cooled region is usually evaluated with an ONB criterion. The formation of first vapor bubble requires a certain wall superheat (i.e. $T_w > T_{sat} + \Delta T_{sat,ONB}$) in order to activate the nucleation sites on the heated surfaces. The correlation of Bergles-Rohsenow [61], which is valid for water at pressure between 0.1 and 13.8 MPa, is usually employed:

$$\Delta T_{sat,ONB} = 0.556 \left[\frac{\phi}{1082 \left(\frac{p}{10^5}\right)^{1.156}} \right]^{0.463 \left(\frac{p}{10^5}\right)^{0.0234}} \quad (5.1)$$

The correlation is fully established for circular pipes, while the verification in narrow rectangular channels would probably require a deeper analysis. However, good results are reported in [62]: the experiments used for the comparison were carried out in a vertical rectangular channel with a 2.25×50 mm test section, and the measurements of ONB were obtained with a visualization technique. The formula may be therefore applied to the SULTAN-JHR experiments.

In the partial sub-cooled boiling region, the heat transfer is usually modeled as a superposition hypothesis, which combines a nucleate boiling term ϕ_{nb} together with a term due to the single-phase forced convection of the liquid ϕ_{fc} .

For example, the model of Bowring [58] may be cited:

$$\phi = \phi_{fc} + \phi_{nb} \quad (5.2)$$

The convective term is computed with appropriate correlations for single-phase forced convection (e.g. Dittus-Boelter), while the nucleate boiling term is expressed with a FDB correlation. The model for the sub-cooled boiling region may be therefore summarized as:

- Single-phase:

$$T_w < T_{ONB} \quad \Longrightarrow \quad \begin{cases} \phi_{fc} = h_{fc}(T_w - T_l) \\ \phi_{nb} = 0 \end{cases} \quad (5.3)$$

- Partial boiling:

$$T_{ONB} \leq T_w \leq T_{FDB} \quad \Longrightarrow \quad \begin{cases} \phi_{fc} = h_{fc}(T_{sat} - T_l) \\ \phi_{nb} = h_{nb}(T_w - T_{sat}) \end{cases} \quad (5.4)$$

- Fully Developed Boiling:

$$T_w > T_{FDB} \quad \Longrightarrow \quad \begin{cases} \phi_{fc} = 0 \\ \phi_{nb} = h_{nb}(T_w - T_{sat}) \end{cases} \quad (5.5)$$

It should be noticed that the liquid sub-cooling $DT_{sub} = T_{sat} - T_{bulk}$ is used as temperature difference in partial boiling, instead of $T_w - T_{bulk}$, which is used in single-phase. Once the FDB region is reached, the single-phase term is put artificially to zero and the wet wall temperature is simply obtained by the FDB correlation. As a consequence, the proposed model creates discontinuities in the heat fluxes both at the ONB and at the FDB point.

Several other models based on a similar superposition hypothesis exist in the literature. The interested reader can find some examples in [58] and [63].

The FDB location z_{FDB} may be obtained with a specific model, derived by Forster and Greif [64]. This model is not employed in system codes for the unnecessary complication that introduces, see discussion in Section 5.1.2. It is therefore not described in this report. Details are described in [58].

The FDB correlations are used for the prediction of the wall superheat until the saturation temperature is reached. Then, specific correlations for saturated flow boiling are usually employed. For this purpose, there is a large number of correlations in the literature [65]. The main idea is generally to combine a nucleate boiling term together with a forced convective term, as in the partial boiling region. A commonly used correlation is the one developed by Chen [66], which assumes an additive superposition for the heat transfer coefficients:

$$h_{chen} = S \cdot h_{nb} + h_{fc} \quad (5.6)$$

where S is a suppression factor for the nucleate boiling term, that was experimentally determined and approaches zero for high steam qualities (since the thin liquid film in annular flows may inhibit the nucleation process). The heat transfer coefficient in nucleate boiling can be calculated, for instance, with the Forster-Zuber correlation. The Dittus-Boelter correlation, computed with an appropriate two-phase Reynolds number, can be used for the forced convection term.

5.1.2 Modeling approach in CATHARE

The two-phase heat transfer modeling approach in CATHARE is described in Section 2.2.5. It is based on Bowring model (5.2) for the sub-cooled boiling region, but the discontinuities in the heat flux are removed. The removal of the discontinuities guarantees the continuity of the calculated parameters in the code, which is necessary for numerical reasons. The implemented modifications can slightly affect the predicted wall temperatures. Figure 5.2 shows a qualitative comparison between a typical discontinuous profile of wall temperature (black line T_w) and a typical wall temperature calculated with CATHARE (red line $T_{w,CATH}$).

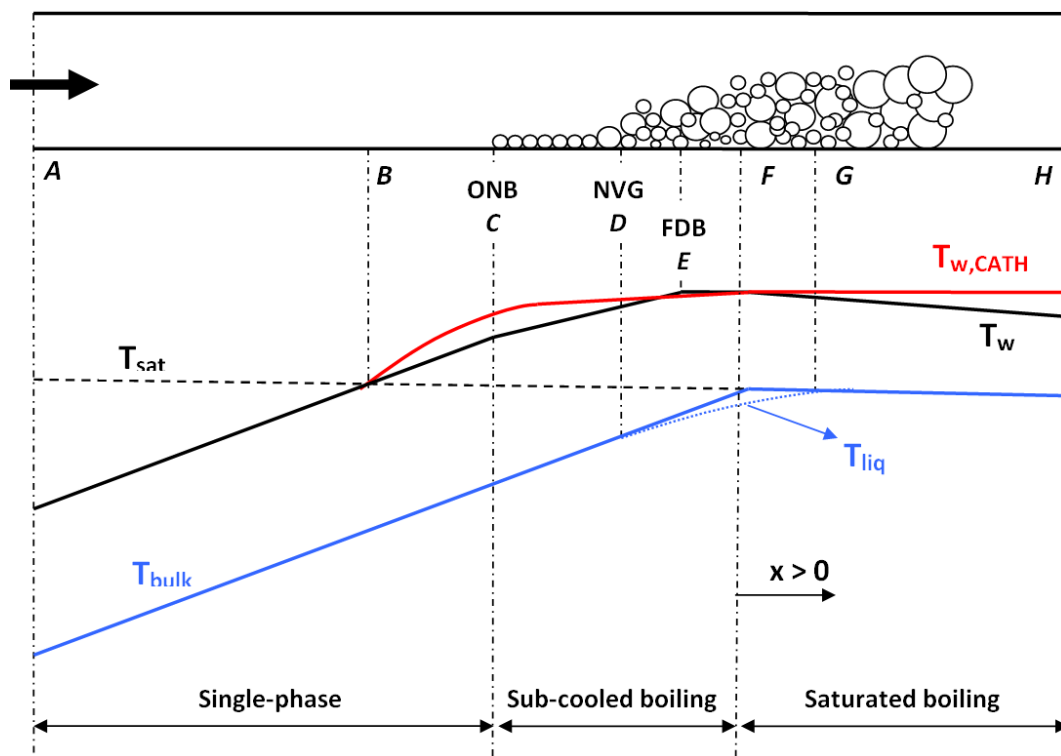


Figure 5.2: Schematic comparison between the flow boiling modeling in the literature [58] and in CATHARE.

The main difference between the two calculation schemes is the lack of an ONB criterion in CATHARE. As a consequence, the single-phase heat transfer is modified when $T_w > T_{sat}$ and an unphysical temperature jump occurs due to the sudden change of the temperature difference, as defined in Eqn. (2.35). This fact leads to a slight over-prediction of the wall temperatures, which is nevertheless conservative.

Analogously, the FDB criterion is not implemented in CATHARE and the flow is assumed to reach FDB conditions when $T_l = T_{sat}$ (i.e. at saturation). These modifications are believed to affect the prediction of the wall temperature in a negligible way. As a matter of fact, in the last part of the sub-cooled region (region E-G in Figure 5.2), the wall-to-liquid heat flux q_{wl} , given by Eqn. (2.57), is small in comparison with the nucleate boiling term q_{nb} . This is caused by the small convective term q_{conv} (proportional to $T_{sat} - T_l$) and by the distribution parameter ϵ very close to 1, as shown in Figure 2.6.

Another approximation in CATHARE is connected to the use of the FDB correlation along the whole saturated boiling region. As discussed above, the nucleate boiling is considered predominant at saturation conditions, and this is acceptable when high heat fluxes are involved. In the other cases, a slight improvement of the heat transfer coefficient, which leads to the prediction of lower wall temperatures, is usually observed. Thus, it is conservative to disregard the forced convective term in saturated boiling.

Based on the previous considerations, the structure of the CATHARE code is believed to be adequate for the two-phase heat transfer modeling in JHR. This is confirmed by the simulations of the SULTAN-JHR tests, which showed that the wet wall temperature profile could be well predicted (if appropriate FDB correlations are used). An example is provided in Figure 5.3. These results are obtained with a version of CATHARE in which the simplified Forster-Greif FDB correlation (5.20) and the single-phase correlations from Section 4.5 were implemented.

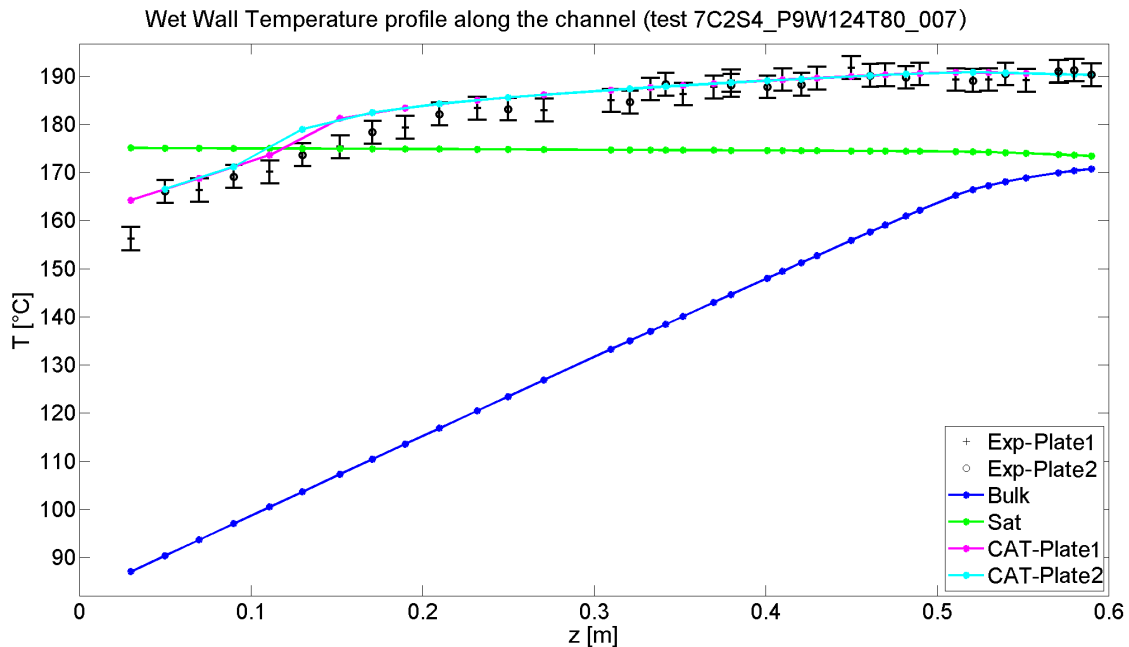


Figure 5.3: Comparison between the experimental and CATHARE wet wall temperature profile.

5.2 Correlations for fully developed boiling heat transfer

In this section, several correlations for fully developed boiling are presented along with their validity ranges and eventual drawbacks. The wall superheat predictions are then compared to the SULTAN-JHR experimental data, so that an appropriate FDB correlation can be suggested for the JHR modeling. All the analyzed data come from the test section SE4, since no measurement in FDB is available for SE3.

The wall superheat is defined as:

$$\Delta T_{sat} = T_w - T_{sat} \quad (5.7)$$

The saturation temperature T_{sat} was estimated with CATHARE, whose single-phase friction and heat transfer correlations were optimized for the simulation of the SULTAN-JHR experiments, as described in Section 4.5. The use of the saturation temperature calculated by CATHARE may be justified by comparing the experimental pressures, measured at the pressure taps P5 and P6, with the predicted values. In fact, the saturation temperature is exclusively dependent on the system pressure and the majority of the experimental points, used in the analysis, are located between P5 and P6. The comparison shows that the residuals between CATHARE and the experimental values have a standard deviation equal to 2.5 % and a bias equal to -0.46 %. This demonstrates that CATHARE can predict accurately the pressure profile (and therefore the saturation temperature) in the analyzed tests.

A careful selection of the experimental database led to the decision of using the data from 32 SE4 tests, where FDB could be clearly identified. Only stable tests were considered, as discussed in Section 3.3.4.

From the 32 experiments, the points of interest were selected in such a manner that the wall superheat is approximately constant along the channel. A total of 227 points was then collected, and they are always found to be beyond the Net Vapor Generation (i.e. $z > z_{NVG}$). In Figure 5.4, the red curve represents the wall temperature predicted by the simplified Forster-Greif correlation as is given in Eqn. (5.20).

The last four thermocouples are removed from the analysis to eliminate any possible effect due to the axial conduction towards the adiabatic zones, consistently with the single-phase selection criteria discussed in Section 4.4.

The range of variation of the physical parameters is reported in Table 5.1.

Table 5.1: Range of physical parameters for the selected FDB points.

Mass flux G [kg/m^2s]	500 - 5364	Liquid subcooling ΔT_{sub} [$^{\circ}C$]	0 - 38.5
Pressure p [MPa]	0.23 - 0.90	Heat flux ϕ [MW/m^2]	0.46 - 4.41
Steam quality x	-0.08 - 0.08	Void fraction α	0 - 0.906

In this table, the steam quality is calculated as:

$$x(z) = \frac{i(z) - i_{l,sat}}{i_{lg}} \quad (5.8)$$

where $i(z)$ indicates the enthalpy of the fluid based on an heat balance. The void fraction values are estimated with CATHARE.

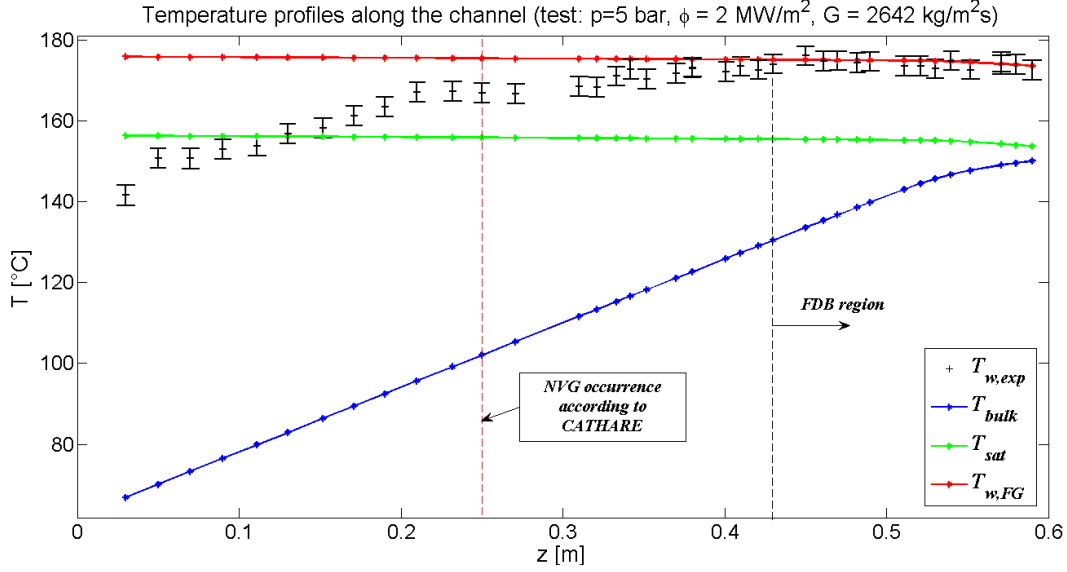


Figure 5.4: Determination of the FDB region according to the experimental temperature profile.

In the following sections, the selected points are then compared to several FDB correlations.

5.2.1 Jens-Lottes and Thom correlations

The Jens-Lottes and Thom correlations are standard correlations employed in the modeling of conventional nuclear reactors and boilers [58].

Jens-Lottes correlation [67] was developed using experiments with water in vertical tubes of small diameters (i.e. 3.63, 4.57 and 5.7 mm) electrically heated. The experiments were performed at UCLA, MIT and Purdue universities. The mass fluxes were between 11 and $10.4 \cdot 10^3 \frac{kg}{m^2s}$, the pressures between 0.59 and 17.24 MPa, and heat fluxes between 0.8 and $7.8 MW/m^2$. The correlation reads:

$$\Delta T_{sat} = 25 \left(\frac{\phi}{10^6} \right)^{0.25} e^{\left(-\frac{1}{62} \frac{p}{10^5} \right)} \quad (5.9)$$

Thom correlation [18] is a modification of the Jens-Lottes correlation which was obtained from experimental data in a tube of internal diameter equal to 12.7 mm. The correlation is valid only for water, flowing upwardly with velocities between 1.5 and 6.1 m/s, pressures between 5.17 and 13.78 MPa, and heat fluxes between 0.284 and $1.58 MW/m^2$. Thom observed that the Jens-Lottes correlation may under-estimate the wall superheat and suggested an improved version:

$$\Delta T_{sat} = 22.65 \left(\frac{\phi}{10^6} \right)^{0.5} e^{\left(-\frac{1}{87} \frac{p}{10^5} \right)} \quad (5.10)$$

Thom correlation is the standard model for the prediction of the wall superheat in CATHARE.

Figure 5.5 shows that these correlations significantly under-predict the heat transfer in FDB and lead to higher wall superheat in comparison with the experiments.

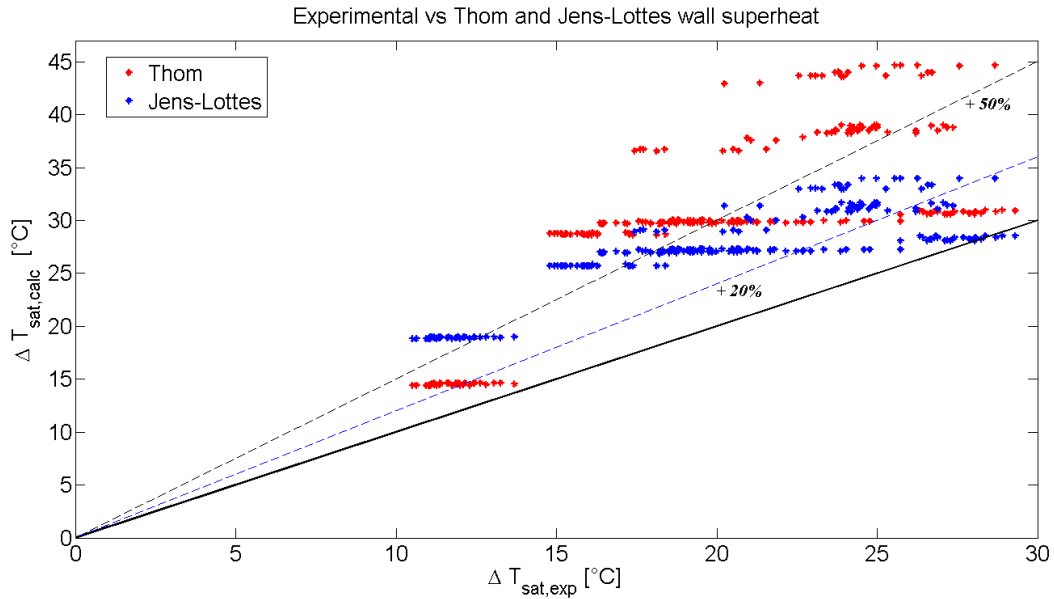


Figure 5.5: Comparison of the experimental data with the prediction of Jens-Lottes and Thom correlation.

The reason of this poor performance may be that both the correlations were developed for relatively high pressure applications, while the SULTAN-JHR experiments are at lower pressure (0.2 to 0.9 MPa). Therefore their use for the JHR modeling is discouraged.

5.2.2 Qiu correlation

Qiu correlation [68] was developed for vertical narrow annuli, using experimental data obtained from two tests sections with gaps of 1.0 and 1.5 mm. It was observed that the boiling heat transfer is enhanced due to the restricted growth and flow of bubbles in the narrow channel. This kind of phenomenon was also pointed out in other works, e.g. [69]. Furthermore it was claimed that a decrease of the channel gap may lead to a decrease of the wall superheat, indicating an improvement of the two-phase boiling heat transfer coefficient with a smaller gap. The authors suggested a modified version of the Jens-Lottes correlation:

$$\Delta T_{sat} = A \left(\frac{\phi}{10^6} \right)^{0.25} e^{\left(-\frac{1}{62} \frac{p}{10^5} \right)} \quad (5.11)$$

The pressure and the heat flux coefficients were kept constant while the multiplicative factor A was obtained with a best-fit, as shown in Table 5.2.

Table 5.2: The coefficient A in Qiu correlation (5.11) as a function of the gap size.

Gap size [mm]	A
1.0	6.081
1.5	7.240
Jens-Lottes	25

In order to apply this correlation to the SULTAN-JHR modeling, the coefficient $A = 8.77$ was computed with a linear extrapolation.

It was observed that Qiu correlation strongly under-predict the wall superheat, as shown in Figure 5.6.

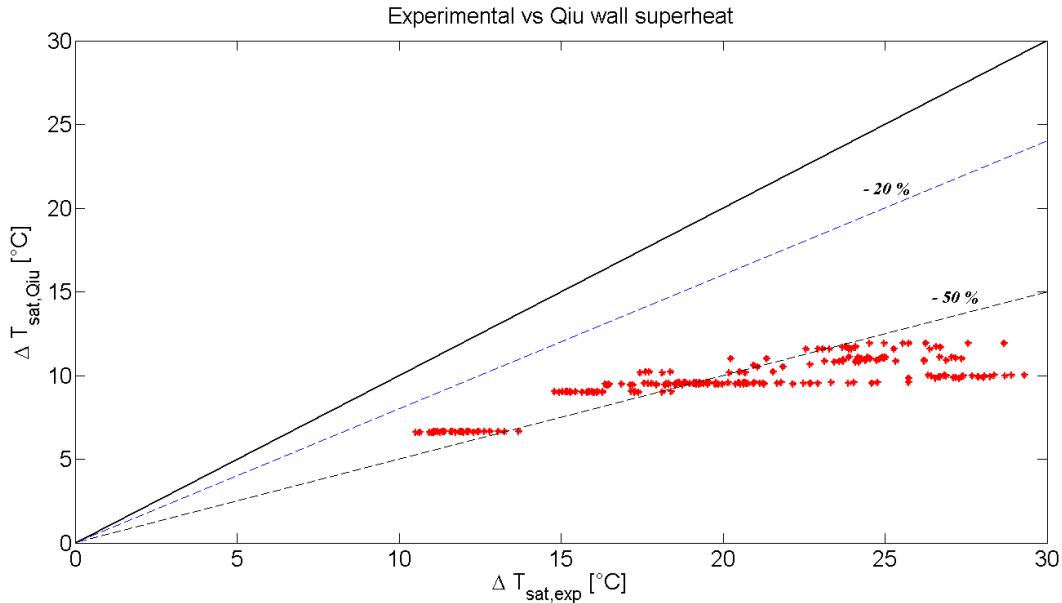


Figure 5.6: Comparison of the experimental data with the prediction of Qiu correlation.

The under-prediction may be due to the fact that the correlation is not used within its range of validity. In fact, the correlation was developed with experiments at higher pressures (1.2 - 4.0 MPa) and very low heat fluxes ($< 0.1 \text{ MW}/\text{m}^2$).

These low heat fluxes determined low wall superheat (2 - 4 $^{\circ}\text{C}$) that seems to be comparable with the experimental uncertainties. Therefore the correlation may also be affected by this issue.

5.2.3 Belhadj correlation

Belhadj et al. [69] studied the wall superheat under fully developed nucleate boiling in vertical, narrow rectangular channels with gap sizes of 2.0, 3.0 and 4.0 mm. The experimental study focused on upward flows at low velocities ($< 0.15 \text{ m/s}$), low heat fluxes ($< 0.12 \text{ MW}/\text{m}^2$), and low pressures (0.139 - 0.145 MPa). The boiling phenomena was investigated in natural convection conditions that are typical of accidental transients in plate-type research reactors.

The authors showed that the conventional correlations for fully developed nucleate boiling (e.g. Jens-Lottes and Thom correlations) overestimate the wall superheat when compared to their experimental data. The heat transfer enhancement was explained with the influence of the narrow gap: the bubbles growing on the two opposite walls can touch each others, thus the rate of bubble detachment from the walls is increased. This effect was taken into account in a correlation that includes the gap size e_{ch} and the bubble diameter D_b via a dimensionless number.

The final correlation was obtained from a best-fit of the experimental data that gives:

$$\Delta T_{sat} = 0.484 (\phi)^{0.25} \left(\frac{e_{ch} - 1.13D_b}{e_{ch}} \right)^{0.26} \quad (5.12)$$

where the bubble diameter is calculated as:

$$D_b = 1.5 \times 10^{-4} \left[\frac{\sigma}{g(\rho_l - \rho_g)} \right]^{0.5} \left(\frac{\rho_l c_{pl} T_{sat}}{\rho_g h_{lg}} \right)^{5/4} \quad (5.13)$$

The vapor tension and the steam properties are calculated at saturation and the saturation temperature T_{sat} is expressed in Kelvin.

In case of the SULTAN-JHR experiments, this correlation provides reasonable results at low wall superheat, but it cannot predict many experimental points, as shown in Figure 5.7.

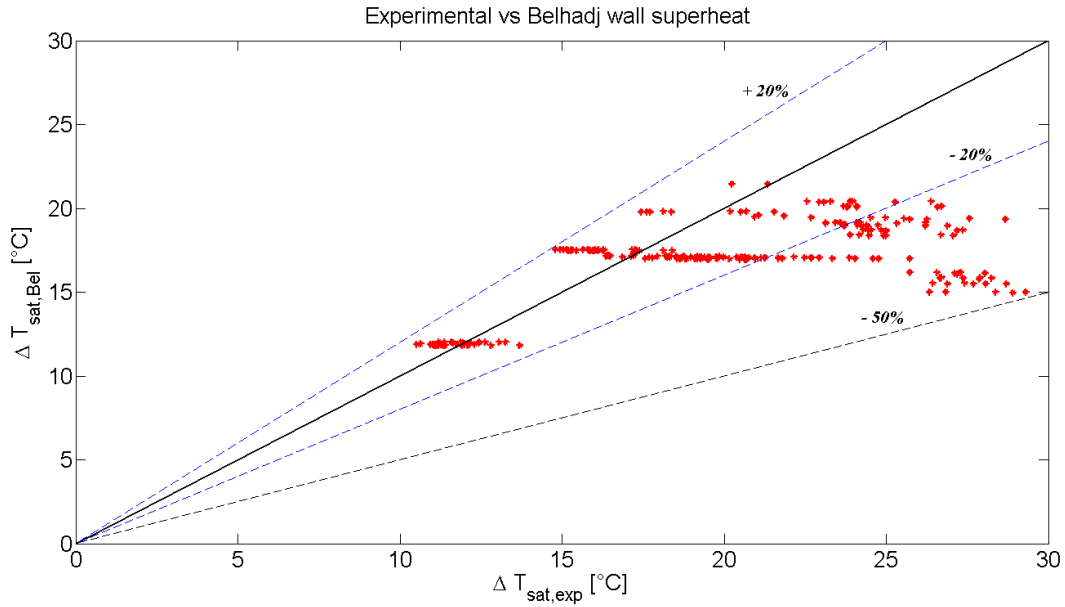


Figure 5.7: Comparison of the experimental data with Belhadj correlation.

It should be noticed that Belhadj correlation is the only correlation of the reviewed ones which fails to predict the dependency of the wall superheat from the pressure, as shown in Figure 5.8. The reason for this may be that the experimental range of pressure variation is quite limited (between 0.139 and 0.145 MPa). In addition, the accuracy of the correlation may be affected by the use of low heat fluxes, as discussed for Qiu correlation.

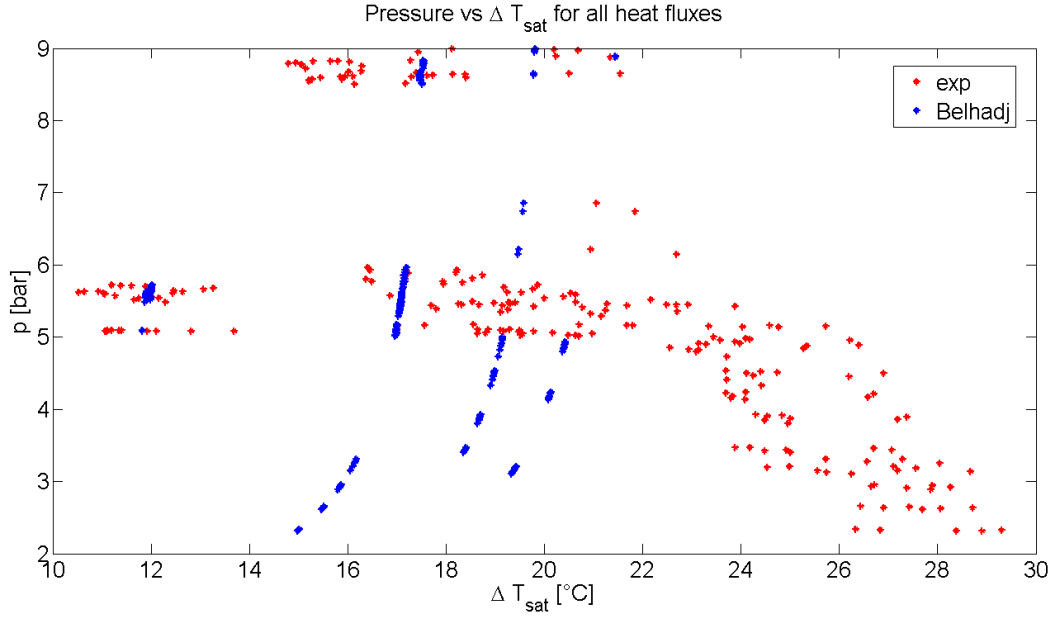


Figure 5.8: Pressure dependency of Belhadj correlation compared with experiments.

5.2.4 Gorenflo correlation

The Gorenflo correlation was developed for water pool boiling at pressure between 0.022 and 2.2 MPa [70]. The predictive model is based on a reference heat transfer coefficient $h_0 = 5600 \frac{W}{m^2 \cdot ^\circ C}$, obtained with a surface roughness $R_{p0} = 0.4 \mu m$, a heat flux $\phi_0 = 20000 \frac{W}{m^2}$ and a reduced pressure $P_{r0} = 0.1$. The reduced pressure is defined as $P_r = \frac{p}{p_{crit}}$, where the critical pressure for water is equal to 22.064 MPa.

The correlation is written in term of normalized quantities as:

$$h_{PB} = h_0 F_P \left(\frac{\phi}{\phi_0} \right)^n \left(\frac{R_p}{R_{p0}} \right)^{0.133} \quad (5.14)$$

where the coefficients n and F_P are derived for water as [70]:

$$n = 0.9 - 0.3 P_r^{0.15} \quad (5.15)$$

$$F_P = 1.73 P_r^{0.27} + \left(6.1 + \frac{0.68}{1 - P_r} \right) P_r^2 \quad (5.16)$$

The surface roughness is usually set to $0.4 \mu m$ if the properties of the surfaces are unknown, as suggested in [58] and [6]. This correlation is used in the system code TRACE for the modeling of the nucleate boiling heat transfer component in flow boiling [6]. The use of this closure law in system codes was however criticized in [71], because the surface roughness is usually unknown and its modeling can be very difficult.

The use of this correlation provides a good comparison with the experiments, as shown in Figure 5.9.

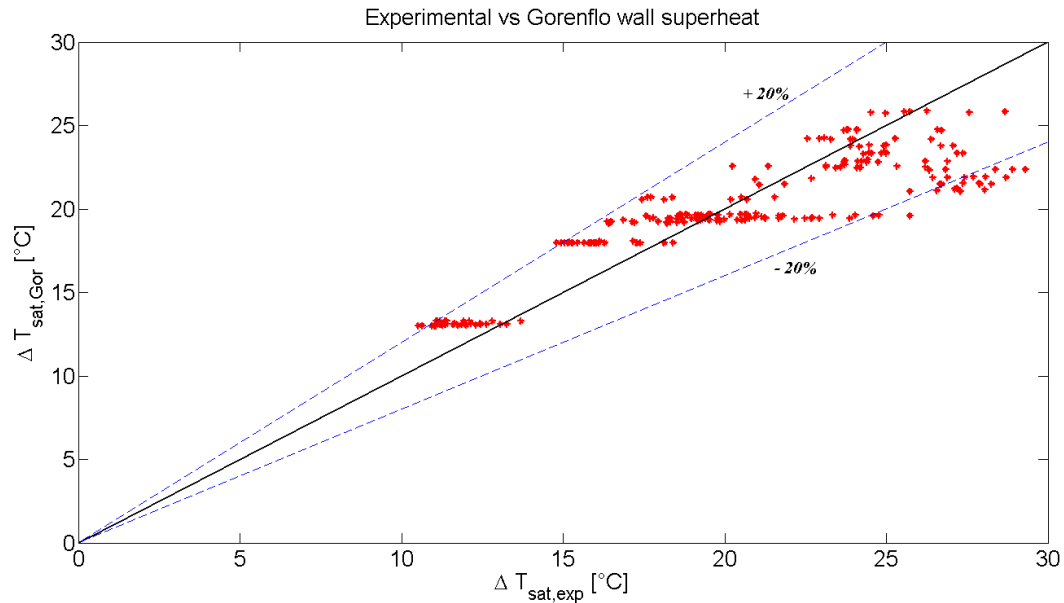


Figure 5.9: Comparison of the experimental data with the prediction of Gorenflo correlation.

The standard deviation of the residuals is equal to 11.9 % and the bias is equal to 0.01 %. The residuals are computed as:

$$Residual [\%] = 100 \frac{\Delta T_{sat,calc} - \Delta T_{sat,exp}}{\Delta T_{sat,exp}} \quad (5.17)$$

Their distribution is shown in Figures 5.10 and 5.11. The deviations from normality may be explained by the relatively small number of tests available.

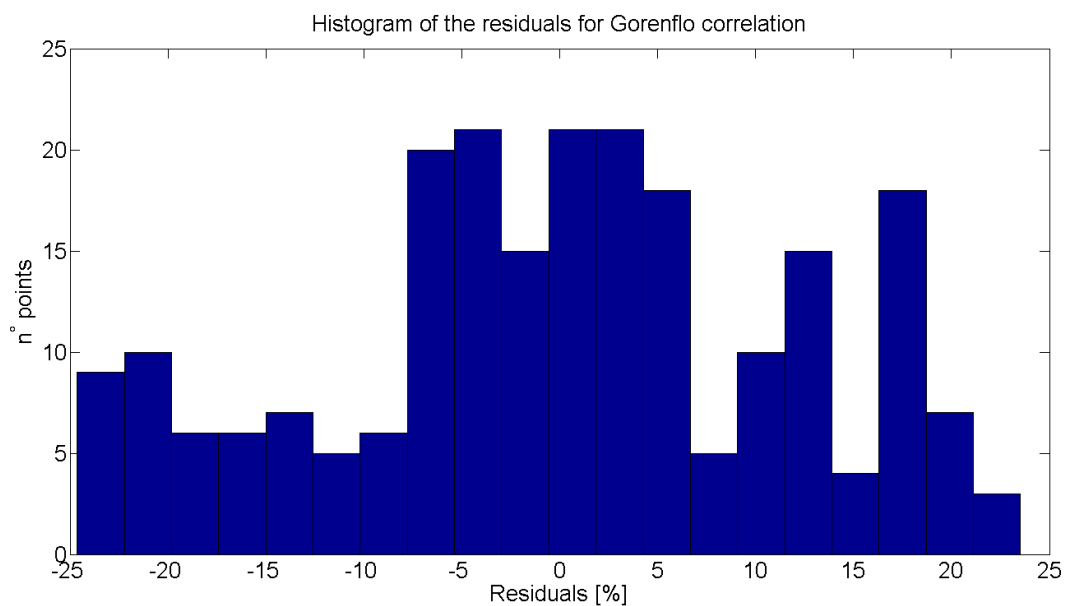


Figure 5.10: Histogram of the residuals for Gorenflo correlation.

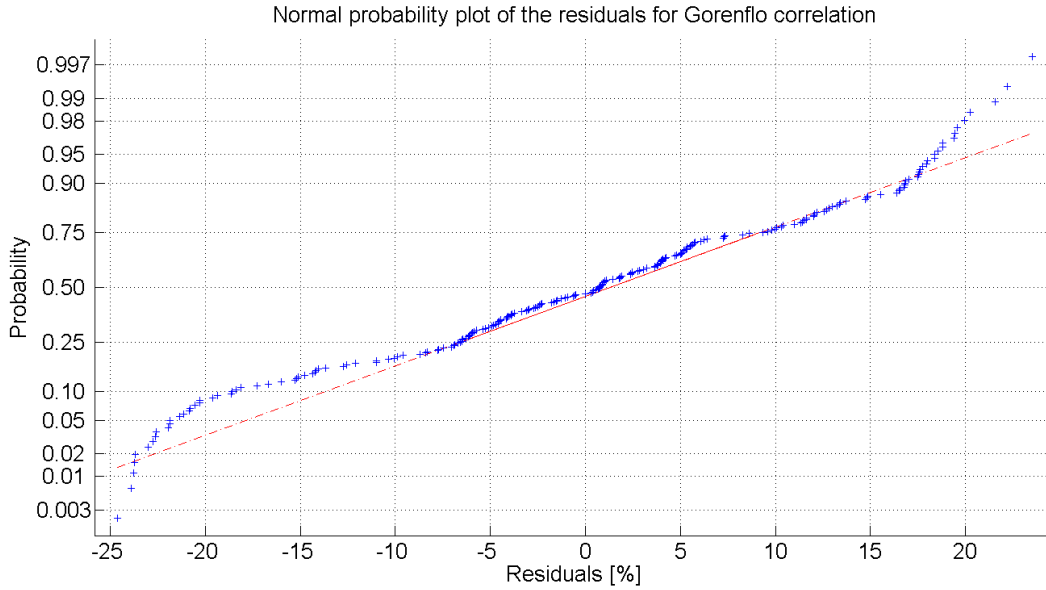


Figure 5.11: Normal probability plot of the residuals for Gorenflo correlation.

5.2.5 Forster-Greif correlation

The Forster-Greif correlation is used for prediction of the heat transfer in sub-cooled flow boiling of water, especially at low pressure. It has been employed in the thermal-hydraulic modeling for research reactors with fuel flat plates, such as the PLTEMP-ANL code [72] and the one reported in [73]. Different versions can be found in the literature and a short review of them is presented below.

The original Forster-Greif correlation [74]

The original Forster-Greif correlation [74] is based mainly on theoretical considerations and a quite small set of experimental data for water at 1 and 5 atm. The correlation was theoretically developed from a dimensional analysis. The majority of the unknown quantities were derived from hypotheses and physical considerations. The suggested form reads:

$$\phi = C_I \frac{k_l}{2\sigma} \Delta p_{sat} \Delta T_{sat} Pr^{1/3} \Pi_1^{0.2} \quad (5.18)$$

The dimensionless number Π_1 describes the growth of a vapor bubble and it is written as:

$$\Pi_1 = \frac{c_{pl}^2 \rho_l^3}{\mu_l} \frac{\pi a_l}{i_{lg}^4 \rho_g^4} \Delta p_{sat}^2 T_{sat}^2 = \frac{\pi c_{pl} \rho_l^2 k_l}{\mu_l i_{lg}^4 \rho_g^4} \Delta p_{sat}^2 T_{sat}^2 \quad (5.19)$$

where $a_l = \frac{k_l}{c_{pl} \rho_l}$ is the liquid thermal diffusivity and the vapor density ρ_g is computed at saturation. The quantity Δp_{sat} is the difference in saturation pressure corresponding to the wall superheat ΔT_{sat} . It can be read from the vapor pressure curve or calculated as $\Delta p_{sat} = p_{sat}(T_w) - p_{sat}(T_l)$ [58]. It must be stressed that Eqn (5.19) requires the quantities in consistent British units and T_{sat} must be expressed in $^{\circ}F$.

The coefficient C_I is equal to 0.7×10^{-2} and was determined by fitting one experiment conducted for water pool boiling, at atmospheric pressure. The accuracy of this value was verified with additional measurements at 50 atm. No reference was reported about the origin of the experimental data. Nevertheless, from the figures in [74], it is possible to deduce an heat flux validity range between 0.16 and 6.3 MW/m^2 . Bergles [75] observed that this correlation was developed for pool boiling, but it may be also applicable to flow boiling.

This correlation is complicated to use and to implement in a system code, such as CATHARE. In view of this, simplified formulations were developed.

A simplified version of the Forster-Greif correlation

This simplified correlation is usually reported in the literature (e.g. [72], [73] and [57]) as the correlation of Forster-Greif. The correlation reads:

$$\Delta T_{sat} = 4.57 \left(\frac{p}{10^5} \right)^{-0.23} \left(\frac{\phi}{10^4} \right)^{0.35} \quad (5.20)$$

The exclusive dependency of the wall superheat on the system pressure and the imposed heat flux (i.e. known quantities) makes this correlation very simple to use and implement in system codes. No original reference could be identified for this relationship. The first documented application is in an internal CEA report on the preliminary safety analysis of the research reactor OSIRIS (1963). In this report, the correlation is reported as the correlation of Forster-Greif simplified and approximated for water between 0.1 and 5.0 MPa. This can be verified from the data available in Figure 9 of Forster-Greif's paper [74]. In particular, one may observe that the wall superheat is proportional to the heat flux raised to approximately 0.34 for the data at 0.1 MPa, and 0.42 at 5.0 MPa. Therefore, if an average pressure of 8 bar is assumed, one may obtain an exponent approximately equal to 0.35, as in Eqn. (5.20). Furthermore, this simplified form of the correlation predicts relatively well Forster-Greif's experimental points.

In the paper written by Ricque-Siboul [57], it is reported that the correlation was developed at CEA-Grenoble based on experimental data at low pressures (between 0.1 and 0.8 MPa). Unfortunately, the name of the test loop, the channel geometry and the flow conditions were not documented and could not be found in any other available source.

From the extensive literature review it may be concluded that this correlation was developed at CEA-Grenoble before 1963 and it is based on the work of Forster-Greif [74]. The correlation is valid for pressures between 0.1 and 0.8 MPa, but the range might be extended up to 5.0 MPa.

The validity of this correlation was also verified for subcooled fully developed nucleate boiling in small-diameter tubes (between 2 and 4 mm), at high heat fluxes (between 5.6 and 20.5 MW/m^2), and low pressures (approximately between 1.3 and 5.0 bar) [57].

The comparison with the experimental data from the SULTAN-JHR database gives excellent results, as shown in Figure 5.12. The standard deviation of the residuals is equal to 10.1 % and the bias is equal to 1.32 %. The distribution of the residuals is shown in Figure 5.13 and 5.14.

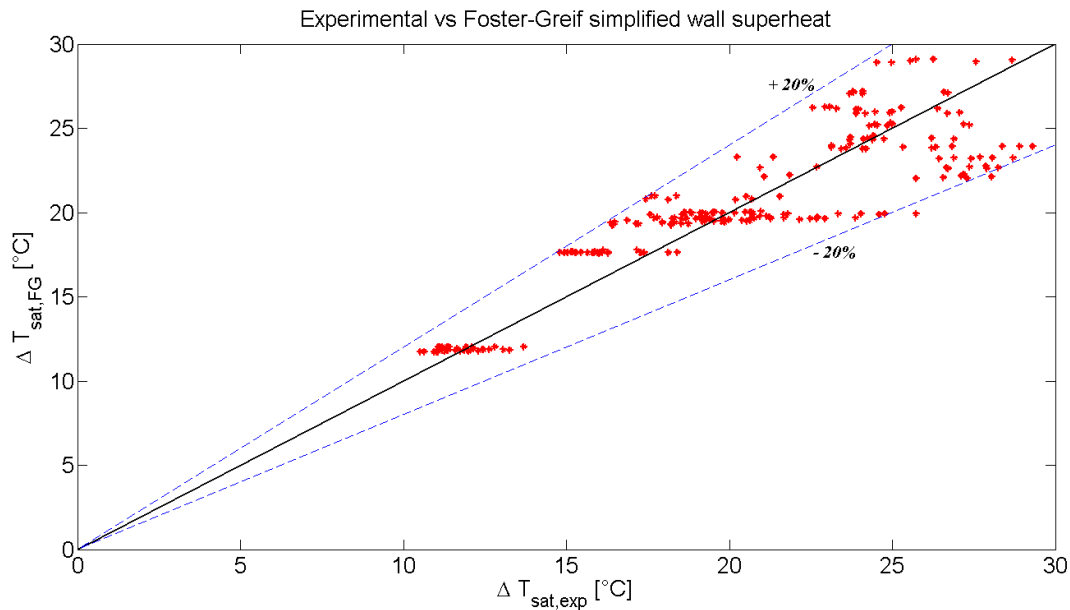


Figure 5.12: Comparison of the experimental data with the prediction of the simplified Forster-Greif correlation.

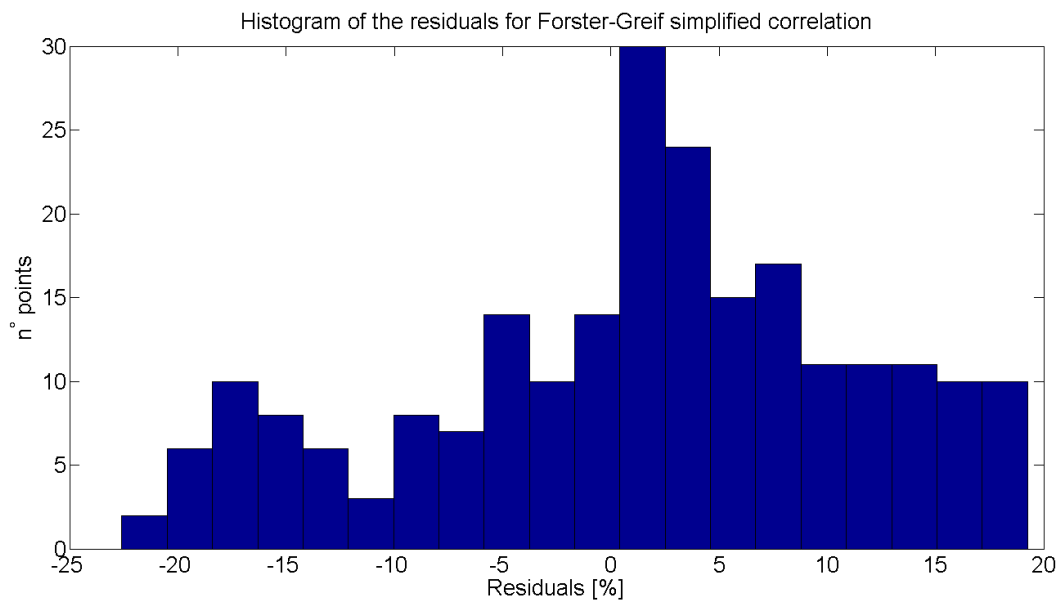


Figure 5.13: Histogram of the residuals for the simplified Forster-Greif correlation.

The largest discrepancies between experiments and predictions are observed at low pressures (0.2 - 0.4 MPa) and low heat fluxes ($\approx 0.5 \text{ MW/m}^2$), as shown in Figure 5.15.

This effect is expected at low pressure because it is more difficult to stabilize boiling phenomena, and because larger uncertainties are associated to the estimation of the saturation temperature. This group of tests causes also the small bump in Figures 5.13 and 5.14 for the residuals around -18 %.

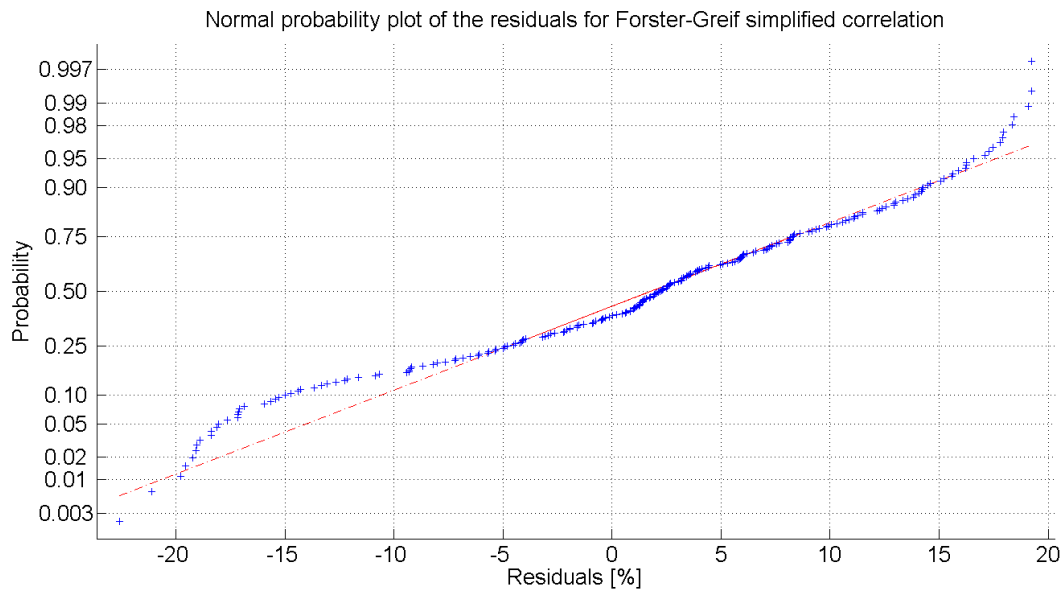


Figure 5.14: Normal probability plot of the residuals for the simplified Forster-Greif correlation.

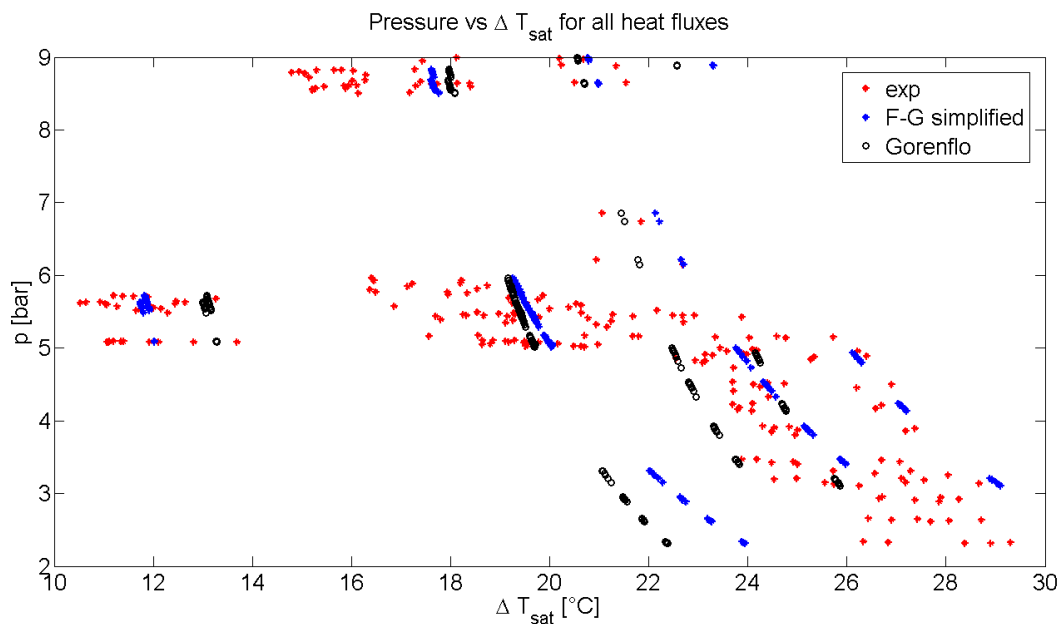


Figure 5.15: Pressure dependency of the simplified Forster-Greif and Gorenflo correlation compared with the experimental results.

The Forster-Greif correlation according to Fabrega [76]

This correlation is quite similar to the previous simplified correlation, but the fitting coefficients are slightly different. It reads:

$$\Delta T_{sat} = 4.44 \left(\frac{p}{10^5} \right)^{-0.23} \left(\frac{\phi}{10^4} \right)^{0.385} \quad (5.21)$$

This correlation was obtained from experiments carried out in the CF4 test loop at CEA-Grenoble, and it was developed by Fabrega [76]. The test section consisted of a circular tube of internal diameter equal to 6 mm, and it was operated at a pressure of approximately 0.8 MPa. The measurements were in conditions of upward flow boiling. No clear validity range for the correlation is given.

For the SULTAN-JHR experiments, Eqn. (5.21) predicts higher wall superheat if compared to Eqn. (5.20) and provides poorer performances as shown in Figure 5.16.

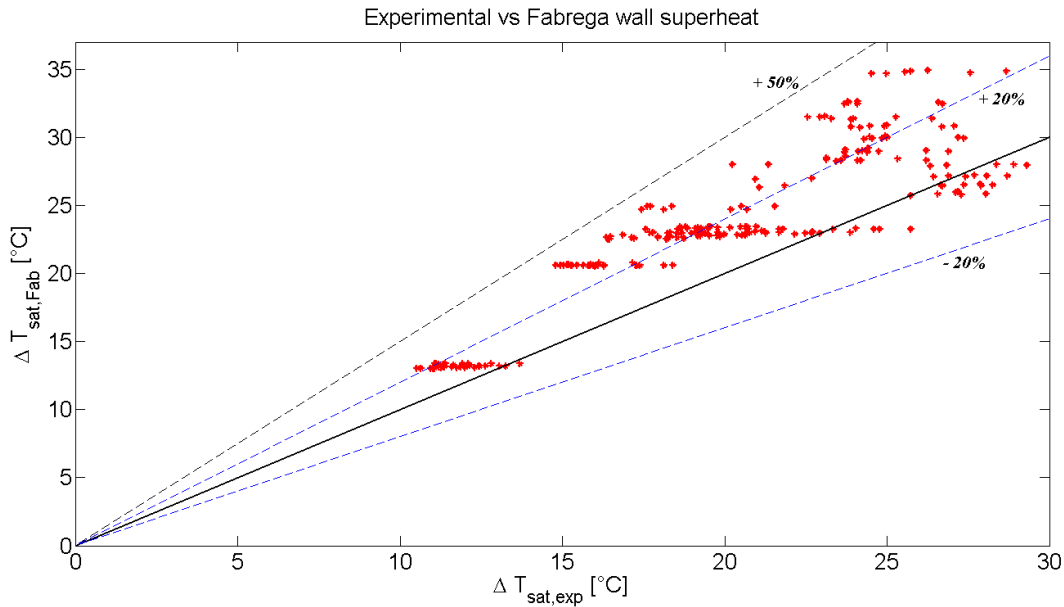


Figure 5.16: Comparison of the experimental data with Fabrega correlation.

5.3 Summary and suggested modifications

CATHARE algorithm for the heat transfer modeling was assessed. A modified Bowring model, which guarantees the continuity of the calculated parameters, is implemented in CATHARE.

The main drawback of such an algorithm is the lack of an ONB criterion, which may lead to over-predictions of the wall temperature in the first part of the sub-cooled boiling region. These over-predictions are expected to be small and conservative. The introduction of an ONB criterion in CATHARE would require a major restructuring of the code, which is not worthy in view of the possible small advantages compared to the increased complexity of the code.

The good agreement between experimental data and calculations on the axial profile of the wall temperature, confirms that CATHARE is adequate for the two-phase heat transfer modeling of JHR.

The assessment of the FDB heat transfer shows that the correlations of Jens-Lottes, Thom, Belhadj, Qiu and Fabrega cannot accurately predict the experimental data. On the other hand, the formulation of Gorenflo and Forster-Greif simplified provide good results. A summary of the statistical analysis of the residuals associated to the different correlations is reported in Table 5.3.

Table 5.3: Summary of the analysis of the FDB correlations.

Correlation	2σ [%]	Bias [%]	95 per. [%]	Min-Max [%]
Jens-Lottes (5.9)	39.3	38.97	0.67 - 71.44	-2.63 - 78.69
Thom (5.10)	50.7	52.82	9.08 - 101.0	5.64 - 112.2
Qiu (5.11)	13.8	-51.24	-64.68 - -39.84	-65.84 - -37.30
Belhadj (5.12)	32.1	-12.89	-44.12 - 14.83	-48.83 - 18.60
Gorenflo (5.14)	23.8	0.01	-22.97 - 19.56	-24.63 - 23.53
Forster-Greif (5.20)	20.2	1.32	-19.07 - 17.94	-22.58 - 19.25
Fabrega (5.21)	24.9	18.41	-5.41 - 39.29	-9.51 - 41.78

For the modeling of the JHR, it is therefore suggested the use of the simplified Forster-Greif correlation in the form of Eqn. (5.20), which provides the best performances.

The simplified Forster-Greif formula also has two attractive features: first, its implementation is straightforward; second, it is independent from the surface conditions and roughness (that may not be accurately known for complex systems, such as a reactor core).

The simplified Forster-Greif correlation has thus been introduced in CATHARE. All the stable SULTAN-JHR tests with sub-cooled and saturated boiling were simulated with this new version of the code. The single-phase heat transfer region was excluded and the point after the occurrence of the NVG (as calculated by CATHARE) were collected. The last 8 thermocouples (i.e. the last 10 cm of the heated channel) were disregarded in order to eliminate any possible effect due to the axial conduction towards the adiabatic zones.

Based on these criteria, a total number of 719 points from 80 SE4 tests was obtained. Figure 5.17 shows that the improved CATHARE can predict accurately the wet wall temperature in the whole flow boiling region.

The residuals between experimental and CATHARE are evaluated as:

$$Residual [\%] = 100 \frac{T_{w,exp} - T_{w,calc}}{T_{w,exp}} \quad (5.22)$$

The standard deviation is equal to 2 %, the bias is equal to - 0.7 % and 95 % of the points is found between -4.8 % and 3.81 %. Details on the distribution of the residuals is given in Figure 5.18.

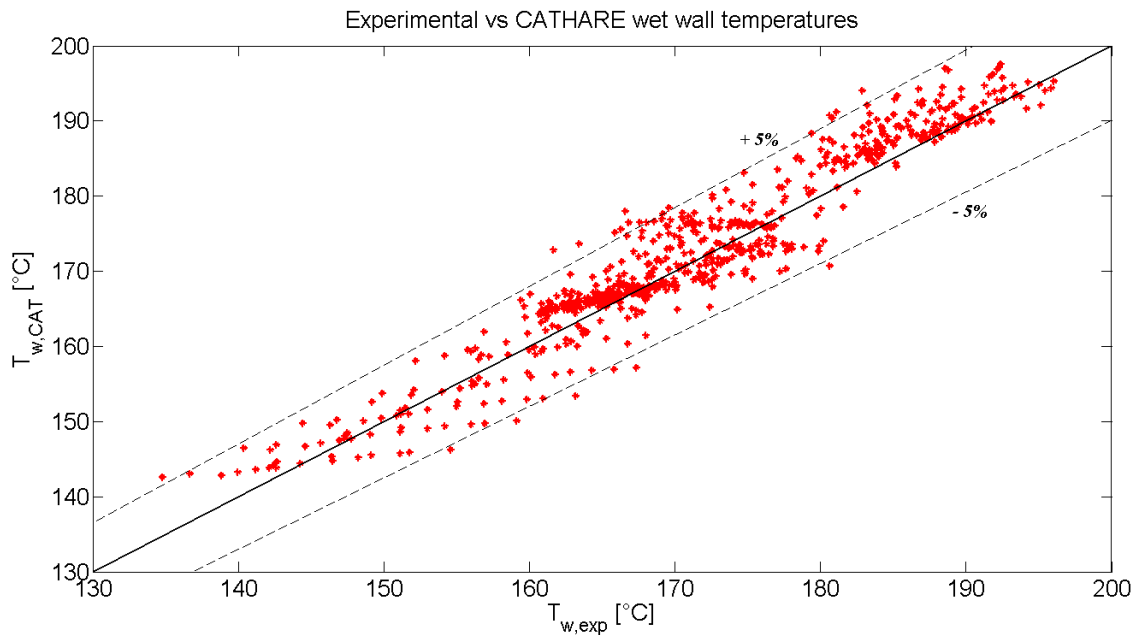


Figure 5.17: Comparison of the experimental data with the improved CATHARE predictions using Forster-Greif correlation (5.20).

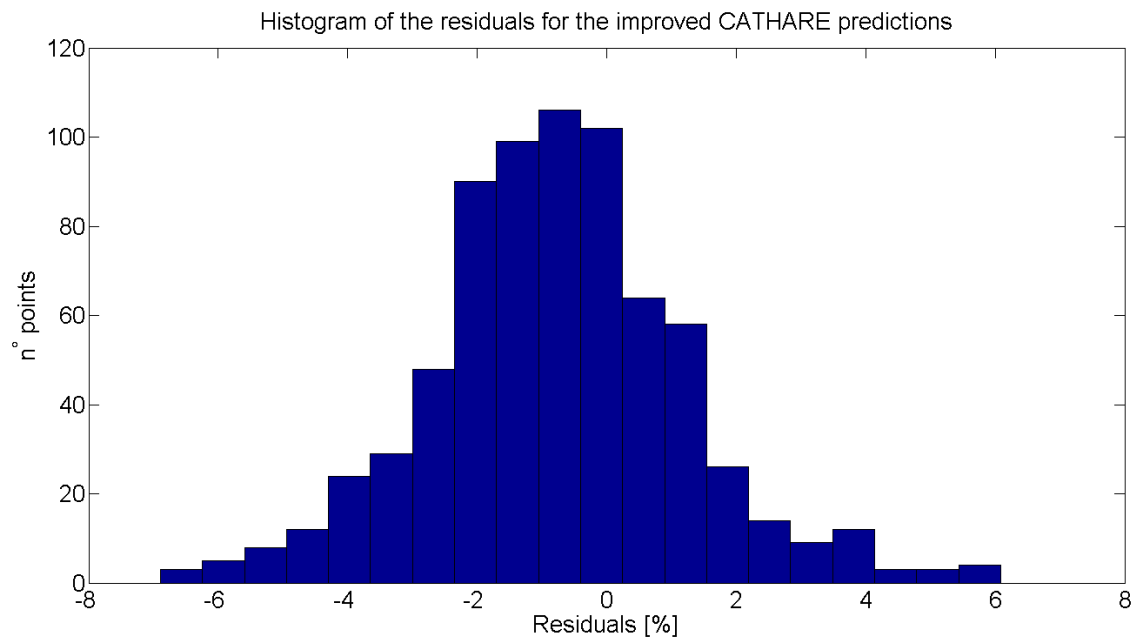


Figure 5.18: Histogram of the residuals for the improved CATHARE predictions using Forster-Greif correlation (5.20).

Chapter 6

Conclusions and future work

6.1 Summary of the main results

The modeling capabilities of the system code CATHARE were assessed with respect to conditions that can be considered representative of the Jules Horowitz Reactor. The SULTAN-JHR experimental database was used for the evaluation of relevant correlations both in single and two-phase flow. The data are related to two narrow vertical rectangular channels with gap sizes of 1.51 mm (SE3) and 2.16 mm (SE4). The experimental conditions range between: 0.2 and 0.9 MPa for the pressure; 0.5 and 18 m/s for the coolant velocity; and 0.5 and 7.5 MW/m² for the heat flux.

The analysis includes the assessment of correlations for single-phase friction, turbulent single-phase heat transfer and heat transfer in fully developed boiling.

As regards single-phase flow, it is suggested that a more realistic modeling of the laminar-turbulent transition could be introduced in CATHARE (see Section 4.1). Thus, a transition range with Reynolds number between 2500 and 4000 was implemented in the code.

The investigation of the isothermal tests allowed the selection of appropriate isothermal friction correlations. In the laminar region ($Re < 2500$), the Shah-London correlation was found to be appropriate. The Noel correlation, optimized over the SULTAN-JHR experiments, was used in the turbulent region ($Re > 4000$). In the transition region ($2500 < Re < 4000$), a linear interpolation between the laminar and the turbulent correlation was suggested for continuity and simplicity.

A corrective factor F_{cor} (4.12) was added, in case of heated walls.

The single-phase heat transfer coefficient was then analyzed. The Marco and Han correlation was suggested for the single-phase heat modeling in laminar flows. A linear interpolation between the laminar and the turbulent correlation was again implemented in the transition region.

The evaluation of the turbulent heat transfer coefficient showed that the standard correlations (e.g. Dittus-Boelter) significantly under-estimate the heat transfer, especially at high Reynolds numbers (see Section 4.4.1). Thus, improved correlations were developed from the SULTAN-JHR experimental data (see Section 4.4.2).

It was also observed that the geometry of the narrow rectangular channel may significantly affect the turbulent heat transfer (see Section 4.4.3). In particular, a

reduction of the channel gap leads to an improvement of the heat transfer coefficient.

In the second part of the work, the modeling of the two-phase heat transfer in CATHARE was scrutinized. This was found to be adequate for the JHR applications.

Several correlations for fully developed boiling were assessed against the available SULTAN-JHR experimental data (see Section 5.2). The simplified Forster-Greif correlation given by Eqn. (5.20) is recommended because of its performance (the standard deviation of the residuals was found equal to 10.1 %) and its simplicity.

6.2 Future work

Future work will be addressed to study additional aspects of the thermal-hydraulic modeling of JHR. This includes the criterion of Net Vapor Generation, the correlations for Critical Heat Flux, and the simulation of flow redistribution, which are related to key safety issues in a nuclear reactor.

Sensibility and uncertainty analysis will also be performed in order to identify the importance of the several modeling parameters and to quantify the accuracy of the correlations.

The improved version of CATHARE will be finally applied to transient analysis of JHR. The impact of the uncertainties on these simulations will be also evaluated.

Acknowledgments

I would like to thank all the people who contributed to the completion of the licentiate work.

My gratitude goes especially to my supervisors Dr. Brigitte Noel and Prof. Paolo Vinai for their continuous scientific and moral support, guidance and supervision. The fruitful and pleasant discussions, the comments and the suggestions were of great help for overcoming the encountered difficulties and to improve the quality of the work. I have really appreciated the respectful and encouraging attitude towards me, the good company and the nice working environment.

I am also very grateful to Prof. Christophe Demazière for his important contribution to the coordination of the project and the helpful comments and feedbacks on the research work and to Prof. Imre Pazsit for being my examiner.

I would also like to thank the JHR team and CEA-Grenoble for their cooperation and support to the project.

Many thanks go to my colleagues both at Chalmers and at CEA-Grenoble for creating a pleasant working environment. A special gratitude goes to Marc Parent for his support with CATHARE and to Didier Dumont for his helpfulness and kindness.

The financial support of the Swedish Research Council (Vetenskapsrådet) is gratefully acknowledged.

Last but not least, I would like to express my gratitude to my family which has been supporting and encouraging me during my entire life.

Bibliography

- [1] D. Iracane et al. The JHR, a new material testing reactor in Europe. *Nuclear Engineering and Technology*, 38:437–442, 2006.
- [2] M. Boyard et al. The Jules Horowitz Reactor core and cooling system design. In *IGORR 10*, Gaithersburg, USA, Sept. 2005.
- [3] R. Pegonen S. Bourdon, C. Gonnier and H. Anglart. A review of the current thermal-hydraulic modeling of the Jules Horowitz Reactor: A loss of flow accident analysis. *Nuclear Engineering and Design*, 280:294–304, 2014.
- [4] F. Cochemé. Use of the thermalhydraulics code CATHARE for the Jules Horowitz Reactor safety assessment. In *International Conference on Research Reactors: Safe Management and Effective Utilization*, Rabat, Morocco, Nov. 14-18 2011.
- [5] F. Barre and M. Bernard. The CATHARE code strategy and assessment. *Nuclear Engineering and Design*, 124:257–284, 1990.
- [6] U.S. Nuclear Regulatory Commission. TRACE V5.0 Theory Manual: Field Equations, Solution Methods and Physical Models. Technical report.
- [7] G. Geffraye et al. CATHARE 2 V2.5_2: A single version for various applications. *Nuclear Engineering and Design*, 241:4456–4463, 2011.
- [8] M. Ishii and T. Hibiki. *Thermo-Fluid Dynamics of Two-Phase Flow*. Springer, 2011.
- [9] J. H. Ferziger and M. Perić. *Computational methods for fluid dynamics*. Springer, 2002.
- [10] D. Bestion. The phase appearance and disappearance in the CATHARE code. In *Trends in Numerical and Physical Modeling for Industrial Multiphase Flows*, Cargese, France, Sept. 27-29 2000.
- [11] G. Laviaille. General description of the CATHARE 2 V25_2mod8.1 system code. Technical report, 2012.
- [12] D. Bestion. The physical closure laws in the CATHARE code. *Nuclear Engineering and Design*, 124(3):229–245, 1990.
- [13] M. M. Shah. A general correlation for heat transfer during film condensation inside pipes. *International Journal of Heat and Mass Transfer*, 22:547–556, 1979.

- [14] S. Nukiyama. The maximum and minimum values of the heat Q transmitted from metal to boiling water under atmospheric pressure. *International Journal of Heat and Mass Transfer*, 9:1419–1433, 1966.
- [15] Y. A. Çengel. *Heat Transfer: a practical approach*. Mcgraw-Hill, 2nd edition, 2002.
- [16] S. Kakaç et al. *Handbook of single-phase convective heat transfer*. John Wiley and Sons, 1987.
- [17] F. W. Dittus and L. M. K. Boelter. Heat transfer in automobile radiators of the tubular type. *University of California Publications in Engineering*, 2:3–22, 1930.
- [18] J. R. S. Thom et al. Boiling in subcooled water during flow up heated tubes or annuli. In *Proceedings of Symposium on Boiling Heat Transfer in Steam Generation Units and Heat Exchangers*, 1965. Obtained from secondary references: [58] and [69].
- [19] P. Saha and N. Zuber. Point of Net Vapor Generation and vapor void fraction in subcooled boiling. In *Proceedings of the 5-th International Heat Transfer Conference*, volume 4, pages 175–179, Tokyo, Japan, 1974.
- [20] L. Sabotinov. *Experimental investigation of the void fraction at subcooled boiling for different heat flux profiles along the channel*. PhD thesis, Moscow Power Engineering Institute, Moscow, Russia, 1974.
- [21] D. C. Groeneveld et al. 1986 AECL-UO critical heat flux lookup table. *Heat Transfer Engineering*, 7:46–62, 1986.
- [22] W. R. Gambill and R.D. Bundy. Heat-transfer studies of water flow in thin rectangular channels. Part I - Heat Transfer, Burnout and Friction for water in turbulent forced convection. *Nuclear Science and Engineering*, 18:69–79, 1964.
- [23] C. Chichoux et al. Experimental study on heat transfer and pressure drop in rectangular narrow channel at low pressure. In *13th International Heat Transfer Conference (IHTC13)*, Sidney, Australia, 2006.
- [24] T. Hamidouche et al. Simplified numerical model for defining Ledinegg flow instability margins in MTR research reactor. *Progress in Nuclear Energy*, 51:485–495, 2009.
- [25] Special Metals. Inconel alloy 600: physical properties. www.specialmetals.com (accessed 15 Jan. 2015).
- [26] J. M. Corsan and N. J. Budd. An intercomparison involving PTB and NPL of thermal conductivity measurements on stainless steel, Inconel and Nimonic alloy reference materials, and an iron alloy. In *12th European Conference on Thermophysical Properties*, Vienna, Austria, Sept. 24-28 1990.
- [27] J. Clark and R. Tye. Thermophysical properties reference data for some key engineering alloys. *High Temperatures-High Pressures*, 35:1–14, 2003.

- [28] J. Blumm et al. Measurement of the thermophysical properties of a NPL thermal conductivity standard Inconel 600. *High Temperatures-High Pressures*, 36:621–626, 2007.
- [29] L. Filoni and G. Rocchini. Thermal conductivity of Inconel 600 and Ti - 6Al - 4V from 360 K to 900 K. *High Temperatures-High Pressures*, 21:373–376, 1989.
- [30] Hot Disk. Thermal conductivity measurements on an NPL certified Inconel 600 sample and brass sample at high temperatures with the Hot Disk Thermal Constants Analyser, 2005. www.hotdiskinstruments.com (accessed 15 Jan. 2015).
- [31] J.A. Boure A.E. Bergles and L.S. Tong. Review of two-phase flow instability. *Nuclear Engineering and Design*, 25:165–192, 1973.
- [32] R. K. Shah and A. L. London. *Laminar Flow Forced Convection in Ducts*. Academic Press, New York, 1978. in Supplement 1 to *Advances in Heat Transfer*. Obtained from secondary references: [16] and [15].
- [33] O. Mokrani et al. Fluid flow and convective heat transfer in flat microchannels. *International Journal of Heat and Mass Transfer*, 52:1337–1352, 2009.
- [34] C. Wang et al. Experimental study of friction and heat transfer characteristics in narrow rectangular channel. *Nuclear Engineering and Design*, 250:646–655, 2012.
- [35] J. Ma et al. Experimental studies on single-phase flow and heat transfer in a narrow rectangular channel. *Nuclear Engineering and Design*, 241:2865–2873, 2011.
- [36] D. Xing et al. A theoretical analysis about the effect of aspect ratio on single-phase laminar flow in rectangular ducts. *Progress in Nuclear Energy*, 65:1–7, 2013.
- [37] Z. H. Liang et al. Experimental investigation on flow and heat transfer characteristics of single-phase flow with simulated neutronic feedback in narrow rectangular channel. *Nuclear Engineering and Design*, 248:82–92, 2012.
- [38] Y. Sudo et al. Experimental study of differences in single-phase forced-convection heat transfer characteristics between upflow and downflow for narrow rectangular channel. *Journal of Nuclear Science and Technology*, 22:202–212, 1985.
- [39] C. Wang et al. Forced convection heat transfer and flow characteristics in laminar to turbulent transition region in rectangular channel. *Experimental Thermal and Fluid Science*, 44:490–497, 2013.
- [40] C. Wang et al. Experimental study of transition from laminar to turbulent flow in vertical narrow channel. *Annals of Nuclear Energy*, 47:85–90, 2012.
- [41] N. Silin et al. Hydrodynamic transition delay in rectangular ducts under high heat flux. *Annals of Nuclear Energy*, 37:615–620, 2010.
- [42] H. Blasius. Das Ähnlichkeitsgesetz bei reibungsvorgängen in flüssigkeiten. *Forsch. Arb. Ing.-Wes.*, 131, 1913. Obtained from secondary reference [16].

- [43] M. Siman-Tov et al. Thermal-hydraulic correlations for the advanced neutron source reactor fuel element design and analysis. In *Proceedings of the ASME Heat Transfer Division, Vol. 190*. ASME, 1991.
- [44] E. Royer et al. FLICA4: Status of numerical and physical models and overview of applications. In *Proceedings of NURETH-11*, Avignon, France, 2005.
- [45] S. M. Marco and L. S. Han. A note on limiting laminar Nusselt number in ducts with constant temperature gradient by analogy to thin-plate theory. *Transactions of the ASME*, 77:625–630, 1955. Obtained from secondary reference [16].
- [46] C. L. Hwang and L. T. Fan. Finite difference analysis of forced-convection heat transfer in entrance region of a flat rectangular duct. *Appl. Sci. Res.*, pages 401–422, 1964.
- [47] R. Siegel and E.M. Sparrow. Simultaneous development of velocity and temperature distributions in a flat duct with uniform wall heating. *A.I.Ch.E. Journal*, 5:73–75, 1959.
- [48] A. K. Muntjewerf. *Laminar flow heat transfer in the thermal entrance region of flat and profiled ducts*. PhD thesis, Delft university of technology, Netherlands, 1969.
- [49] A. Ghione B. Noel, P. Vinai and C. Demazière. On the prediction of single-phase forced convection heat transfer in narrow rectangular channels. In *Proceedings of the 10th International Topical Meeting on Nuclear Thermal Hydraulics, Operation and Safety (NUTHOS-10)*, Okinawa, Japan, 2014. NUTHOS10-1116.
- [50] S. Levy R. A. Fuller and R. O. Niemi. Heat transfer to water in thin rectangular channels. *Journal of Heat Transfer - Transactions of the ASME*, pages 129–143, 1959.
- [51] T. M. Adams et al. An experimental investigation of single-phase forced convection in microchannels. *International Journal of Heat and Mass Transfer*, 41:851–857, 1998.
- [52] W. H. McAdams. *Heat Transmission*. Mcgraw-Hill, New York, 2nd edition, 1942.
- [53] E. N. Sieder and G. E. Tate. Heat transfer and pressure drop of liquids in tubes. In *Heat Transfer Symposium*, pages 1429–1435, Division of Industrial and Engineering Chemistry, Yale University, USA, 1936.
- [54] V. Gnielinski. New equations for heat and mass transfer in turbulent pipe and channel flow. *International Chemistry Engineering*, 16:359–368, 1976.
- [55] B. S. Petukhov. Heat transfer and friction in turbulent pipe flow with variable physical properties. *Advances in heat transfer*, 6:503–564, 1970.
- [56] M. Siman-Tov et al. FY 1995 Progress report on the ANS Thermal-Hydraulic Test Loop operation and results. Technical report, ORNL/TM-12972, Oak Ridge National Laboratory, Tennessee, USA, 1997.

- [57] R. Ricque and R. Siboul. Etude experimentale de l'échange thermique a flux eleve avec l'eau en convection forcee a grande vitesse dans des tubes de petit diametre, avec et sans ebullition. *International Journal of Heat and Mass Transfer*, 15:579–592, 1972.
- [58] J. G. Collier and J. R. Thome. *Convective boiling and condensation*. Clarendon Press - Oxford, 1994.
- [59] S. G. Kandlikar. Heat transfer characteristics in partial boiling, fully developed boiling and significant void flow regions of subcooled flow boiling. *Journal of heat transfer*, 120:395–401, 1998.
- [60] R. H. Whittle and R. Forgan. A correlation for the minima in the pressure drop versus flow-rate curves for sub-cooled water flowing in narrow heated channels. *Nuclear Engineering and Design*, 6:89–99, 1967.
- [61] A. E. Bergles and W. M. Rohsenow. The determination of forced-convection surface-boiling heat transfer. *Journal of Heat Transfer*, 86:365–372, 1964.
- [62] Y. Sudo et al. Experimental study of incipient nucleate boiling in narrow vertical rectangular channel simulating subchannel of upgraded JRR-3. *Journal of Nuclear Science and Technology*, 23:73–82, 1986.
- [63] G. R. Warriar and V. K. Dhir. Heat transfer and wall heat flux partitioning during subcooled flow nucleate boiling - A review. *ASME Journal of Heat Transfer*, 128:1243–1256, 2006.
- [64] K. Forster. Heat transfer to a boiling liquid; mechanism and correlations. Technical report, University of California, 1958.
- [65] S. G. Kandlikar. A general correlation for saturated two-phase flow boiling heat transfer inside horizontal and vertical tubes. *Journal of heat transfer*, 112:219–228, 1990.
- [66] J. C. Chen. Correlation for boiling heat transfer to saturated fluids in convective flow. *Industrial and Engineering Chemistry Process Design and Development*, 5:322–329, 1966.
- [67] W. H. Jens and P. A. Lottes. Analysis of heat transfer, burnout, pressure drop and density data for high-pressure water. Technical report, 1951. Argonne national laboratory, ANL-4627.
- [68] S. Qiu et al. Experimental study on heat transfer of single-phase flow and boiling two-phase flow in vertical narrow annuli. In *Proceedings of ICONE10*. ASME, 2002. ICONE10-22212.
- [69] M. Belhadj et al. Determining wall superheat under fully developed nucleate boiling in plate-type research reactor cores with low-velocity upwards flows. *Nuclear Technology*, 95:95–102, 1991.
- [70] D. Gorenflo. *Pool Boiling*. Springer, 2010. Chapter taken from: VDI Heat Transfer Atlas.

- [71] D. Bestion P. Griffith, M. Thurgood and G. Yadigaroglu. TRACE Version 5.0 computer code independent peer review. Technical report, 2009.
- [72] A. P. Olson and M. Kalimullah. A user's guide to the PLTEMP/ANL code (version 4.1). Technical report, 2011. Argonne national laboratory, ANL/RERTR/TM-11-22.
- [73] S. Fabrega. Le calcul thermique des reacteurs de recherche refroidis par eau. Technical report, 1971. Rapport CEA-R-4114.
- [74] K. Engelberg-Forster and R. Greif. Heat transfer to a boiling liquid; mechanism and correlations. *ASME Journal of Heat Transfer*, 81:43–53, 1959.
- [75] A. E. Bergles and W. M. Roshenow. Forced-convection surface-boiling heat transfer and burnout in tubes of small diameter. Technical report, 1962. MIT-Report 8767-21.
- [76] S. Fabrega. *Etude experimentale des instabilites hydrodynamiques survenant dans le reacteurs nucleaires a ebullition*. PhD thesis, University of Grenoble, CEA-Grenoble, 1966.

Paper I

*On the prediction of single-phase forced convection heat transfer in
narrow rectangular channels*

A. Ghione, B. Noel, P. Vinai, C. Demazière
NUTHOS10-1116, The 10th International Topical Meeting
on Nuclear Thermal Hydraulics, Operation and Safety
(NUTHOS-10), Okinawa (Japan), Dec. 14-18 2014

Paper II

*Wall superheat prediction in narrow rectangular channels under Fully
Developed Boiling of water at low pressures*

A. Ghione, B. Noel, P. Vinai, C. Demazière

Manuscript to be submitted to the 16th International Topical
Meeting on Nuclear Reactor Thermal Hydraulics (NURETH-16),
Chicago (USA), Aug. 30 - Sep. 4 2015.